Chair of Astronautics
School of Engineering and Design
Technical University of Munich

Solar-vapor pyrolysis of lunar regolith for oxygen production in high vacuum

An experimental investigation and thermochemical modeling

RT-MA 2022/01

Rok Šeško

Thesis for the attainment of the academic degree

Master of Science (M.Sc.)

at the School of Engineering and Design of the Technical University of Munich.

Examiner:

Prof. Prof.h.c. Dr. Dr.h.c. Ulrich Walter[1]

Supervisors:

Laura Grill, M.Sc.[1]
Dr. Aidan Cowley[2]

Submitted:

Munich, September 7th, 2022

[1]Chair of Astronautics, Technical University of Munich
[2]European Astronaut Center, European Space Agency

Mir als vertraulich genannte Informationen, Unterlagen und Erkenntnisse werde ich nach meiner Tätigkeit am Lehrstuhl nicht an Dritte weitergeben.

Ich erkläre mich außerdem damit einverstanden, dass meine Bachelor-, Semester-, Master-/Diplomarbeit vom Lehrstuhl auf Anfrage fachlich interessierten Personen, auch über eine Bibliothek, zugänglich gemacht wird, und dass darin enthaltene Ergebnisse sowie dabei entstandene Entwicklungen und Programme vom Lehrstuhl für Raumfahrttechnik uneingeschränkt genutzt werden dürfen. (Rechte an evtl. entstehenden Programmen und Erfindungen müssen im Vorfeld geklärt werden.)

Ich erkläre außerdem, dass ich diese Arbeit ohne fremde Hilfe angefertigt und nur die in dem Literaturverzeichnis angeführten Quellen und Hilfsmittel benutzt habe.

Munich, September 7th, 2022 Rok Šeško

Abstract

Oxygen is one of the essential consumables in space exploration, being used as an oxidizer in chemical propulsion and for human life support systems. With the planned future long-term human missions to the moon, the need for oxygen delivery to the lunar surface will only increase. The idea of producing oxygen and other consumables from lunar materials has been present in research for some time. Multiple processes have been developed and tested here on Earth. Most processes utilizing oxygen bound in the lunar regolith also require consumables themselves. This thesis investigates the process of solar-vapor pyrolysis, which can use unbeneficiated regolith, sunlight, and vacuum to produce oxygen and other byproducts without requiring any consumables.

Thermal reduction of metal oxides in lunar regolith is heavily dependent on pressure conditions during the pyrolysis process. Lower pressures decrease the temperature at which oxides present in lunar regolith are dissociated into oxygen, suboxides, and metals. This makes pressure an essential parameter for future design and optimization of reactors for lunar operations. The pyrolysis reactions are studied at lower pressures in the high vacuum regime to determine the ideal conditions for oxygen production. This is done experimentally on a small purpose-built solar-vacuum furnace where partial vaporization of regolith simulant EAC-1A is demonstrated, although no quantitative conclusions on oxygen production can be drawn.

Ideal conditions for pyrolysis in the pressure range of 10^{-8} mbar to 10^{3} mbar and temperatures range of 289 K to 3773 K are determined through thermochemical equilibrium modeling. The influence of regolith composition on oxygen production is studied through modeling of three representative regolith compositions and the EAC-1A simulant. It is shown that the ideal molecular oxygen yields range from 6.6% to 14.1%, with EAC-1A exhibiting the highest yields, followed by low-Ti Maria, high-Ti Maria, and Highlands regolith.

Additionally, a model is presented which combines the oxygen yield from the thermochemical model with a solar-thermal simulation of the regolith surface to evaluate oxygen production during solar heating of regolith. The model shows that the experiments were performed nearly at the lowest solar power boundary, where pyrolysis still occurs. An increase in solar power applied to the regolith surface would significantly increase oxygen production. A doubling of the experimental solar power would lead to an up to ten-fold increase in theoretical O_2 mass production. Further increases in solar power would lead to progressively lower increases in oxygen production.

Zusammenfassung

Sauerstoff ist einer der wichtigsten Elementen in der Raumfahrt, da er als Treibstoff für chemische Antriebe und für Lebenserhaltungssysteme für Astronauten verwendet wird. Mit den geplanten bemannten Langzeitmissionen zum Mond wird der Bedarf an Sauerstoff auf der Mondoberfläche weiter steigen. Die Idee, Sauerstoff und andere Verbrauchsmaterialien aus lokalen Rohstoffen auf dem Mond zu gewinnen, wird in der Forschung schon seit einiger Zeit verfolgt. Hier auf der Erde wurden bereits mehrere Verfahren entwickelt und getestet, vobei die meisten den im Mondregolith gebundenen Sauerstoff nutzen und weitere Verbrauchsstoffe benötigen.

In dieser Arbeit wird der Prozess der solaren Dampfphasenpyrolyse untersucht, bei dem aus nicht aufbearbeitetem Regolithh, Sonnenlicht und Vakuum Sauerstoff und andere Nebenprodukte erzeugt werden können, ohne dass weitere Materialien erforderlich sind. Die thermische Reduktion von Metalloxiden im Mondregolith ist stark von den Druckverhältnissen während des Prozesses abhängig. Bei niedrigerem Druck sinkt die Temperatur, bei der die im Mondregolith vorhandenen Oxide in Sauerstoff, Suboxide und Metalle aufgespalten werden. Dies macht den Druck zu einem wichtigen Parameter für die künftige Konstruktion von Reaktoren für den Einsatz auf dem Mond. Um die idealen Bedingungen für die Sauerstoffproduktion zu ermitteln, wurde die Pyrolysereaktion bei niedrigeren Drücken im Hochvakuumbereich untersucht. Dies geschah experimentell in einem kleinen, eigens für diesen Zweck gebauten Solar-Vakuum-Ofen, in dem die unvollständige Verdampfung des Regolith-Simulats EAC-1A nachgewiesen wurde, ohne dass quantitative Schlussfolgerungen zur Sauerstoffproduktion gezogen werden können.

Ideale Bedingungen für die Pyrolyse im Druckbereich von 10^{-8} mbar zu 10^{3} mbar und im Temperaturbereich von 289 K zu 3773 K sind durch thermochemische Gleichgewichtsmodellierung bestimmt. Der Einfluss der Regolithzusammensetzung auf die Sauerstoffproduktion ist durch die Modellierung von drei repräsentativen Zusammensetzungen und des EAC-1A-Simulats untersucht. Die idealen Sauerstoffausbeuten liegen zwischen 6,6% und 14,1% liegen, wobei EAC-1A die höchsten Ausbeuten aufweist, gefolgt von Mare-Regolith mit niedrigem Ti-Gehalt, Mare mit hohem Ti-Gehalt und Highland-Regolith.

Um die Sauerstoffproduktion während der solaren Erwärmung des Regoliths zu evaluieren, wird ein Modell vorgestellt, in welchem die Sauerstoffausbeute aus der thermochemischen Simulation mit einem solarthermischen Modell der Regolithoberfläche kombiniert wird. Dieses ist gezeigt, dass die Experimente nah an der unteren Grenze der solaren Leistung durchgeführt wurden, wo Pyrolyse noch möglich ist. Eine Erhöhung der solaren Leistung würde wesentlich zum Sauerstoffgewinn beitragen. Eine Verdoppelung der experimentellen Solarleistung würde bis zu einer Verzehnfachung der theoretischen O_2 Masse führen. Ein weiterer Anstieg der Solarleistung würde zu einer immer geringeren Steigerung der Sauerstoffproduktion führen.

Acknowledgments

First of all, I would like to thank Dr. Aidan Cowley for trusting me with this project, for his refreshing ideas, and for maintaining an assortment of wonderful interns and trainees at Spaceship EAC, making it a great place to work. I especially have to thank a few interns and trainees who helped me and the project along the way. Thank you to Kim Lamboley for being a great collaborator and successor on the ROAST project. Also, thanks to Alexandra Adiaconitei for all the help and administrative support, Leonardo for a great introduction to ROAST and the lab, and Nils for fruitful discussions about mechanical design and building things.

I want to thank Laura Grill for being a great mentor and for being patient with my sometimes chaotic and overambitious ideas during the writing of this thesis. I also have to thank the Chair of Astronautics at the Technical University of Munich and Prof. Dr. Walter for the incredible lectures on space exploration and the possibility of working on thesis projects in this field.

A large part of this thesis would also not exist without Thorben de Riese and the Chair of Energy Systems at the Technical University of Munich, who provided access to the FactSage simulation package for the equilibrium calculations. I also have to thank Marco for the help with the melt sample analysis.

Last but not least, a big thank you to my family for all their support, even if mostly through a screen.

Contents

List of Figures

List of Tables

Symbols and constants

Symbol	Description	Value	Unit
a	component activity	-	-
C	solar concentration ratio	-	-
C_p	specific heat capacity	-	$\mathrm{J\,kg^{-1}\,K^{-1}}$
E	solar flux density	-	$\mathrm{W\,m^{-2}}$
G	Gibbs free energy	-	J
h	specific enthalpy	-	$\mathrm{J\,kg^{-1}}$
H	enthalpy	-	J
K	equilibrium constant	-	-
Kn	Knudsen number	-	-
m	mass	-	g
M	molar mass	-	$\mathrm{g\,mol^{-1}}$
p	pressure	-	Pa
p_{ini}	initial pressure	-	Pa
p_{O2}	partial pressure of molecular oxygen	-	Pa
p_O	partial pressure of atomic oxygen	-	Pa
p_r	reactor pressure	-	Pa
R	universal gas constant	8.3145	$\mathrm{J\,K^{-1}\,mol^{-1}}$
r, θ, z	cylindrical coordinates	-	m,°,m
S	entropy	-	$\mathrm{J\,K^{-1}}$
T	temperature	-	K
t	time	-	s
U	internal energy	-	J
V	volume	-	$\mathrm{m^3}$
x,y,z	spatial coordinates	-	m
L	latent heat	-	$\mathrm{J\,kg^{-1}}$
α	absorbance	-	-
α_s	solar elevation angle	-	°
Δ	difference operator	-	-
η	efficiency/yield	-	-
λ	optical wavelength	-	-
Φ	energy flux	-	W
ρ	reflectance	-	-
σ	standard deviation	-	-
σ	Stefan-Boltzmann constant	$5.670\,373 \times 10^{-8}$	$\mathrm{W\,m^{-2}\,K^{-4}}$
τ	transmittance	-	-
θ	phase indicator	-	-

Acronyms

Acronym	Description
AM	Air Mass
BDF	Backwards Differentiation Formula
DLR	Deutsches Zentrum für Luft und Raumfahrt (German Aerospace Center)
DNI	Direct Normal Irradiance
EAC	European Astronaut Center
EDX	Energy Dispersive X-ray Spectrometry
ESA	European Space Agency
ExPeRT	Exploration Preparation, Research and Technology Team
GEO	Geostationary Earth orbit
HV	High Vacuum
IR	Infra-Red
ISRU	In-Situ Resource Utilization
JSC	Johnson Space Center
LEO	Low-Earth Orbit
MLS	Minnesota Lunar Simulant
NASA	National Air and Space Administration
NRMSE	Normalized Root-Mean-Square Error
RGA	Residual Gas Analyzer
RMS	Root Mean Square
SEM	Scanning Electron Microscope
TRL	Technology Readiness Level
TUM	Technical University of Munich
UHV	Ultra High Vacuum

1 Introduction

Methods for sustainable lunar exploration are increasingly becoming an important topic as NASA, ESA, and other space agencies are preparing for a return of humans to the lunar surface with the Artemis missions [1]. This return to the Moon is an essential step in space exploration as described in the Global Exploration Roadmap [2]. It outlines the vision for lunar exploration as a step toward eventual Mars missions and long-term lunar activities. To make human presence on the Moon sustainable, it is vital to develop technologies and methods that reduce mission costs and enable larger and longer space exploration endeavors.

The main obstacle to large-scale space exploration is the Earth's gravity well which inflicts a high cost on the transportation of any material from the Earth's surface into orbit and beyond. NASA estimates the cost of launch to the lunar surface at US$90,000/kg [3], which is expected to become cheaper with increased frequency of launches and following the trend of decreasing launch costs to LEO in recent years. These have fallen from US$54,500/kg for launches by NASA's space shuttle to US$2,720/kg for launches with SpaceX's Falcon 9 [4, 5]. A study by Kornuta et al. [6] states the potential future transportation cost from Earth to the lunar surface at US$35,000/kg. Despite a potential significant cost reduction, launch cost will still remain a major fraction of total mission cost.

Moreover, the payload mass of a rocket is fundamentally restricted by the amount of propellant needed for a launch from the Earth's surface, even if the cost of the launcher and its fuel fall significantly. Any propellant or consumables stored as a payload at launch, meant for lunar operations or an Earth return, heavily restrict the mass of other hardware on a single launcher. Production of propellants in the comparatively low gravity environment of the Moon could be one of the solutions for fueling lunar surface activities and potentially refueling spacecraft bound for destinations beyond the Moon, as well as satellites in cis-lunar space [3]. Earth orbits, including geostationary (GEO) and low Earth orbit (LEO), require less energy to be accessed from the lunar surface than from Earth [7]. Although, an analysis by Jones [8] states that the financial breakeven point between Earth-launched propellant and lunar in-situ produced propellant for cis-lunar space will only be reached in 35 years. Therefore, the short to middle-term interest still lies with the use of in-situ produced consumables on the lunar surface.

1.1 Lunar in-situ oxygen production

The lunar surface offers a potential for the extraction of various materials. These include solar implanted volatiles, water ice, oxygen, silicon, iron, aluminum, titanium, and other metals from the lunar soil or regolith. Oxygen is one of the most important resources available since it is needed for human life support systems and as a spacecraft propellant. It can be made from local water ice or volatile water by way of electrolysis. It can also be made from the oxide-rich lunar regolith. Lunar surface regolith is particularly interesting for oxygen production due to its significant percentage of oxides by weight, such as plagioclase, pyroxene, olivine, and ilmenite. It contains approximately 45 wt% of oxygen, although this value changes slightly with the differences in the regional regolith composition across the lunar surface. [9, 7]

Oxygen bound in the regolith can be extracted using different processes, for example, by using reactive gasses, which reduce the metal oxides and substitute the oxygen, or by electrolysis of the regolith itself.

Another approach, vapor-phase pyrolysis, uses thermal energy to reduce the regolith, extracting the oxygen from the metal oxides without a reactive gas. Pyrolysis is particularly interesting because it does not require additional consumable resources such as reactive gasses and works with all and unbeneficiated regolith compositions. [9, 10]

A pyrolysis process on the lunar surface would require only regolith and a heat source, which can be electric-resistive or inductive in case of abundant power in the future. Regolith can also be heated directly with concentrated sunlight, which requires less infrastructure than high-power electricity generation [11, 12]. Focused sunlight can potentially heat regolith to temperatures on the order of 2000 K to 3000 K [13]. These temperatures are sufficient for full or partial dissociation of oxides in rough vacuum. A decrease in pressure into high or ultra-high vacuum regimes results in a decrease in expected dissociation temperature, which can be beneficial from an energy consumption perspective and in terms of thermal loads on a pyrolysis reactor [14].

Dissociation temperatures in the order of 1100 K have been modeled by Shaw et al. [15] at pressures of 10^{-12} mbar. These conditions lie in the sublimation regime, where evaporation and dissociation take place from solid state regolith, instead of a molten state at higher pressures. Pressures applicable for pyrolysis reactors are likely to be higher, which would be beneficial from the reaction kinetics and oxygen throughput perspective [15]. Dissociation conditions throughout a higher pressure range of 10^{-8} mbar to 10^{3} mbar are studied and presented in this thesis.

1.2 Spaceship EAC

This solar-vapor pyrolysis process is being investigated as project ROAST (Regolith Only and SunlighT) at the Spaceship EAC - an initiative of the ESA's Exploration Preparation, Research and Technology Team (ExPeRT) located at the European Astronaut Center in Cologne, Germany. Spaceship EAC is investigating innovative low TRL technologies in fields of Energy, Advanced Manufacturing, Disruptive Technologies, Physiological and Exercise Countermeasures, and Space Resources as preparation for the future of space exploration. [16]

A small prototype solar vacuum furnace for pyrolysis experiments was designed and built during an internship at Spaceship EAC. This thesis presents the first experiments with this furnace setup, their results, and the modeling of the pyrolysis process.

1.3 Thesis objectives and outline

This thesis focuses on oxygen extraction from regolith and regolith simulants by way of solar-vapor pyrolysis through experiments and computational modeling. The potential metallic and suboxide byproducts of the process are not studied in this thesis. The objectives of this thesis are to:

1. demonstrate the achievement of temperature and pressure conditions in the solar furnace, theoretically required for regolith pyrolysis to occur,
2. and determine the ideal reaction temperature and pressure conditions for oxygen production in a small solar-vapor pyrolysis reactor.

The first part of this thesis presents the underlying fundamentals, state-of-the-art in-situ oxygen extraction processes, and the applicability of concentrated solar power for ISRU. Next, the prototype solar-vapor pyrolysis setup, experiments, and results are presented and discussed to fulfill the first thesis objective. Afterward, two chapters on computational modeling are presented to fulfill the second objective. The first

focuses on the thermochemical equilibrium modeling of the pyrolysis process to provide an insight into the behavior of regolith in a vacuum at high temperatures. This chapter presents characteristic oxygen yields for each modelled pressure between 10^{-8} mbar and 10^{3} mbar as its result. The second modeling chapter focuses on the thermal modeling of the regolith under concentrated solar irradiation to study the interaction between concentrated solar power, regolith properties, and regolith pyrolysis. The latter also evaluates the solar-heated regolith surface for potential oxygen production by using the oxygen yield values from the equilibrium model. At the end, the experimental and modeling aspects of this thesis are discussed, and an outlook for further theoretical and experimental work is given.

2 Fundamentals

The lunar environment is hostile to human exploration with its vacuum, radiation, meteoroid impacts, temperature fluctuations, harsh sunlight, and a monotonous regolith surface [17]. This thesis investigates the use of three of these characteristics of the lunar environment for the production of oxygen: vacuum, sunlight, and lunar regolith.

Lunar regolith is a scarce resource for experiments on Earth as only Apollo, Luna, and Chang'e missions have brought back samples for study. The experiments in this thesis have been done with a lunar regolith simulant, an analog material mimicking the properties of lunar regolith. Several simulants have been developed and used since the 1970s. Each one is mostly specialized to mimic a limited number of properties. For example, some mimic the mineralogical composition, and others their geotechnical properties. Simulants are, therefore, not an ideal representation of lunar soil and should be compared to lunar regolith to be aware of differences in properties between them. [5, 7]

2.1 Lunar regolith

The Moon is divided into two major geological regions, the darker maria and the lighter highlands. Mare regolith stems from basaltic lava flows in large basins created through meteorite bombardment, while the original lunar crust can be found in the highlands. Mare rocks are predominantly basaltic in compositions and contain mostly pyroxene, olivine, ilmenite, and some plagioclase, while the highlands contain more plagioclase and less olivine, pyroxene, and ilmenite. This makes the highlands rich in calcium and aluminum oxides, while mare is richer in iron oxides. [17, 18]

Mare regolith is sometimes further classified into two groups based on its titanium content, high-titanium Mare (>6 wt% TiO_2) and low-titanium mare (<6 wt% TiO_2), secondary and tertiary classifications can also be made with the Al_2O_3 and K content [19]. Papike [20] identified two samples, Apollo 16 sample 64501 and Luna 24 sample 24999, as "clean" representations of Highlands and Maria regolith, respectively. The composition of these two samples available in [21, 22] will be used for modeling pyrolysis behavior in this thesis.

2.1.1 Lunar regolith simulants

Testing of ISRU processes and other lunar-related activities require significant amounts of regolith to ensure the relevance and validity of experiments for eventual high-throughput operational lunar reactors. Regolith is altered significantly during most ISRU processes, especially during oxygen or metal extraction, where the oxides are dissociated. This research cannot be done with real lunar soil on a large scale. Regolith simulants have therefore become an essential part of ISRU research. [5]

The main problem with using regolith simulants for ISRU studies is the sometimes significant differences in their fundamental properties. None of the currently available simulants can be considered a perfect copy of real lunar soil. They are mostly made for a specific purpose with only a few properties being engineered to fit those of lunar soil. Other properties might be very different from those of real lunar regolith. Therefore, it is important to understand the properties of the simulant and its differences from the real lunar soil. [23]

The simulant used in this thesis is EAC-1A because of its availability at the European Astronaut Center, where it was developed. Its geophysical properties, grain size distribution, sphericity, and cohesion are similar to Apollo 17 soils. On the other hand, the important mineralogical properties for this thesis, exhibit notable deviations from lunar soil. Major components of the simulant are shared with Apollo soils, but EAC-1A includes higher contents of alkali minerals and thus higher K_2O and Na_2O content. The composition also differs due to chlorite, quartz, and feldspathoids, which are rare in lunar soil. EAC-1A also includes small amounts of hydrogen and carbon, 0.18% and 0.19%, respectively, which are not taken into account in this thesis's modeling due to their small mass fractions. [5, 24]

Another major difference between EAC-1A and lunar soil is the presence of iron(III) oxide Fe_2O_3 instead of the iron(II) oxide O present in lunar soil compositions [25]. This difference has a significant impact on the equilibrium calculations in section 4 with regolith compositions listed in Tab. 4.1.

2.1.2 Heat transfer in regolith

Heat transfer in particulate matter is one of the most important phenomena to be considered in thermal modeling in section 5.2. The first major heat transfer property is its specific heat capacity, which governs the energy required to heat the regolith to a specific temperature. The heat capacity of Apollo soils has only been measured up to 350 K [26]. Values above this temperature have to be extrapolated or substituted by measurements of analogous terrestrial materials, for example, silicate glasses and liquids. Measurements of these materials [27] can be integrated into approximate models describing a wider temperature range as described in Schreiner et al. [28] The thermal conductivity k of regolith is the other important heat transfer property of regolith. The conductivity of particulate material such as regolith cannot simply be modeled as a normal continuous material due to the gaps in solid material, gaseous material in these gaps, and small contact surfaces between the particles. Therefore, a conductivity model such defined by [29] in Eq. 2.1 is applicable. It incorporates a temperature-dependent radiation term $k_{rad}\,T^3$, which accounts for radiative heat transfer from particle to particle, and the temperature-independent solid conductive term k_{cond}, which defines the conductivity through the solid particle.

$$k = k_{cond} + k_{rad}\,T^3 \tag{2.1}$$

This model is defined well in a high vacuum since there is little gaseous material that can contribute to heat transfer between the particles. Gas in a lower vacuum can add significantly to the heat transfer. A semi-empirical model by Parzinger [30] adds two more terms to the conductivity equation: an additional gas term k_{gas} dependent on the number of molecules moving between particle surfaces and a solid/gas coupling term describing the contact between gas and solid particles. The influence of these terms was studied by Reiss [31, 32] to understand which terms govern thermal conductivity at what pressures. Ratios of these conductivity terms are shown in Fig. 2.1. It shows that below 10 Pa (10^{-1} mbar) thermal conductivity is governed primarily by solid contact and radiation, which are not pressure-dependent. Therefore, it is assumed for the purpose of this thesis that thermal conductivity is only temperature dependent. A comprehensive model by Schreiner et al. [28], which is fitted to empirical measurements of lunar soil, regolith simulants, and liquid silicates will be used in this thesis.

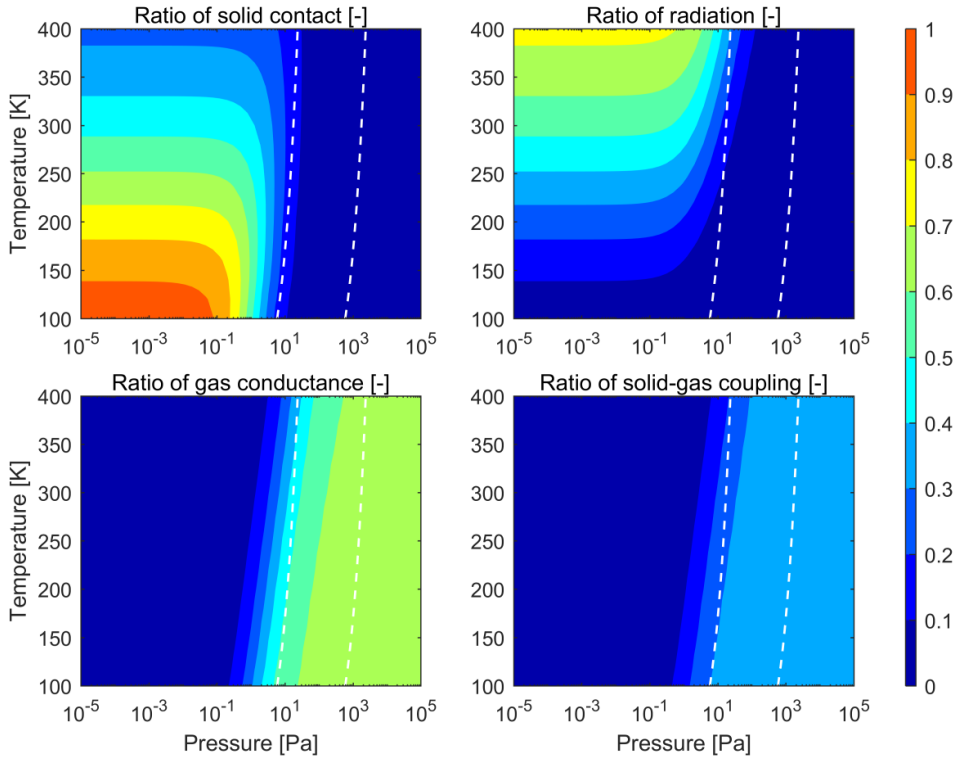

Figure 2.1 Ratio of solid contact, radiation, gas, and solid-gas coupling for the effective thermal conductivity according to Reiss [31]. The left dashed line indicates Kn = 10, and the right dashed line indicates Kn = 0.1.

2.2 Oxygen extraction on the Moon

Oxygen extraction processes for lunar applications have been summarized well by Schwandt [10], and Schlüter and Cowley [9]. These methods can broadly be divided into two categories. Firstly, methods that use lunar polar ice or volatile water and the methods which extract mineralogically bound oxygen.

Lunar surface ice is one of the important sources of oxygen being investigated since the detection of lunar surface ice in the polar regions by Moon Mineralogy Mapper [33]. Water amounts in the permanently shadowed regions could be on the order of 10^{12} kg. This water ice can potentially be split into hydrogen and oxygen by way of electrolysis [7, 9].

Another major source of oxygen is the lunar regolith, which is comprised of approximately 45 wt% of oxygen. This makes regolith a great candidate for oxygen extraction and potential byproducts. Extraction from regolith can be achieved in numerous ways, which can be classified into three main categories: Extraction via reactive gas, Extraction via electrolysis, and Pyrolysis. An example of extraction via reactive gas is the Hydrogen reduction process described by Eq. 2.2. This process reduces only the iron oxide fraction of ilmenite ($FeTiO_3$), producing water and iron metal. This means Ilmenite-rich mare soils or beneficiated feedstock has to be used to increase the efficiency of the process, which is comparatively low. Additionally, the produced water then has to be electrolyzed to produce hydrogen and oxygen for further consumption.

$$FeTiO_3 + H_2 \longrightarrow H_2O + Fe + TiO_2 \tag{2.2}$$

An example of extraction via electrolysis is molten salt electrolysis, which is already used in industrial applications on Earth for the production of metals. A variant of this process, FFC molten salt electrolysis,

functions by submerging a sintered metal oxide cathode and an anode in a molten salt bath. Oxygen is ionized on the cathode and moves towards the anode, where the oxygen anions are oxidized. The resulting gas can be collected and filtered for storage. The last category is represented by vapor phase pyrolysis. By heating regolith feedstock to high temperatures in a vacuum environment, the metal oxides vaporize/sublimate and dissociate into oxygen, suboxides, and metals.

One of the main factors that will decide which processes will be utilized in the future is the oxygen yield defined in Eq. 2.3 [34], which characterizes the efficiency of the process. The expected oxygen yield ranges for the common processes are shown in Tab. 2.1, summarized from Schlüter and Cowley [9].

$$\eta_{O_2} = \frac{m_{O_2}}{m_{reg}} \tag{2.3}$$

Table 2.1 Oxygen yield of selected extraction processes [9]

Method	Oxygen yield
H_2 ilmenite reduction	1-5%
CH_4 (carbothermal) reduction	15-28%
Fluorination	41-45%
Molten regolith electrolysis	35%
Molten salt electrolysis	21-40%
Vapor phase pyrolysis	2-24%

2.3 Pyrolysis

Metal oxides that make up lunar regolith can be vaporized and reduced into suboxides, oxygen, and metals with only high temperatures and a vacuum environment using the process of vapor(-phase) pyrolysis, sometimes referred to simply as thermal reduction. A major advantage of this process over others is the lack of reactants, gasses, or other consumables needed for the extraction. The process can work with unbeneficiated regolith, vacuum, and a heat source. The heat source (photovoltaic, concentrated solar, or nuclear-electric) can also be chosen flexibly based on the infrastructure of a lunar base [11]. If the heat source used is concentrated sunlight, this process can run sustainably and entirely off locally available resources [9]. This trade-off on this decision can be made only later when planning the base infrastructure. Therefore, the flexibility of the heat source for a pyrolysis oxygen plant is an advantage [11].

Another significant difference to the previously mentioned processes is the separation of oxygen from regolith in the gas phase compared to the separation from solid or liquid regolith. This poses other challenges with the separation of oxygen gas from other vaporized metals and suboxides, which have to be condensed immediately after vaporization to avoid reoxidation and, therefore, loss of gaseous oxygen, which has to be continuously pumped out of the reaction chamber. Several reactor concepts have already been considered. Two examples of a batch and a continuous process reactor are shown in Fig. 2.2.

These reactor concepts also show the potential benefit of the pyrolysis process in regard to its byproducts. The slag and the condensates contain refractory glasses, ceramics, or metals. Slags with lower content of pure elements can be used as construction material. Elemental byproducts like iron, aluminum, and titanium can be used for metal hardware, and sodium and potassium can be used as liquid coolants or for energy storage [35]. Lunar regolith also contains significant amounts of magnesium which could be used as a metal for structural purposes. It can be used for steel or aluminum alloys or in magnesium alloys which can be alloyed with other materials from ISRU sources [36]. The quantity of certain elements and compounds produced as byproducts can be adjusted by changing process temperatures.

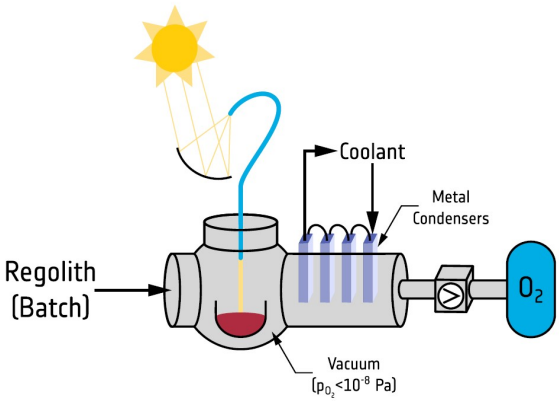

(a) A batch reactor [9]

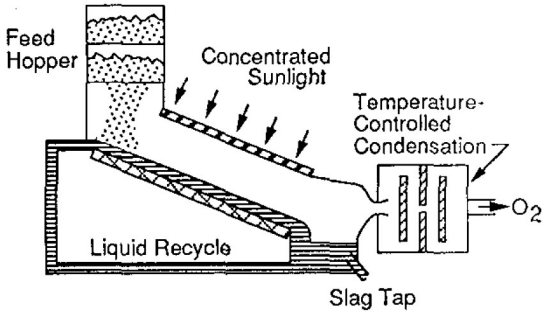

(b) A continuous reactor [11]

Figure 2.2 Illustrations of batch (a) and continuous (b) solar vapor pyrolysis reactors from Schlüter and Cowley [9] and Senior [11]

2.3.1 Thermodynamics of pyrolysis

Molten or solid metal oxides are in thermochemical equilibrium with the dissociated products, shown in Eq. 2.4, where *Me* represents a metal atom and *O* an oxygen atom. With the example of SiO_2, the equation is given in Eq. 2.5. The reaction has to always be kept below equilibrium to reduce the oxides. This requires constant removal of gaseous products from the reactor, so the reaction does not reach equilibrium.

$$Me_xO_y \longleftrightarrow xMe_{(g)} + \frac{y}{2}O_2 \tag{2.4}$$

$$SiO_2 \longleftrightarrow SiO_{(g)} + \frac{1}{2}O_2 \tag{2.5}$$

The dissociation of oxides is governed primarily by the Gibbs free energy equation Eq. 2.6, where G is the Gibbs free energy, H is the enthalpy, T the temperature, and S the entropy. Enthalpy H can be rewritten with an internal energy U, pressure p, and a volume V in Eq. 2.7, showing its dependence on pressure and temperature. This free energy is minimized when a system reaches chemical equilibrium, which a reaction such as pyrolysis is moving towards.

$$G(p, T) = H(p, T) - TS \tag{2.6}$$

$$G(p, T) = U + pV - TS \tag{2.7}$$

The material in a pyrolysis reactor exists in up to 3 phases, whose partial free energies have to be summed to the total Gibbs free energy (Eq. 2.8) [14].

$$G = G_{(s)} + G_{(l)} + G_{(g)} \tag{2.8}$$

The stability of individual components is therefore dependent on the temperature and pressure of the system, described by the equilibrium constant K in Eq. 2.9 with activities a of each of the components. The equilibrium constant can be simplified by assuming the ideal condition of activities being equal to the partial pressures p of components and the activity of solids as 1 in Eq. 2.10 [37].

$$K = \frac{a_{Me_xO_{y(g)}}}{a_{Me_xO_{y(s)}}} = e^{-\frac{\Delta G}{RT}} \tag{2.9}$$

$$K = (p_{Me_{x(g)}})^x \cdot (p_{O_{2(g)}})^{y/2} \tag{2.10}$$

This equilibrium constant is very low, so the vaporization and dissociation do not happen spontaneously for most oxides. Continuous removal of gasses from the chamber can keep pressures low, which results in the reaction not reaching equilibrium and a continuous reduction of the oxides. Continuous removal of gaseous material from the reactor also reduces the temperature at which oxygen is produced due to improved evaporation behavior of oxides. [9] This is beneficial from the energy and engineering perspectives to reduce the thermal requirements of reactor materials.

Matchett [14] calculated that a reduction in pressure from 10^{-4} bar to 10^{-10} bar reduces the temperature of the peak oxygen production by approximately 750 °C. Fig. 2.3 shows this decrease in temperature between higher pressures on the left and lower on the right. The 10^{-7} mbar (10^{-10} bar) pressure is assumed as the chamber pressure for lunar operations. A target pressure of 1.3×10^{-7} mbar (10^{-7} Torr) has also been proposed by Cardiff [38] as this the environmental pressure would be slightly higher in the area surrounding human activity in comparison to the nightly environmental pressure on the lunar surface of approximately 10^{-15} bar [39].

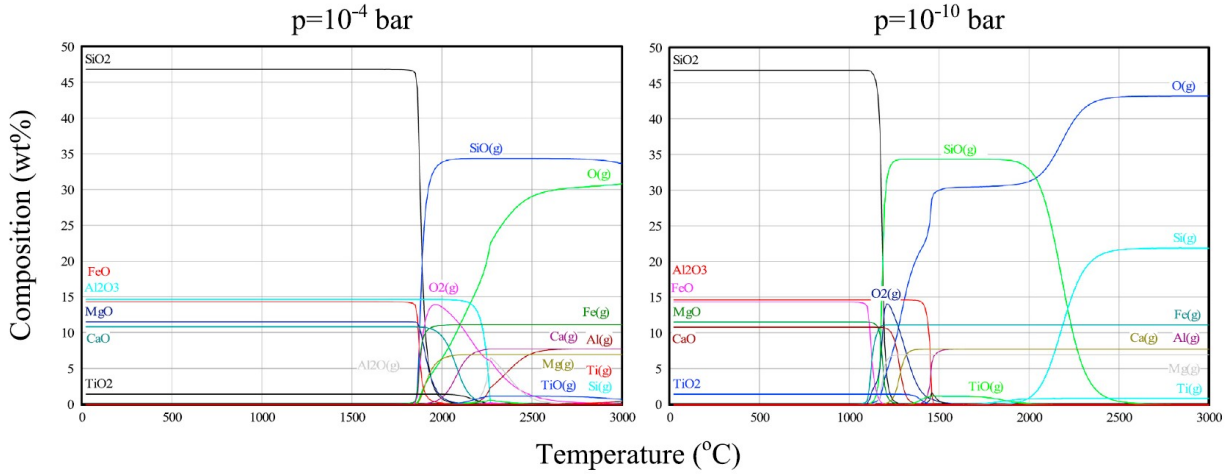

Figure 2.3 Dissociation behavior of Apollo 15 average regolith composition at 10^{-4} bar and 10^{-10} bar

2.3.2 Industrial applications

The technological knowledge needed for vapor phase pyrolysis is already partially present in terrestrial industrial applications. Therefore, this process has the advantage of existing supporting knowledge from the industrial use of vacuum metallurgy. Processes like vacuum deposition for producing thin metal layers, vacuum arc melting, and vacuum distillation for materials like tin, lead, and copper have been practiced to varying degrees for decades [40, 41]. Melting of titanium and aluminum under vacuum is also an important industrial process for the production of stainless steel, titanium, and nickel alloys. Industrial experience in vacuum evaporation, coating, and industrial vacuum pumping systems down to 10^{-6} Torr (1.3×10^{-6} mbar) will be helpful in designing lunar oxygen production plants, and especially the metal condensation and separation systems [11]. Nonetheless, vapor phase pyrolysis provides some additional questions that need to be answered before use in space.

2.3.3 State of the art in vapor-phase pyrolysis

Before the concept of vapor phase pyrolysis was introduced for ISRU applications, Apollo sample vapors have been investigated for other purposes by De Maria [42, 43]. Mass spectrometric investigations of vaporized Apollo samples have been done using a multiple-rotating Knudsen-cell technique and shown vaporization of the oxides and presence of atomic species Na, K, Fe, Mg, Ca, Al, Cr, Mn, O, O_2 molecules and other oxide and suboxide species SiO, SiO_2, FeO, AlO, Al_2O, TiO, and TiO_2 in vapor phase. Fig. 2.4 shows the vapor pressures of these species from the mass spectrometric measurements. This shows the feasibility of producing these species in vapor but not yet for an ISRU application.

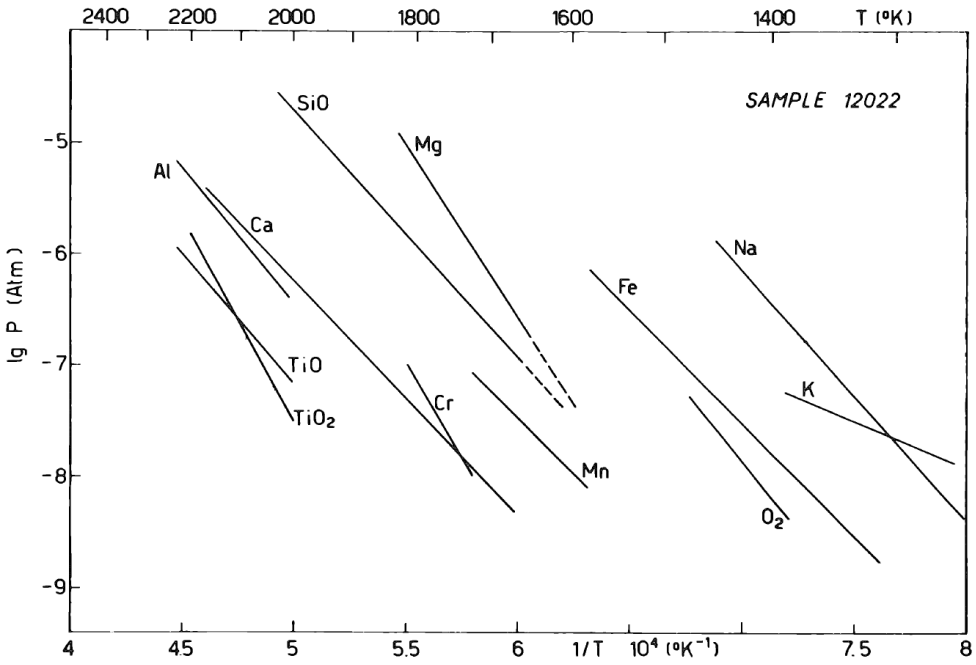

Figure 2.4 Vaporization behavior of Apollo sample 12022 presented by De Maria [42]

The concept of regolith vapor pyrolysis as an ISRU process has been formulated theoretically by Steurer and Nerad [37], who calculated yield ranges for single oxides and defined some basic principles of operation for a pyrolysis reactor. Senior [11] has done some preliminary experimental work and refined the concept with more accurate pressure, temperature, and oxygen yield predictions. Two experimental studies have been done by Sauerborn [44] at the DLR Solar furnace in Cologne, Germany, and Matchett [45, 14] using a Fresnel lens concentrator.

Detailed thermochemical equilibrium modeling has been done by Shaw et al. [15] with a focus on metal production, especially potassium, sodium, and FeO. The first stage of their model gives good insight into the gas species evolution of heated regolith. The gas evolution from their model is shown in Fig. 2.5. Only the very low pressure of 10^{-15} bar was modeled, but it still gives useful data on the process and order of vaporization of different oxide and gas species.

A top-down approach has been taken in the study by Lamboley [46], who developed a Model-Based Systems Engineering (MBSE) model of a lunar oxygen production plant based on the solar pyrolysis process. The whole process path has been considered from bulk regolith intake through oxygen and byproduct separation, handling, and storage. The proposed concept reactor is shown in Fig. 2.6. This reactor uses a batch process with minimal preparation of regolith (sieving), concentrated solar energy as the heat source, dynamic condensation surfaces for producing metal condensate, and an oxygen filtration and storage system using a cryo-pump and a liquid oxygen storage tank.

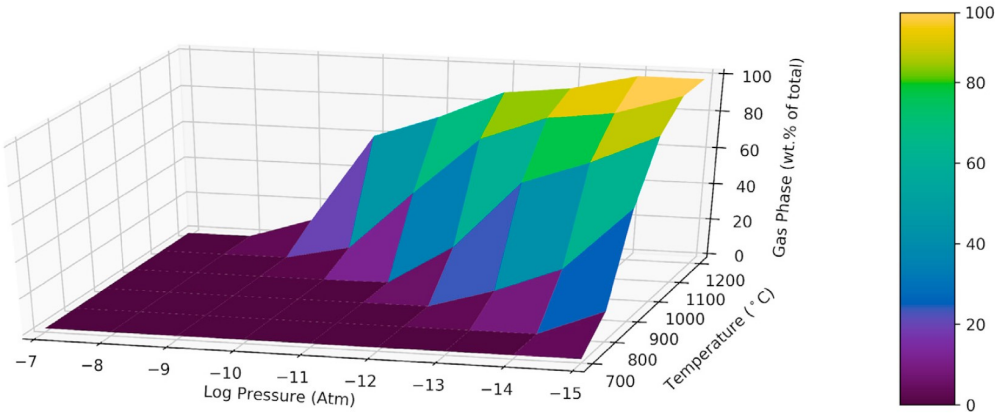

Figure 2.5 Gas evolution of at thermochemical equilibrium at pressure and temperature from [15]

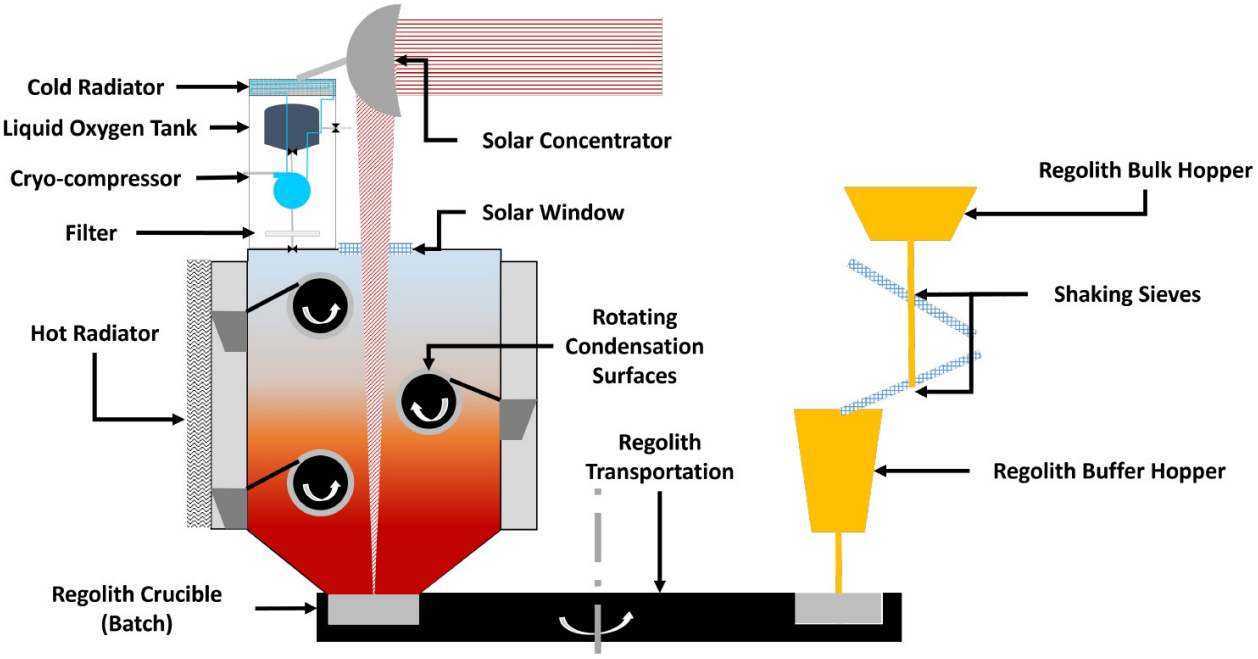

Figure 2.6 A pyrolysis reactor for oxygen and metal processing proposed by Lamboley [46]

Oxygen yield The main underlying parameter for the choice of an oxygen extraction process to be used on the lunar surface is the oxygen yield, defined simply in Eq. 2.3 as a fraction of oxygen mass to the initial (unbeneficiated) bulk regolith mass. This is also how yield will be defined in this thesis, as some define yields slightly differently. For example, Steurer and Nerad define it as a gaseous oxygen fraction of the total mass of gas ($\eta_{oxygen} = \frac{m_{O_2}}{m_{gas}}$). Assuming all regolith would vaporize, both definitions would deliver the same yield value. Conditions where part of the regolith stays solid or liquid might be beneficial to the process, so the definition in Eq. 2.3 is more general and is used by most studies [9, 11, 14] and the universal framework for space resource utilization by Hadler et al. [34].

The oxygen yield values in literature lay between 2 and 24% as already listed in Tab. 2.1. Steurer and Nerad [37] state that approximately half of all oxygen contained in each oxide can be extracted and that the region above 2000 K is of practical interest for oxygen production due to the higher pressures and the associated useful throughput rate of the reactor. These statements appear not to consider the difference

between molecular and atomic oxygen, which should be made due to the aggressive oxidation behavior of atomic oxygen. They point out that efficient oxygen and metal recovery is possible with rapid cooling of the vapor phase to around 500 K. This has to happen faster than the reoxidation of components to the original oxide.

Senior [11] predicted pressures of 0.013 mbar to 0.13 mbar for pyrolysis at temperatures of 2000 K to 2200 K. The resulting O_2 yield was estimated between 2% and 20%. The vaporization of silicon, magnesium, and iron in a lower temperature regime would result in a yield of 2.4% to 12%, while extraction from calcium and aluminum could increase the yield value to 6.3% to 21%. These values account for only partial vaporization between 25% and 100%, and a decreased yield efficiency of 60%. This leads to a proposed lower bound of 15% and an upper bound of 60% for the estimation of realistic yields from ideal values. They also state that condensation of metal-containing species is of major importance for high oxygen yields. Oxygen recovery and storage still present a problem that has not been investigated enough. Senior also states that the best solution for the protection of chamber hardware from the melt would be to use the regolith itself as an insulating boundary due to its low thermal conductivity. This technique has been applied in the experimental setup in section 3.

Senior recommends the pyrolysis temperatures between 2000 K and 2200 K because above these temperatures molecular oxygen begins to dissociate into atomic oxygen, which is a very reactive atom that can quickly reoxidize the suboxide species before their recondensation, decreasing reactor efficiency. It can also be detrimental to the reactor surfaces and oxygen processing hardware. Atomic oxygen should, therefore, not be considered in oxygen yield values. This presents the main difference between the considerations of previous work and Senior because oxygen dissociation was neglected by Steurer and Nerad [37].

Energy requirements The energy required for vapor pyrolysis has been estimated by Steurer and Nerad [37] with approximately 29.6 kW h t^{-1} of O_2 which accounts for heating of the bulk regolith and cooling of the condensation surfaces. Providing 65% of power for heating with concentrated solar, the power requirements can be split up in the direct solar power of 19.2 kW h t^{-1} of O_2 and electric power of 10.4 kW h t^{-1} of O_2. These power requirements are valid for the high oxygen yield of 24%, although they show that a considerable amount of power can be supplied by concentrated solar, reducing required photovoltaic or nuclear power loads. A lower yield would require comparatively more energy and a higher total power, but the ratio of concentrated solar to cooling power would stay similar, requiring more concentrated solar and electric capacity.

Solar experiments Concentrated solar has been proposed as a power source for a major amount of the required power, as described in the previous paragraph. Mattchet [14], and Sauerborn [44] have taken this theoretical idea and done experimental studies of vapor phase pyrolysis in solar concentration devices. Matchett has done pyrolysis experiments using relevant simple oxides ($FeTiO_3$, Al_2O_3, $MgSiO_3$) and the MLS-1A simulant while Sauerborn used other simple oxides (MgO, Fe2O3, SiO2), oxide mixtures, and JSC-1 simulant. They both demonstrated pyrolysis in a vacuum environment, although they did not produce quantitative measurements of the process.

Sauerborn's experiments at the DLR Solar Furnace (Fig. 2.7a) with the JSC-1A regolith simulant were performed at temperatures of 1300 °C to 1500 °C at vacuum pressures of 10^{-5} mbar to 10^{-4} mbar. An increase in the oxygen partial pressure, stemming from the simulant, was measured by an RGA during the solar exposure. EDX measurements of produced samples also showed lower Na, K, P, and O amounts in the sample, but a qualitative conclusion could not be drawn. Nonetheless, this study proved solar-vapor pyrolysis as proof of principle for oxygen production from lunar regolith simulants.

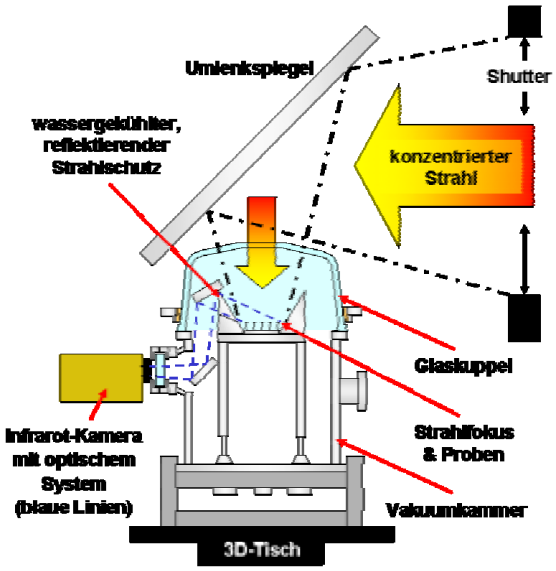

(a) Setup

(b) Cupola

Figure 2.7 Solar-vapor pyrolysis setup by Sauerborn [44]: (a) setup overview and (b) cracked glass cupola.

A much smaller prototype setup with a Fresnel lens (Fig. 2.8a) was used by Matchett for pyrolysis of lunar simulant MLS-1A. Bulk samples have been fully melted and partially vaporized at pressures of 10^{-4} mbar to 1 mbar and temperatures of 900 °C to 1400 °C with maximum temperatures reaching to approximately 1900 °C.A maximum mass loss of 10% due to vaporization was observed. This mass loss cannot be attributed to full dissociation and oxygen production. It can likely be attributed to vaporized regolith deposition on vacuum chamber surfaces and the solar window, as shown in Fig. 2.8b. EDX measurements of the melted regolith samples have shown an oxygen decrease which can be attributed to the dissociation of oxides.

(a) Setup

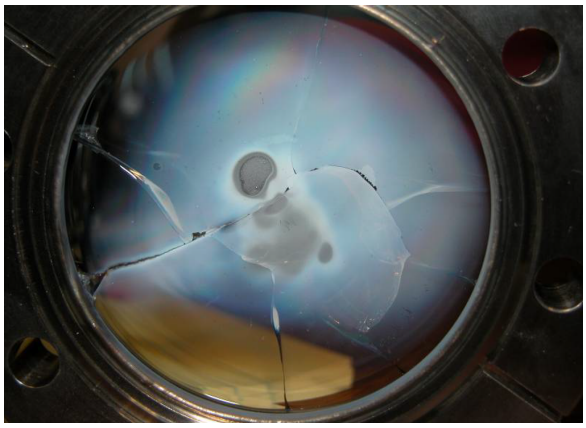

(b) Window

Figure 2.8 Solar-vapor pyrolysis setup by Matchett [14]: (a) setup overview and (b) cracked solar window.

A major problem for both experiments, by Sauerborn and by Matchett, was the condensation of vapor on the vacuum window (Fig. 2.8b) and the glass cupola (Fig. 2.7b), which reduced the transmission of light and resulted in a thermal failure of the glass during or after the experiment.

2.3.4 Vapor condensation, oxygen capture, and processing

Vaporization of lunar regolith is only the first part of an effective oxygen extraction process. The metal and suboxide species contained in the vapor phase must be recondensed rapidly at a rate that prevents reoxidation and formation of original oxides [37]. Senior [11] states that the condensation surfaces have to be hot enough so that oxygen does not condense with other species. A suggested upper limit for the condensation temperature is 500 K to 600 K [11]. Through variation of the condensing temperature, metal and suboxide species can be separated in the process of metal distillation [11, 47]. Shaw et al. [15] has theoretically studied this process, producing solid FeO, Na, and K from regolith vapor in ultra-high vacuum.

After condensation of metal species, the remaining gaseous oxygen has to be removed from the chamber and stored for further use. Several oxygen collection and storage methods have been proposed. Steurer [37] proposed letting the oxygen flow into a balloon, where the lunar vacuum outside the balloon provides the pumping power. Another, more terrestrial, process is using staged compressors/vacuum pumps to produce pressurized or even liquefied oxygen [11, 46]. A molecular sieve could be implemented to trap oxygen at low pressures while releasing it at higher pressures and saving a certain amount of mechanical work compared to mechanical compression [11].

2.4 Solar energy

Solar energy is another important factor in the solar vapor pyrolysis process and an overall important resource on the lunar surface. It can be used for electricity generation through solar panels or alternatively as concentrated solar power for heating applications, such as high-temperature ISRU processes [12], or thermal energy storage [48].

2.4.1 Solar radiation

The amount of solar radiation reaching the lunar surface is significantly higher than the Earth's surface. The average irradiance a the lunar surface reaches 1363 $\mathrm{W\,m^{-2}}$. As the Moon travels on its orbit around the Earth, the irradiance also fluctuates due to the varying distance to the Sun. Lunar surface irradiance fluctuates between 1310 $\mathrm{W\,m^{-2}}$ and 1415 $\mathrm{W\,m^{-2}}$. [49] These values are at least 30% higher than the solar irradiance values on the Earth's surface, which lie at approximately 1000 $\mathrm{W\,m^{-2}}$. Terrestrial solar irradiance is influenced not only by the orbital position of Earth but even more so by the atmospheric losses. The atmosphere reduces the total solar irradiance and changes the spectral properties of light reaching Earth's surface. This is shown in Fig. 2.9. The solar spectrum outside Earth's atmosphere, which is also applicable at the lunar surface, is the AM0 (Air Mass 0) spectrum represented by the ASTM E490e data set [50]. The terrestrial spectrum, accounting for atmospheric losses, is marked AM1.5 (Air Mass 1.5) represented by the ASTM G173 data set [51].

Solar irradiance is also dependent on the geographical location on Earth's surface. It can reach higher values of up to 1100 $\mathrm{W\,m^{-2}}$ in equatorial regions, where solar elevation angles reach 90°. Solar experiments for this thesis have been performed in Cologne, Germany, which receives a slightly lower solar irradiance. Sauerborn gives the highest measured value of 980 $\mathrm{W\,m^{-2}}$ for direct solar irradiance from the Weather archive at the DLR Solar Furnace in Cologne. Average clear and cloud-free days reach between 650 $\mathrm{W\,m^{-2}}$ and 850 $\mathrm{W\,m^{-2}}$ at midday. [44]

The lack of an Earth-like atmosphere on the Moon makes sunlight a promising resource on the lunar surface since significantly more power is available. A problem on the lunar surface is the long lunar day-night cycles due to the lunar rotation period of 27.322 Earth days. This leads to 14 day-long periods of

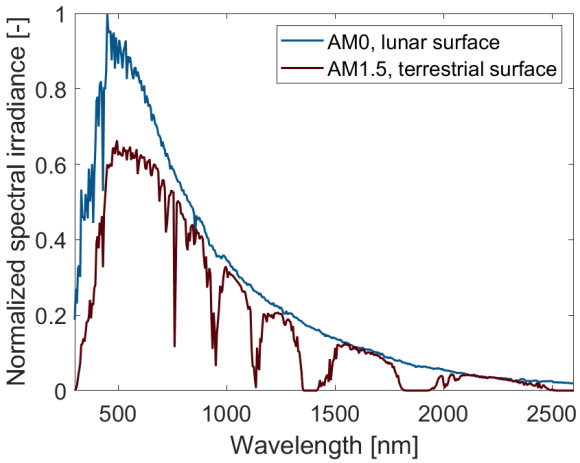

Figure 2.9 Solar spectrum at the lunar surface (AM0) and at Earth's surface (AM1.5)

sunlight and 14 days of darkness. [49]. This presents a considerable problem for solar-powered hardware and human activity during the lunar night when no solar-driven ISRU can be running. A possible solution to this problem is setting a lunar base and human activities at the lunar south pole, where regions with nearly-permanent sunlight exist and illumination periods exceed 70% [52].

2.4.2 Spectral properties of regolith

Since the main topic of this thesis concerns heating the regolith with focused solar power, it is useful to look at the spectral properties of bulk regolith. These properties influence the efficiency of solar heating due to the varying absorption ability of different regolith and simulant samples. Mare and highlands regolith represent the major groups in this regard, with highlands regolith being visibly lighter on average than mare regolith, thus reflecting more light in the visible spectrum. A darker regolith will get heated more due to more light being absorbed. Absorption of light is governed by Eq. 2.11, where $\tau(\lambda)$ is wavelength-dependent transmittance, $\rho(\lambda)$ is the wavelength-dependent reflectance, and $\alpha(\lambda)$ the wavelength-dependent absorbance. Assuming regolith as an opaque surface $\tau(\lambda) = 0$ the total absorbance can be written in Eq. 2.12. [53]

$$\tau(\lambda) + \rho(\lambda) + \alpha(\lambda) = 1 \tag{2.11}$$

$$\alpha = (1 - \rho) \tag{2.12}$$

These properties are shown well in the spectral analyses of the Apollo samples done by the Lunar Soil Characterization Consortium [54]. Fig. 2.10b shows spectral reflectances for the mare 15071 and highlands 61221 lunar soil samples, which influence the absorbance of the solar spectrum into the regolith. The absorbed solar spectra calculated from these reflectances and the AM0 solar spectrum are shown in Fig. 2.10a.

2.4.3 Solar concentration

Solar irradiance at the lunar or terrestrial surfaces is not high enough to heat regolith to temperatures relevant for pyrolysis, which are above 1300 K. Regolith can be heated through the use of concentrated sunlight similarly to the way concentrated solar power is used on Earth for electricity generation in solar-thermal power plants.

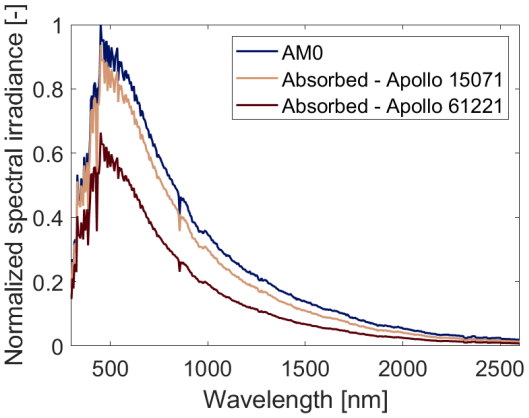

(a) Absorbed solar spectrum

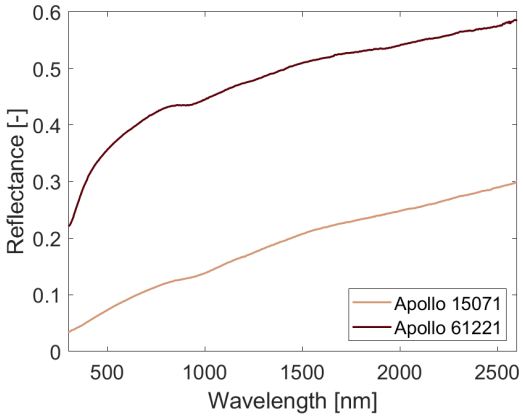

(b) Spectral reflectance

Figure 2.10 Absorbed solar spectra in comparison to the Air Mass 0 solar spectrum and the corresponding spectral reflectances of the Apollo samples 15701 and 61221 as the lower and upper reflectance bound respectively [54]

Solar concentration systems Solar-thermal power plants and solar furnaces mostly use mirrors to redirect and concentrate light. These can be divided into direct and indirect concentrators. The first are cylindrical or dish parabolic mirrors which concentrate the incoming solar radiation to a focal point or line, where a fluid medium can be heated. Indirect concentrators are systems composed of one or more heliostats, which are flat mirrors that track the Sun and reflect it to a desired location, where it can be concentrated. These mirrors are flat and do not concentrate the light. Such heliostats are used in solar towers to focus a large surface area on a single area on the tower and heat a storage medium. Most solar furnaces also use heliostats to capture sunlight but have secondary parabolic mirrors, which focus the light. A similar system was also used for the pyrolysis experiment by Sauerborn [44, 55]. Smaller solar concentrating systems can also use refractive optical elements instead of mirrors, for example, Fresnel lenses. The main difference compared to mirror systems is that the light travels through the concentrating optical element and gets partially absorbed by the lens material. Therefore, mirror systems are usually more efficient than lens systems for solar concentration applications. [56]

Solar concentration ratio An important metric for defining the performance of solar concentration systems in the solar concentration ratio as defined in Eq. 2.13, where E_c is the solar flux density at the concentrated spot, A the beam cross-sectional area at the concentrated spot, and E_{sun} the direct solar irradiance of the environment. An average direct solar irradiance of $1000\,\mathrm{W\,m^{-2}}$ is taken for terrestrial systems and an average value of $1363\,\mathrm{W\,m^{-2}}$ is taken for lunar surface systems. [13]

$$C = \frac{\frac{1}{A}\int_A E_c\,dA}{E_{sun}} \tag{2.13}$$

A simplified relationship between solar concentration ratio C and the regolith surface temperature can be defined through the absorption coefficient in Eq. 2.14 [13]. Using this coefficient and the calculated solar concentration ratio, a surface temperature of the regolith under lunar or terrestrial solar irradiance can be estimated with data shown in Fig. 2.11.

$$\eta_{absorbtion} = \frac{\Phi_{abs}}{\Phi_{solar}} = 1 - \frac{\sigma T^4}{E_s C} \tag{2.14}$$

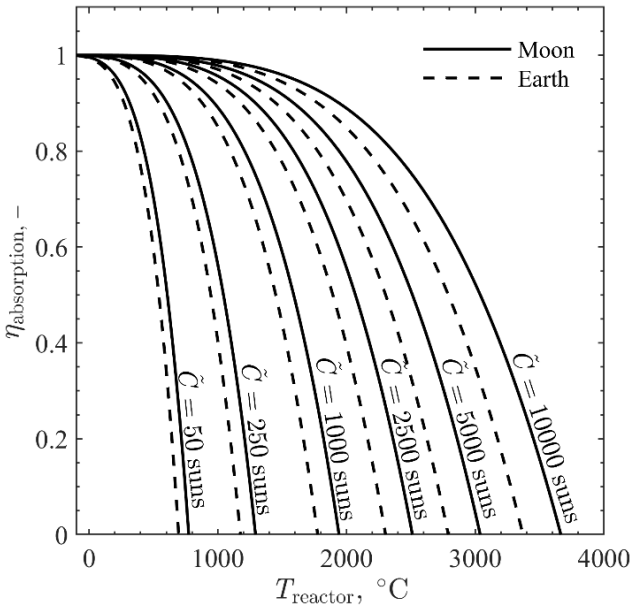

Figure 2.11 Relationship between solar concentration, absorption efficiency, and regolith surface temperature as defined by Clendenen [13]

Lunar applications of concentrated solar power The reduced lunar gravity and lack of atmospheric wind are beneficial for large sunlight collecting or concentrating structures since they can be made very lightweight. Mylar or similar materials with reflective coatings can be stored in a small volume for the launch and for the journey to the Moon. There they can be unfolded and tensioned on large lightweight structures to assume the desired shape for reflection or concentration of sunlight. Large reflecting heliostats can be placed at high peaks where the solar illumination is less interrupted and reflect the light to other areas. [18]

A habitat concept has been proposed by Herzig et al. [57], where large solar mirrors are placed on top of inflated habitat structures to provide light for greenhouses and habitat inhabitants. Silver-coated Kapton or Mylar membranes are tensioned over lightweight truss structures, and an electrostatic technique is used for adjusting the mirror's focal length. Similar structures could also be used for the collection and concentration of sunlight for ISRU reactors.

Several ISRU techniques could benefit from such a solar concentration system. Solar-vapor pyrolysis requires such a concentration system, but also other high-temperature ISRU processes would benefit from direct solar heating to reduce electrical power requirements, for example, ilmenite reduction. [14]

3 Experimental demonstration of solar vapor pyrolysis

The following chapter presents the vacuum pyrolysis experiments using EAC-1A regolith simulant [24] in a purpose-built small-scale high-vacuum solar furnace. The goal is to show the feasibility of creating needed conditions for pyrolysis and the reduction of oxygen content in the sample. At the beginning, the experimental setup, its development variants, its performance compared to lunar conditions, and the experimental procedure are described. Afterward, the results and the post-experiment analysis of produced samples are given and discussed.

3.1 Solar-pyrolysis experimental setup

The experimental work was carried out on the setup shown in Fig. 3.1. It was designed from the ground up as a part of an internship at Spaceship EAC at the European Astronaut Center. Building, testing, and first experiments were done as a part of this thesis. The main challenge of this experimental setup is that the process is best suited for the vacuum environment of the Moon. On Earth, the primary problem is creating and maintaining the required high vacuum while producing gas from the regolith sample in the vacuum chamber.

The experimental setup consists of a vacuum chamber, an analysis section, and an optical system, which is used for the concentration of sunlight into the vacuum chamber to heat the sample. The optical system uses a heliostat mirror to reflect sunlight onto a horizontally positioned lens. This is done to enable the experiments to be carried out in winter when the solar elevation angles are small. The horizontally positioned Fresnel lens focuses the light through a quartz glass window and onto the surface of the regolith sample in a crucible inside the vacuum chamber. While the sunlight is heating the sample, the pressure of the vacuum chamber, as well as the surface temperature of the regolith, is being recorded using an pressure sensors mounted on the chamber and an IR camera.

Initial outgassing and vaporization of the regolith sample produces gas and results in a pressure increase. To avoid detrimental effects to the turbomolecular pump or the RGA, measures have been taken to handle this initially unknown pressure increase. An additional unknown was the temperature stability of the solar window. A potential window failure could lead to significant damage to the pump or RGA and needed to be tested [14, 44]. During the tests, described in section 3.3, four designs were developed to iteratively improve the pumping, the pressure stability, and the reliable use of the RGA. The resulting samples were therefore created on different vacuum setups and cannot be compared to each other in terms of gas production or pumping conditions. All samples for each of the following setup versions, including their pressures, temperatures, and solar irradiance, are shown and described under results in section 3.3. The setups themselves are described in the following section.

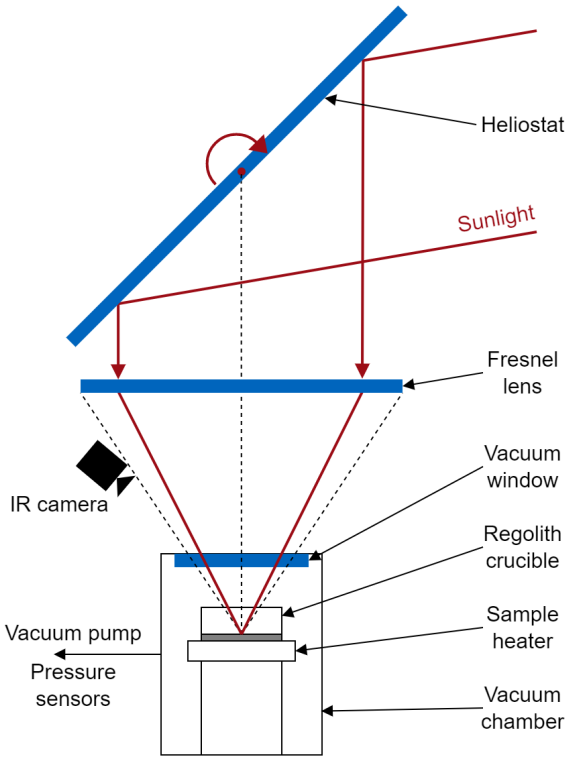

(a) Setup diagram

(b) Setup photo

Figure 3.1 Overview of the experimental setup

3.1.1 Vacuum system

Four variants of the vacuum setup were developed for solar experiments. The first was used as a closed system during the solar exposure so the potential rapid pressure spike would not damage the delicate equipment in the analysis section. The second uses a vacuum pump continuously during the solar exposure after verification that the pressure spikes do not present a problem for the pump and that the window does not reach temperatures considered problematic for its stability. The third and fourth setup designs aim to improve pressure conditions in the chamber and the analysis section.

Version 1: Vacuum lock The first version, "Vacuum lock" (Fig. 3.2), connects the analysis section with the chamber using two valves with a flexible tube in between. The valves can be used in the same manner as a canal lock: closing valve V2, opening valve V1 to let the chamber gasses in the lock volume, closing valve V1, and opening valve V2 to let the gas through to the analysis section without a direct connection to the chamber. The motivation behind this positioning is to protect the RGA and the turbopump from a sudden pressure rise, either due to sample outgassing or window cracking due to thermal stress induced by the focused sunlight. Window failures have been observed by Matchett [14] on a flat window and by Sauerborn [44] on a glass cupola during solar exposure or the cool-down phase.

The first experiment used this setup and produced melted samples 1 and 2 shown in Tab. 3.1 and 3.3. These results show the major flaw of this design. Pressure in this closed system peaks around 0.1 mbar to

1 mbar, which is out of the expected range needed for vapor pyrolysis on this setup, below approximately 10^{-3} mbar to 10^{-4} mbar, and far above the measurement limit of the RGA, which lies at 10^{-5} mbar. The vacuum lock is shown to let too much gas through to the analysis section at these high pressure peaks in the vacuum chamber.

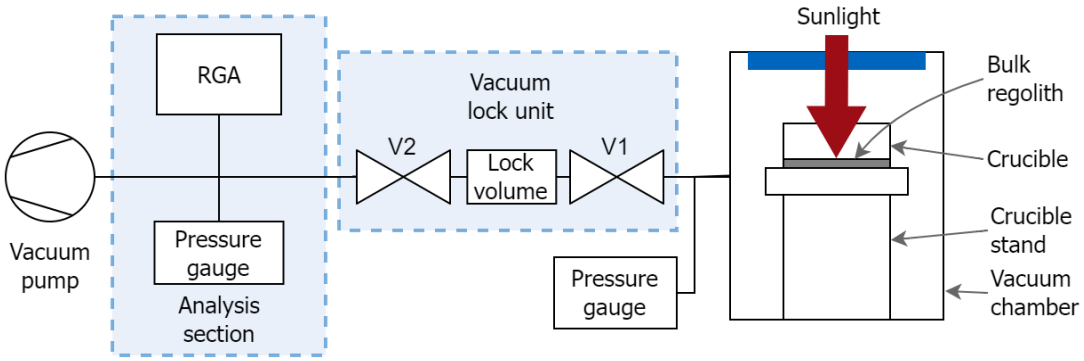

Figure 3.2 Experimental setup - Version 1

Version 2: Direct connection The second version, "Direct connection" (Fig. 3.3), connected the turbopump directly to the chamber with one valve (V1). The valve is used for sealing the baked and evacuated chamber when moving the setup from the lab to the outside for solar experiments because pumps had to be shut down to not be damaged by the vibrations during transportation. The valve is kept open during solar exposures to pump the chamber continuously.

The second experiment was done with this setup to test the ability to pump the chamber continuously, resulting in lower peak pressure than the version 1. Melted samples 3-7 have been produced with this setup and are listed in Tab. 3.1 and 3.3.

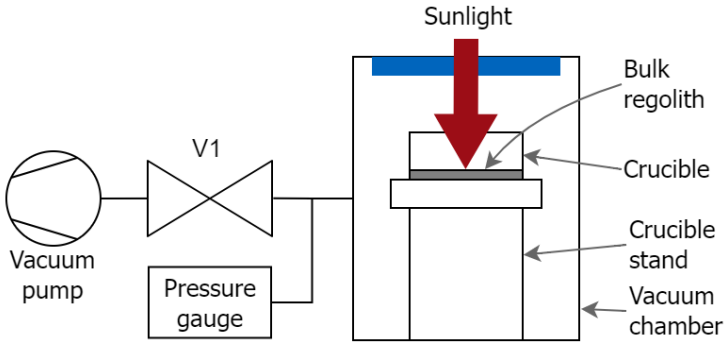

Figure 3.3 Experimental setup - Version 2

Version 3: Two pumps The third version, "Two pumps" (Fig. 3.4), is built to allow for continuous pumping of the chamber while the analysis section is disconnected. It features an additional turbopump connected to the chamber through the V2 valve. The analysis section is separated from the chamber with the V1 valve. The chamber can be pumped continuously during an experiment by opening the V2 valve. V1 valve can be opened when the pressure peak in the chamber falls below the pressure limit of the RGA to take a reading of the gas composition.

Version 4: Metering valve The fourth version, "Metering valve" (Fig. 3.5), has been planned and built but has not been tested in the frame of this thesis and serves as a basis for the outlook of this thesis.

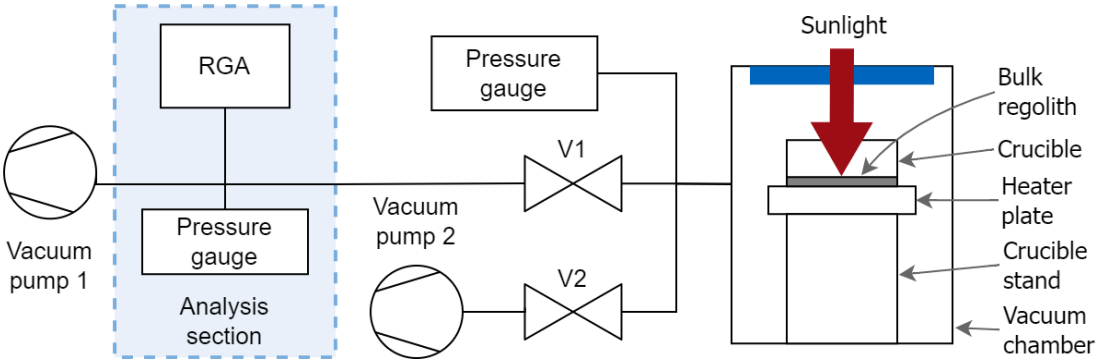

Figure 3.4 Experimental setup - Version 3

It aims to solve the problem of the pressure difference between the chamber and the analysis section. A metering valve is added in series to the V1 valve in this setup. It is used to let small amounts of gas pass from the chamber to the analysis section in a controlled manner during a solar exposure to keep the pressure below the RGA pressure limit.

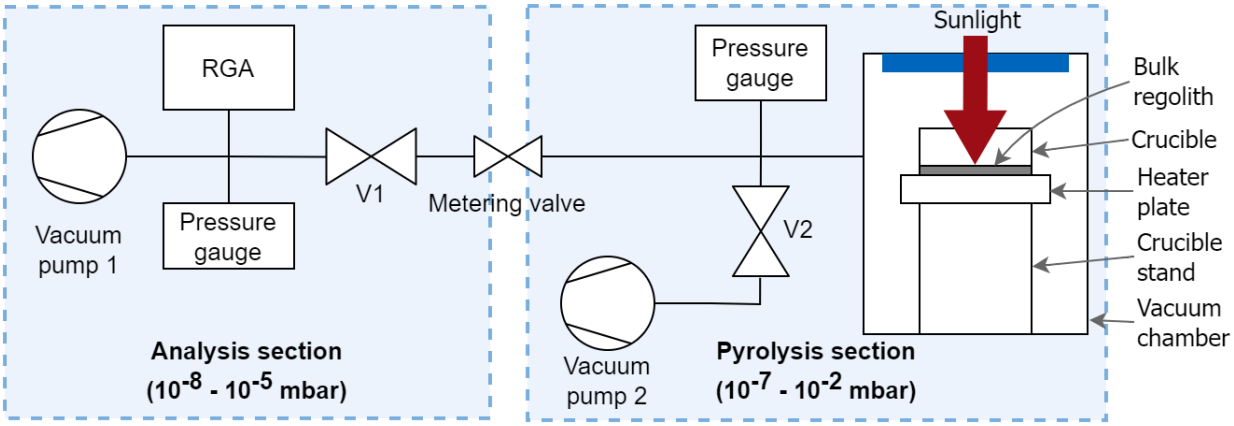

Figure 3.5 Experimental setup - Version 4

3.1.2 Chamber and sample bake-out

Creating high or ultra-high vacuum conditions in a chamber is only possible with good pumping conditions, eliminating any virtual leaks and desorption of adsorbed molecules. Leaks have been reduced to a negligible amount through UHV vacuum hardware which uses copper gaskets for the high vacuum portion of the system. Pumping conditions are ideal when the pump is connected the closest to the chamber and with the largest diameter tubing possible. Through the previously described iterations of the setup, the pumping conditions were improved but were still limited due to the available tubing and the required use of at least one valve for sealing the evacuated chamber.

The last important consideration for achieving ultra-high vacuum is off-gassing, which is eliminated with baking [58, 59]. Internal surfaces must reach a temperature where most adsorbed molecules desorb and are pumped out of the system. Bake-out for versions 1 and 2 is implemented with heating tapes glued to the outside of the vacuum vessels. Large parts of the system were wrapped in aluminum foil for additional insulation to achieve homogeneity. The surface of the heating tapes reached above 170 °C. The regolith sample inside the chamber reached between 125 °C to 140 °C. In setup version 3, a sample heater is implemented to heat the sample to even higher temperatures above 300 °C.

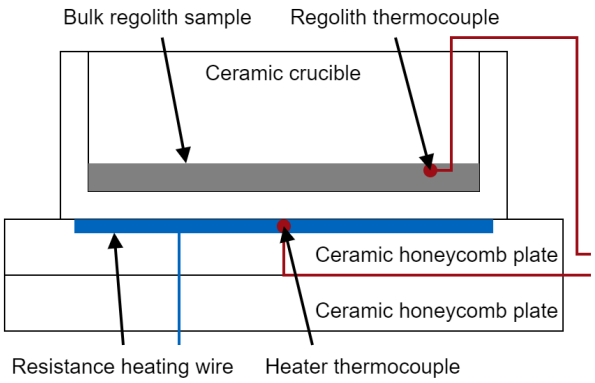

(a) Heater diagram

(b) Heater in the vacuum chamber

Figure 3.6 In-Vacuum heater for the regolith crucible

Regolith crucible heater The temperature reached in the regolith sample during baking using external heaters is insufficient to bake the sample sufficiently [58, 59]. The regolith sample presents a significant source of outgassing during the experiment due to the large adsorption surface area of the regolith simulant. An internal sample heater (Fig. 3.6) has been implemented to aid the baking process by heating the bulk regolith sample in the crucible. Several sample heating concepts have been considered, including solar, inductive, and resistive options. It was decided against the use of solar heating for the purpose of baking. Solar heating does not provide a homogenous heat flux on the whole regolith surface but a gaussian distribution of flux which would result in a hotspot in the middle of the crucible or a too low heat flux distribution towards the edges of the crucible. Therefore, an electrically powered solution was chosen to bake the system. Resistive heating was chosen instead of inductive heating due to its lower hardware requirements and ease of implementation.

The flat heater is made of two alumina honeycomb plates (Fig. 3.6a) with channels cut into the surface to recess the resistance wire below the surface, so the heater lays flat on the supporting surface, and the crucible lays flat on the heater. This heater is used in version 3 of the setup to bake the sample to at least 300 °C for melt samples 8 to 11 and 400 °C for melt sample 12 due to an improvement in heater filament wiring.

3.1.3 Sensors and measurement

During the experiments, pressure and temperature are constantly measured. The following describes the sensors used in the experiments.

Pressure measurement Pressure is measured at two locations in the vacuum system. The first location is in the pyrolysis chamber, measured by a Kurt J. Lesker CCPG-H2-6 Cold-cathode/Pirani combination gauge connected directly to the chamber opposite the pump connection. The KJL-SPARC Gauge Display is used for the readout of measured values and data logging through an RS232 serial connection on a computer. The second combination gauge Pfeiffer PKR 251 is connected in the analysis section to monitor the pressure limits for the RGA and is logged only when the RGA is recording.

Temperature measurement Temperature of the sample is measured by two methods. The first utilizes two Type-K thermocouples (Fig. 3.6a) connected to an Omega HH306A data logger and logged on a computer through an RS232 serial connection. One of the thermocouples is embedded in the sample bake-out heater below the crucible to monitor the temperatures of the heater. The second thermocouple is embedded in the regolith at the edge of the crucible to primarily monitor regolith temperature during the bake-out of the sample. The thermocouples have shown to not be helpful during the experiment itself since the low thermal conductivity of regolith does not allow the locations of these sensors to rise to values that would give insight into the process. The thermocouple in the regolith also tended to become loose and rise above the regolith sample during transportation of the setup from the lab to the outside, losing conductive contact with the sample.

The more effective temperature measurement is done by an Optris IR camera looking through the solar window and placed just outside the concentrated solar beam (Fig. 3.1b). The information logged from the camera id the peak temperature measured at an emissivity of 0.98. This emissivity has been taken based on the value range 0.973 to 0.984 given by Ball [60] for measurement of molten basalt in vulcanology applications. The peak temperature is chosen due to the inconstant position of the beam during an experiment, making an area-averaged measurement of the whole heated spot unpractical. The peak temperature is not a measurement of the temperature of the whole melt. However, because of convection and increased conduction in a melt, it is assumed that the peak temperature is a good indicator of temperature not only on the surface but also deeper in the melt.

This measurement's significant uncertainty is that the camera measures IR radiation that passes through a quartz glass window. Quartz glass absorbs specific wavelengths in the IR spectrum, reducing measurement accuracy. This accuracy was checked with an experiment using a microwave heated regolith experiment setup, which could produce high-temperature regolith melt in the atmosphere. The camera was pointed and focused on a regolith sample heated to different temperatures. Peak temperatures were measured with the camera in three consecutive steps: (1) a direct view of the melt, (2) the vacuum glass window between the camera and the sample, and (3) a repeated measurement without the quartz glass in front of the camera. The average temperature error of 8 measurement sets was 14.5 °C for the range of 1000 °C to 1450 °C (Supplementary table A.2). Another indication that the window transmittance is not a considerable problem is the camera's spectral measurement range of 850 nm to 1100 nm which is in the region of high and constant transmittance of around 0.9 for the quartz window as shown in Fig. 3.7b.

3.1.4 Solar irradiance and efficiency losses

A primary consideration when using sunlight for processes being developed for the lunar surface is the difference in solar irradiance on the lunar or terrestrial surface and the resulting solar spectrum that irradiates the sample. The experimental setup uses the sunlight spectrum available at the Earth's surface, which is considerably lower in total power than the spectrum of the light illuminating the surface of the Moon, as described in section 2.4. Fig. 3.7a shows the irradiance spectra of the sunlight at the Earth's surface and at the lunar surface. The spectrum at the lunar surface is represented by the ASTM E490e "Air Mass Zero" reference spectrum [50], and the Earth's surface spectrum is represented by the ASTM G173 "Air Mass 1.5" reference spectrum [51]. The total radiant flux reaching the surface is given in Eq. 3.1, with E_{sun} being the solar irradiance based on the ASTM G173 spectrum and A_{eff} the effective collection area dependent. This effective collection area is implemented in the calculation because the lens is only partially illuminated at low solar elevation angle α_{sun} due to the relative cross sections of the beam at the lens aperture and the lens area. ρ_{mirror}, τ_{lens}, and τ_{window} are total transmission or reflection efficiencies of the optical elements which represent the loss of total radiative flux.

$$\Phi_{in} = \tau_{window}\tau_{lens}\rho_{mirror}A_{eff}E_{sun} \tag{3.1}$$

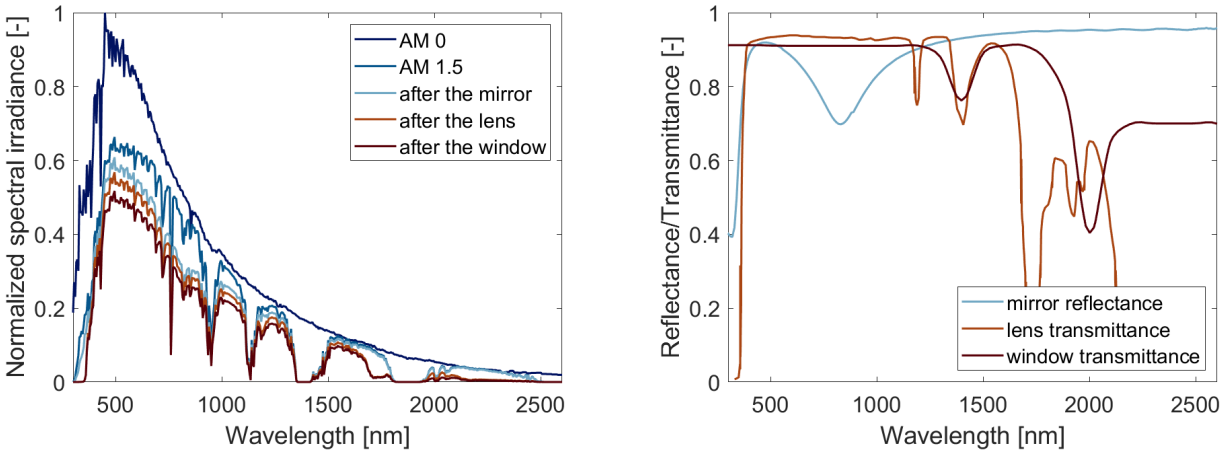

(a) Normalized irradiance

(b) Reflectance/Transmittance

Figure 3.7 Normalized sunlight spectra at the lunar surface (Air Mass 0), at the Earth's surface (Air Mass 1.5), and spectra inside of the experimental setup after reflection or transmission by optical elements (a) and the reflectance or transmittance of optical elements (b)

Taking the spectrum of the incoming sunlight and weighing it with the spectral properties of the optical elements, a changed light spectrum and losses for each optical element can be calculated. These are calculated with the weighing equation Eq. 3.2, with Φ_λ being the spectral flux at the optical surface and τ_λ the spectral transmittance of the optical element. Fig. 3.8 shows the light spectra weighed by the optical losses. The lowest shown spectrum shown in Fig. 3.7a is the spectrum of the light that reaches the regolith sample in the vacuum chamber. Total losses of each single optical element are 14.7% for the mirror (accounting for mirror reflectance ρ_{mirror}), 12.4% for the lens (accounting for τ_{lens} and A_{eff}), and 9.6% for the vacuum window (accounting for τ_{window}). The total spectra-weighed loss of the solar radiative flux when the beam reaches the regolith sample is 32.7 %, which combines τ_{window}, τ_{lens}, R_{mirror}, and A_{eff}.

$$\tau = \frac{\sum \Phi_\lambda \tau_\lambda}{\sum \Phi_\lambda} \tag{3.2}$$

The spectral reflectance $R_{mirror,\lambda}$ or transmittances $\tau_{window,\lambda}$ and $\tau_{lens,\lambda}$ are shown in Fig. 3.7b and their influence on the light spectrum in Fig. 3.7a. The heliostat mirror's reflectance is unknown; therefore, it is approximated by the data for an unprotected aluminum coated mirror taken from Thorlabs [61]. The lens transmittance is taken from its manufacturer Edmund optics [62], and the window transmittance is taken from its manufacturer Kurt J. Lesker Inc. [63].

Due to the uncertainty of mirror reflectance, the irradiance loss at the mirror was also measured with a solar irradiance sensor multiple times during the experimental runs. The sensor used was a Voltcraft PL-110SM Luxmeter with a measurement error of $\pm 10\,\mathrm{W\,m^{-2}}$ or $\pm 5\,\%$ and a precision of $0.1\,\mathrm{W\,m^{-2}}$. Solar irradiance of the reflected beam after the mirror was measured at two different points at the higher and lower end of the mirror on the shutter of the lens. The irradiance point values were then averaged for each measurement. The irradiance loss between the measured environmental irradiance E_s and the beam after the mirror averaged across all 16 measurements (supplementary table A.1) resulted in a loss of 15.04 % with a standard deviation of 1.1 %. This is only a slight deviation from the calculated value of 14.96 %. Therefore, the calculated value of 32.7 % has been taken as the total losses between the solar irradiance and for calculating solar power at the sample surface.

This incoming solar energy flux does not get absorbed in its entirety due to the reflectance of the regolith sample. There is no published information on EAC-1A reflectance; therefore, Apollo data [54] has been

taken to estimate the reflectance of the sample. The spectral conditions were calculated for such an experiment system on lunar and terrestrial surfaces. Two Apollo reflectance spectra, a maria sample 15071 and a highland sample 61221 [54] have been taken to represent the assumed best and worst cases for absorption, respectively. These were combined with the light spectrum at the regolith surface from Fig. 3.7 shown in Fig. 3.8. The Apollo reflectances lead to a loss of 40.51 % and 60.45 %, respectively, for the terrestrial case. For the lunar case, the reflectance losses lie at 42.75 % and 61.82 %, respectively. These reflectance losses $R_{regolith}$ are used to calculate the estimated absorbed flux Φ_{abs} during experimental exposures with Eq. 3.3 [53] as well as for the modelling considerations in section 5.2. The worst and best case absorbed flux for each solar exposure calculated with these reflectance values is listed in Tab. 3.1 in section 3.3.

$$\Phi_{abs} = (1 - R_{regolith})\Phi_{in} \tag{3.3}$$

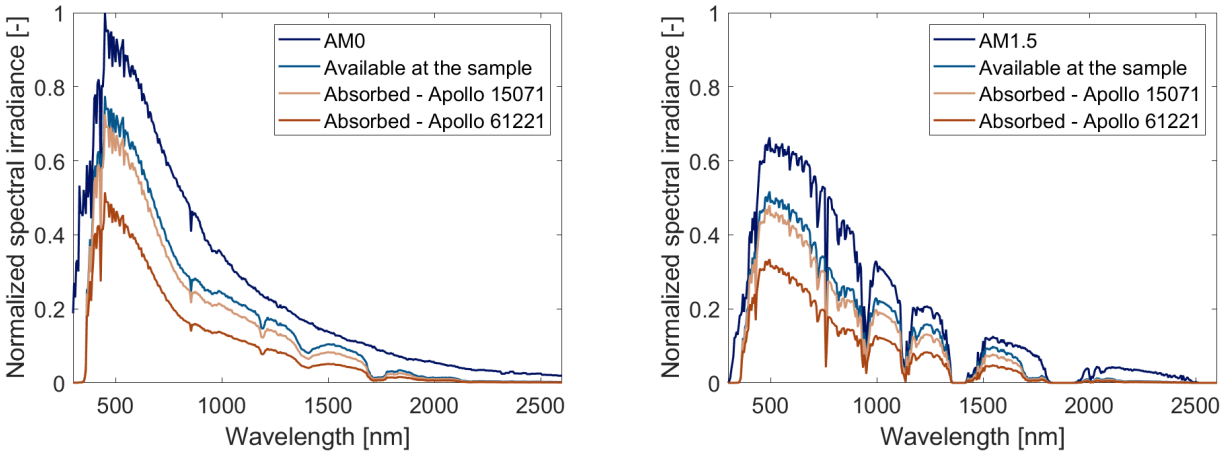

(a) AM 0 **(b)** AM 1.5

Figure 3.8 Absorbed solar flux Φ_{abs} based on the Apollo reflectance spectra 15071 and 61221 applied to the (a) AM 0 and (b) AM 1.5 spectra, and accounting for optical losses in the experimental setup

3.2 Experiment procedure

Solar experiments were run in a cycle of two days: a bake-out and a solar exposure day. It is necessary to describe the whole procedure because the pumping, baking, and primarily the setup transportation process might influence the results.

A bake-out day constituted mounting the crucible with regolith into the chamber, sealing, evacuating the chamber, and baking the walls and the sample using heaters described in section 3.1.2. At the end of the day, heaters were turned off, while the vacuum pumps were left running through the night.

On the day of a solar experiment, the experiment had to be transported from the lab to the outside, which required closing the valves to keep the chamber evacuated, shutting off the turbo pump(s), and partially disassembling the setup for transport. The setup was then reassembled and turned on outside. The lens was focused by adding a partial shade over the lens to reduce the power and moving the lens vertically until the spot on the sample was at its smallest, which was estimated only by visual inspection. This introduces an inevitable error estimated by calculation using the lens data. Most focusing distances were adjusted at most for ± 3 mm which results in an estimated spot diameter change uncertainty of up to 5.5 % or a 11 % change of spot area. An explanation of this calculation is given in section 5.2.1.

An exposure could be started once the chamber pressure was below at least 10^{-5} mbar, ideally below 10^{-6} mbar. It started by manually removing the shade above the lens and ended by manually placing the shade back above the lens when the desired exposure time was reached. After the exposure, the chamber was pumped down to at least 10^{-5} mbar another exposure could be performed by focusing the beam on a region of fresh regolith inside the crucible. If solar conditions permitted, multiple exposures could be done during a single experiment day using a single bulk regolith sample under vacuum.

3.3 Experimental results and analysis

The results presented here are divided into two main sections: the measurements obtained directly on the experimental setup and an EDX analysis of selected samples. Presented are 12 solar exposures from 4 experiments between the 23rd and 28th of April 2022. Solar exposures and the experiment conditions are listed in Tab. 3.1, Tab. 3.2, and Tab. 3.3. The melt samples are identified with the corresponding exposure number.

Table 3.1 Solar conditions at the time of each solar exposure: solar elevation angle at the time of the solar exposure α_{sun} [64] and measured solar direct normal irradiance (DNI) E_s

Exposure	Date	α_{sun} [°]	E_s [W m^{-2}]
1	23/03/2022	36.8	960
2	23/03/2022	37.5	900
3	25/03/2022	38.0	965
4	25/03/2022	40.7	958
5	25/03/2022	40.6	995
6	25/03/2022	36.8	920
7	25/03/2022	30.7	860
8	20/04/2022	43.1	1008
9	20/04/2022	48.4	1020
10	20/04/2022	50.6	1030
11	20/04/2022	45.5	955
12	28/04/2022	46.2	950

Table 3.2 Effective solar flux in the pyrolysis setup for each solar exposure: solar irradiation at the lens aperture E_{lens}, effective sunlight collection area at the lens A_{eff}, solar flux at the lens aperture Φ_{lens}, estimated incoming solar flux at the regolith surface Φ_{reg}, and an estimation of lower $\Phi_{abs,low}$ and upper bounds $\Phi_{abs,hi}$ for absorbed solar flux.

Exposure	E_{lens} [W m^{-2}]	A_{eff}[m^2]	Φ_{lens} [W]	Φ_{reg} [W]	$\Phi_{abs,low}$ [W]	$\Phi_{abs,hi}$ [W]
1	818	0.1143	93.4	74.0	29.3	44.0
2	768	0.1121	86.1	68.1	26.9	40.5
3	830	0.1107	91.8	72.7	28.7	43.2
4	813	0.1022	83.0	65.7	26.0	39.1
5	838	0.1025	85.9	68.0	26.9	40.4
6	783	0.1144	89.5	70.9	28.0	42.2
7	753	0.1332	100.3	79.4	31.4	47.2
8	860	0.0943	81.1	64.2	25.4	38.2
9	868	0.0048	67.2	8.7	3.4	5.2
10	854	0.0706	60.3	47.7	18.9	28.4
11	797	0.0866	69.0	54.6	21.6	32.5
12	807	0.0845	68.2	54.0	21.4	32.1

Table 3.3 Pressure and mass data for each solar exposure on the pyrolysis setup: Exposure duration, the mass of melted regolith samples m, initial pressure conditions before the solar exposure p_{ini}, chamber pressure during the exposure p_c, and the corresponding setup version (1-Vacuum lock, 2-Direct connection, 3-Two pumps).

Exposure	Duration [hh:mm:ss]	m [g]	p_{ini} [mbar]	p_c [mbar]	Setup
1	00:02:20	0.39	7.0×10^{-6}	2×10^{-1} to 7×10^{-1}	1
2	00:05:00	0.82	7.0×10^{-6}	3×10^{-1} to 1.2	1
3	00:00:30	0.10	1.2×10^{-7}	2×10^{-2} to 3×10^{-2}	2
4	00:00:15	0.00	2.6×10^{-6}	2×10^{-2} to 3×10^{-2}	2
5	00:00:45	0.20	2.7×10^{-6}	2×10^{-2} to 3×10^{-2}	2
6	00:02:30	0.39	3.3×10^{-6}	2×10^{-2} to 3×10^{-2}	2
7	00:00:30	0.17	6.4×10^{-6}	2×10^{-2} to 3×10^{-2}	2
8	00:00:30	0.09	1.1×10^{-7}	2×10^{-3} to 4×10^{-3}	3
9	00:38:00	0.00	1.0×10^{-6}	2×10^{-5} to 3×10^{-4}	3
10	00:31:00	1.03	1.5×10^{-6}	5×10^{-5} to 8×10^{-3}	3
11	00:10:00	0.66	5.0×10^{-7}	2×10^{-4} to 2×10^{-2}	3
12	03:12:00	2.32	6.0×10^{-8}	8×10^{-7} to 10^{-2}	3

3.3.1 Pressure and temperature measurements

Measurements obtained during and after the solar exposures on the experimental setup and in the lab include molten sample mass, solar irradiance, estimated irradiance of the regolith sample, and the sample's peak measured surface temperature.

The first 5 s to 15 s of each exposure exhibit an initially lower temperature than the rest of the exposure time, as shown in 3.9. During this time, a temperature plateau is reached where temperature stays relatively constant between 1500 K and 1550 K which is above but still close to the melting temperature of EAC-1A at 1444 K [25]. The bubble of melt characteristic for longer exposures does not form in this lower temperature region, as shown in 3.12b. A full bubble of melt (Fig. 3.12a) forms only after this period of 5 s to 15 s when the temperature rises higher to between 1600 K and 2100 K depending on the incoming flux density. This secondary increase in temperature can be seen in well in Fig 3.9b at around 15 s and in Fig. 3.9c at around 20 s. The photos of other solidified melt samples ar shown in Fig. 3.12.

Another phenomenon can be observed during the first 15 s. Several particles get continuously ejected from the hotspot, as shown in the image from the thermal camera in 3.13. The particles are the several hot points above the hotspot. Due to their measured temperature, these ejecta are likely partially or fully melted. After this first period, particles keep getting ejected in considerably smaller quantities. This likely happens when the hotspot falls on fresh regolith or when regolith falls into the existing melt. After the experiments, these ejected particles can be seen sticking to the wall of the crucible.

Chamber pressures during a solar exposure reach similar values for each of the three setups as shown in 3.3. The first two samples melted in the first version of the setup, reaching between 0.2 mbar and 1.7 mbar. The exposures in the second setup reach between 2×10^{-2} mbar and 3×10^{-2} mbar with a slight tendency to decrease over time. The rest of the exposures reach even lower pressures between 8×10^{-7} mbar and 10^{-2} mbar. The relatively high highest pressure of sample 12 at 10^{-2} mbar is reached only at three pressure peaks during more than a 3 h exposure. Most of the time, the chamber pressure stayed bellow 2×10^{-3} mbar except for the mentioned peaks. All these pressures can be seen in Fig. 3.9, 3.10 and 3.11, with the exception of samples 1 and 2. These have not been continuously logged but have been logged manually. Therefore, no plot of their pressure or temperature is shown.

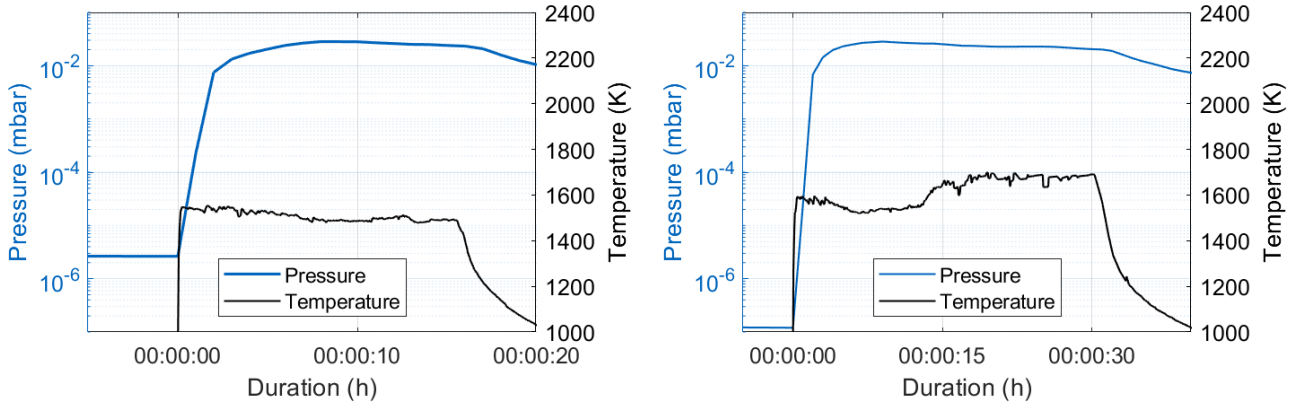

(a) A 15 s exposure of sample 4

(b) A 30 s exposure of sample 3

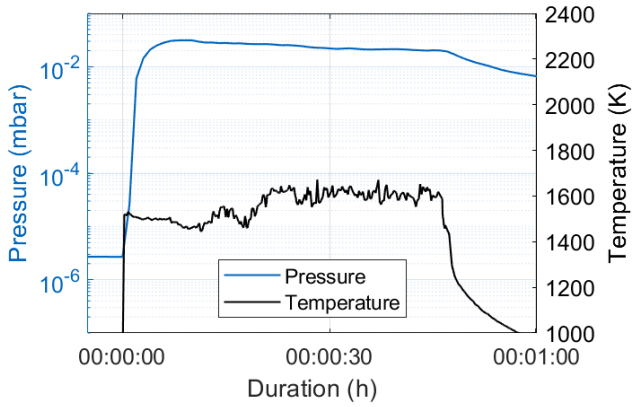

(c) A 45 s exposure of sample 5

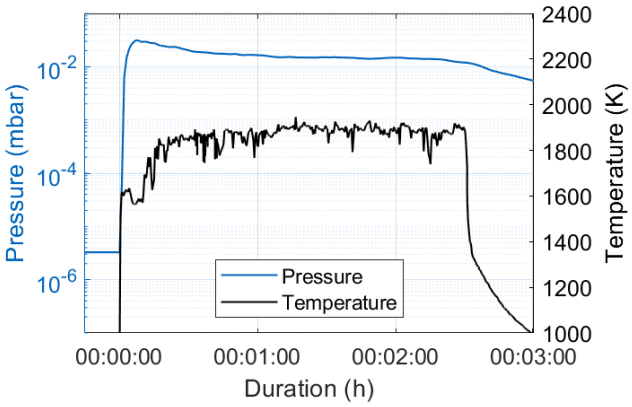

(d) A 150 s exposure of sample 6

Figure 3.9 Pressure and temperature of exposures ranging from 15 s to 150 s, producing samples 3-6.

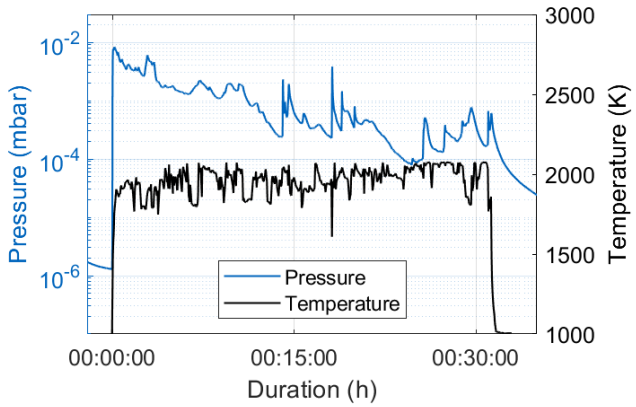

(a) A 30 min exposure of sample 10

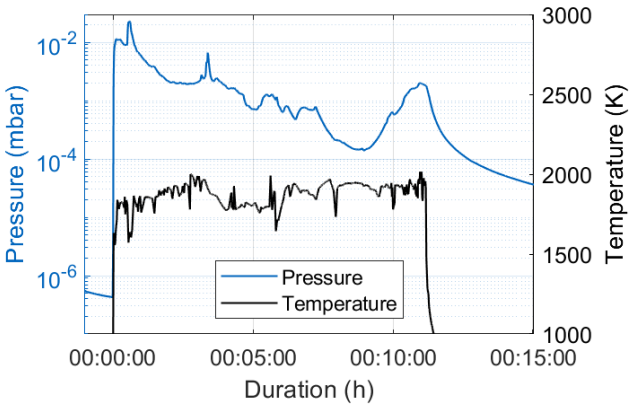

(b) A 10 min exposure of sample 11

Figure 3.10 Pressure and temperature plots of the longer exposures 10 min and 30 min, producing samples 10 and 11.

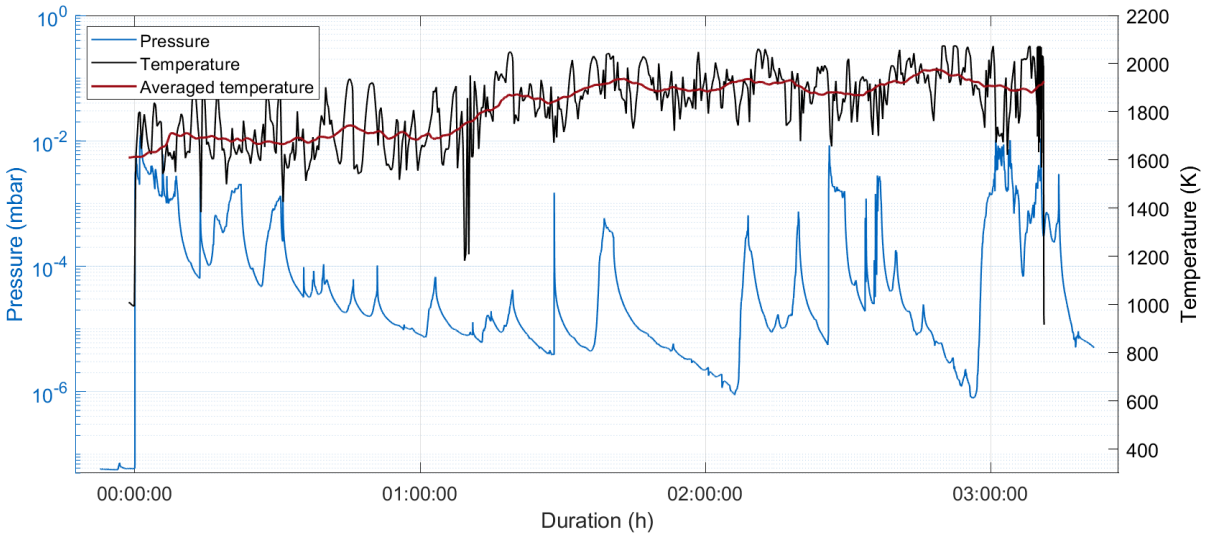

Figure 3.11 A pressure, temperature and a 15-minute-averaged temperature plot of a 3 h exposure, producing sample 12.

(a) Sample 3, 30s

(b) Sample 4, 15s

Figure 3.12 Photos of melted samples. The estimated concentrated solar spot with a gaussian solar flux distribution has an approximate diameter of $2\sigma = 6.9$ mm

An informative sample regarding pressure evolution is the number 9. This sample was exposed to only 1/16th of the available power and therefore exhibits comparatively low pressures and temperatures between 1400 K and 1450 K. These are below the melting temperature, which results in partially sintered regolith without any melt. The pressure still rises significantly over the initial pressure, which can be attributed to a significant residual amount of adsorbed material in the regolith which outgasses during solar heating. This shows that most gaseous material in all exposures is likely only desorbed volatiles from the regolith sample, not vaporized regolith. This initial sudden outgassing is likely the cause of the aforementioned ejected particles during the early period of an exposure.

RGA measurements No significant results could be obtained by measurement of gas composition using the RGA. As shown in Fig. 3.9, 3.10, 3.11 and Tab. 3.3, all exposures resulted in peaks above the RGA measurement limit of 10^{-5} mbar. The operation of the vacuum lock in setup version 1 was a long process,

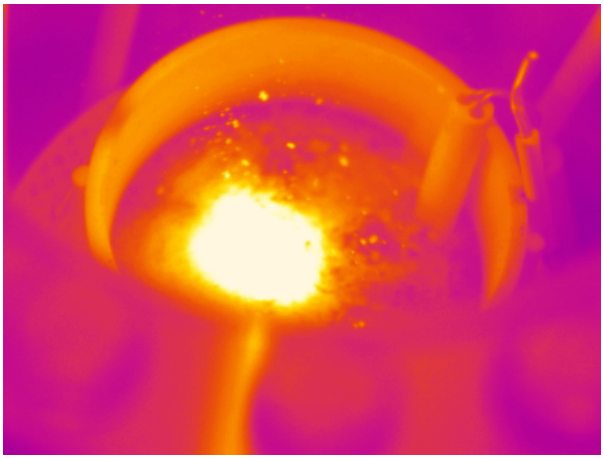

Figure 3.13 Ejected particles from the hotspot during the initial 15 s of a solar exposure visible on the IR camera image

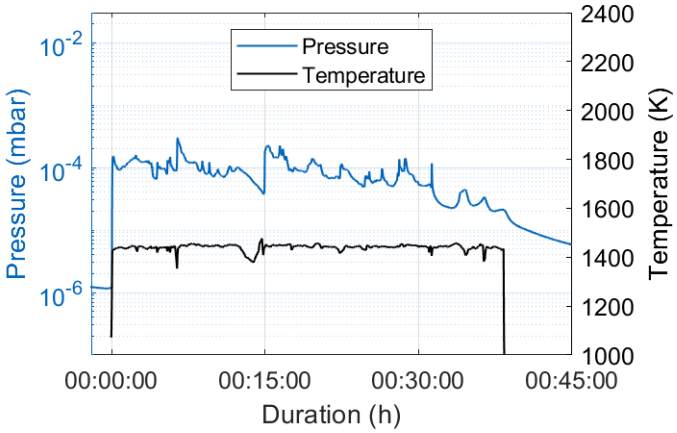

Figure 3.14 Pressure and temperature plot of sample 9

including the opening and closing of both valves and waiting for the pressure in the analysis section to fall below the RGA limit after the lock was operated. This time difference likely resulted in recondensation of any vapors to the lock volume or the analysis section surfaces before the RGA could be switched on. The setup version 3 had a similar problem of pressure fall-off. The duration between the initial pressure peak produced with sunlight exposure and the time when the V1 valve could be opened for analysis presents a problem in the RGA measurement because the different gasses produced are pumped out with the vacuum pump 2 as well as condense and adsorb on the surfaces in the chamber differently over time and temperature conditions. Due to these difficulties, no RGA results have been obtained during these experiments.

3.3.2 Elemental analysis of selected samples

A limited number of samples were selected for energy-dispersive x-ray spectrometry (EDX) analysis to analyze their elemental composition. The analysis was done at the Technical University of Munich on an FEI Philips XL 40 scanning electron microscope (SEM) with an Oxford instruments EDX detector and an IDFix-NumeriX processing system. Samples 10, 11, and 12 were selected based on their longer exposures and comparatively low pressures during the exposure. EDX spectra of the surface of these samples

were measured at a constant voltage of 20 kV, 500x magnification, and a 60 s measurement time. All spectra of melt samples were done as point measurements on the sample surface. The major difference in the measurement was with the reference bulk EAC-1A sample, whose spectrum was measured using a mapping method. This captured the average composition at the 500x magnification and not only a single grain of the bulk material. The melt samples were taken as produced, cleaned, and sputtered with Platinum. Due to the longer measurement time of the EAC-1A mapping and the instrument parameters, the measurements can only be taken as a qualitative indication of elements in the sample. The elemental data is therefore plotted in Fig. 3.19 with Silicon-normalized counts.

Silicon can be taken as the reference element because it has a peak in all melt and bulk regolith samples. Its peak is the highest in most samples and allows for a good comparison reference. It is also not expected to vaporize from the melt in significant amounts at the temperatures and pressures reached within the chamber during solar exposures. This is shown by comparison with thermochemical simulation in section 4 as well as literature [11, 15, 37]. Therefore, it is assumed that the amount of silicon stays the same between bulk material and the melted sample.

Reference sample EAC-1A from the same batch as the material for the solar exposures was taken as the reference for EDX measurements. A qualitative comparison of the melt samples against the EDX spectrum is shown in Fig. 3.15. The spectrum of EAC-1A shows significant amounts of silicon, oxygen, magnesium, aluminum, calcium, and iron at X-ray emission energies of 1.74 keV, 0.53 keV, 1.25 keV, 1.48 keV, 3.69 keV and 6.40 keV respectively. A prominent carbon peak can be seen at 0.27 keV and is attributed to the material of the carbon tape used as the base surface upon which the simulant was placed. Sodium and potassium peaks are present in smaller amounts at 1.04 keV and 3.31 keV respectively. Phosphorus peak at approximately 2.01 keV would be expected according to the composition of EAC-1A shown in 4.1. In this case, it overlaps with the M-shell platinum peak at 2.05 keV due to the platinum sputtering of the sample. Therefore, the presence of phosphorus cannot be accurately detected.

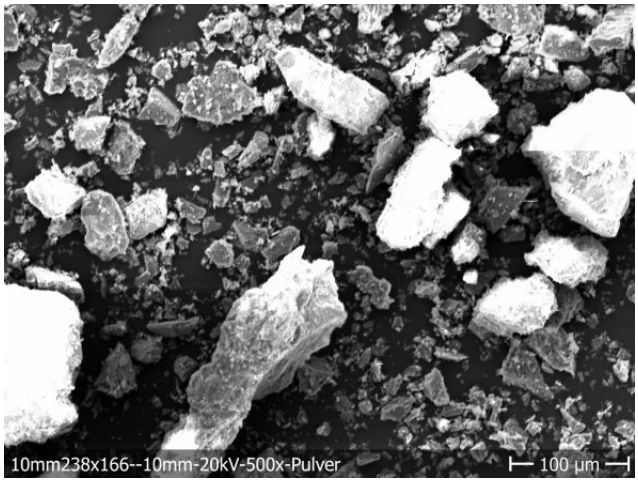

(a) SEM image

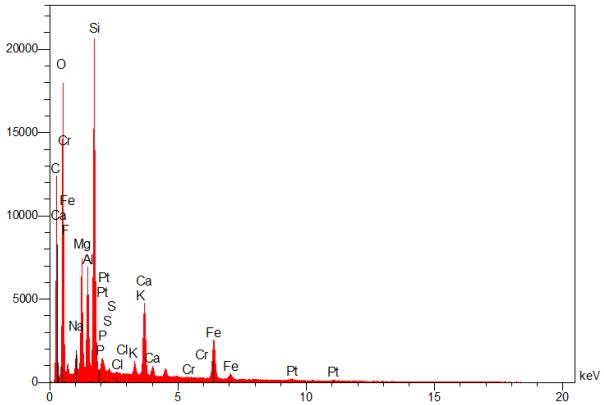

(b) EDX spectrum

Figure 3.15 SEM and EDX analysis of EAC-1A reference sample

Melt samples All EDX measurements of the melted samples were taken as point measurements. Relevant areas had to be chosen for each sample. The EDX spectra of all these points are shown in Fig. 3.19 except for point 1 on the condensation skin of sample 11 (Fig. 3.17c). This point shows significant amounts of iron and oxygen, which reach far above the silicon peak. Therefore, it could not be included

in the bar graphs in Fig. 3.19b not to skew the graph. Due to the large presence of iron and oxygen, it is assumed this point was located on a particle with high iron oxide content. It does not give useful information for this analysis as it shows only one distinct particle. The EDX spectrum of this point is shown in the supplementary figure A.1.

Other measurement points can be compared qualitatively to each other and the EAC-1A reference. Firstly, it can be observed that all of the samples with exposure times above around 60 s have two distinct regions on their surface. A photograph and SEM images with measurement points are shown for all 3 analyzed melt samples in Fig. 3.16, 3.17 and 3.18. A sample with an exposure time of 30 s and no distinct regions on the surface is shown in Fig. 3.12a. The surface of sample 10 in Fig. 3.16a and 3.16b shows these 2 distinct regions well. It appears to be smoother and more glassy on the left and rougher on the right. The smooth surface is located at the location of the material which was melted last, and the rough surface is located on the older melt. Therefore it is assumed that the rough surface is the condensation skin on the solidified melt, whereas the smooth surface does not have the skin due to its later solidification. Due to the homogeneity of the smooth melt region, only 1-2 measurement points have been chosen here in comparison to 2-3 points on the skin, which is much more varied.

Magnified images of the skin in Fig. 3.16d, 3.17c and 3.18c all indicate a condensate that lies on the surface of the melt. The melt below the condensation still appears to reach through the skin at several positions, for example at point 3 in Fig. 3.17c likely lies on a bubble of melt. The EDX measurements of the skin surface in Fig. 3.19b also indicate a varied composition of the skin surface with significant increases in magnesium content in samples 11 (point 2) and 12 (points 1 and 2) as compared to the EAC-1A reference. The amounts of other elements also vary between the samples, which could point to different condensates on the surface or spatial variation of the melt composition. The EDX measurements of the smoother region show much less variation of most elements, with oxygen being an exception. This could indicate that the melt surface is mostly homogenous and that the variation of the elemental composition of the skin comes from the various condensates on the surface.

Elemental measurements The main focus of this thesis is the production of oxygen, which exhibits interesting behavior in EDX measurements of both the melt and skin regions. Fig. 3.19a shows the melt regions of all chosen samples. It shows no significant difference in any of the major elements except for oxygen which shows a decrease in amount for all samples relative to the reference EAC-1A. This would indicate that the surface of the samples most likely has a lower oxygen content, while the amounts of other elements stay mostly similar. This is consistent with EDX measurements by Cardiff et al. [38], which measured molten samples produced in the setup by Matchett [14].

An independent decrease in oxygen relative to other elements would mean that only oxygen vaporizes out of the melt while other reduction products stay or recondense in the melt. The presence of a condensation skin and condensate on the crucible, described in the following paragraphs, indicate that this could be only partially true. They show reduction products that left the melt and recondensed somewhere else. This should result in a decrease of oxygen as well as the corresponding element, which builds the oxide that vaporizes under given conditions. This change in the measured amount might be present, but it is not visible due to the much lower initial peaks of other elements or the normalization with the silicon peak.

A similar result is shown in EDX measurements of the condensation skin in Fig. 3.19b. The oxygen content seems lower than in bulk EAC-1A, but the decrease is not as significant as in the melt region. These measurements also show significantly more variation in other elements, primarily in magnesium, as well as aluminum, calcium, and iron.

Drawing other qualitative conclusions from these EDX measurements of the condensation skin is not possible. Firstly, the thickness of the condensate and the EDX depth penetration are unknown. This means the composition of the condensate is not known independently from the melt, as it might be that

(a) Sample 10

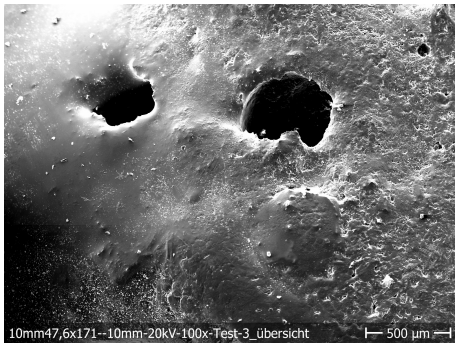

(b) Overview of the sample at 100x magnification

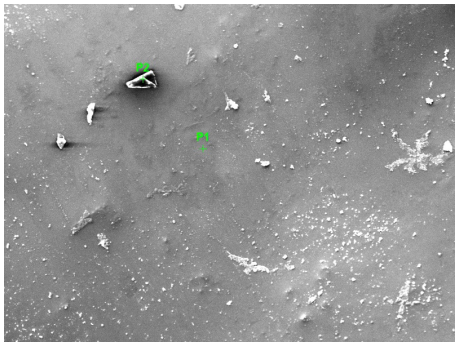

(c) An SEM image of the melt at 500x magnification

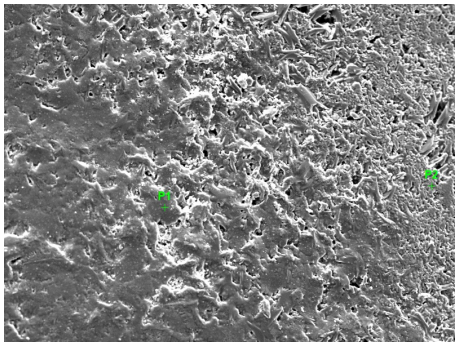

(d) An SEM image of the skin at 500x magnification

Figure 3.16 Sample 10: (a) An image of sample 10 in the crucible after the exposure, SEM images of (b) the sample overview with visible melt and condensation skin, (c) the melt region with marked EDX measurement points, and (d) the skin region with marked EDX measurement points

the skin measurements also include a significant amount of the melt composition below the condensate. Secondly, the amount of magnesium in the skins of samples 11 and 12 could indicate a relatively high temperature at which both MgO and SiO_2 already vaporize. This could mean that the normalization with the silicon peaks might not be entirely valid due to the vaporization of SiO_2 out of the melt. If this is the case, the normalized values overestimate the amounts of all elements compared to EAC-1A. Lastly, the magnesium could be explained by locally rich regions of magnesium or magnesium oxide particles on the surface instead of magnesium condensate. These particles could be present on top of the already solidified melt and the skin because of ejected particles described in section 3.3 and shown in Fig. 3.13. Due to these uncertainties, it can be concluded that there is an indication of lower oxygen content at the surface of the samples. However, no conclusions about the composition of the melt below the surface can be made.

(a) Sample 11

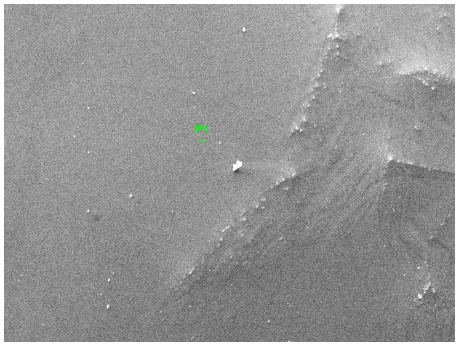

(b) An SEM image of the melt at 500x magnification

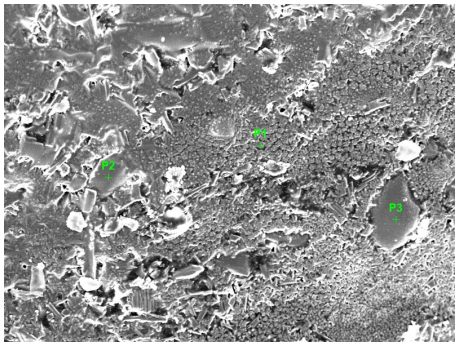

(c) An SEM image of the skin at 500x magnification

Figure 3.17 Sample 11: (a) an image of the sample in the crucible after the exposure, SEM images of (b) the melt region with marked EDX measurement points, and (c) the skin region with marked EDX measurement points

(a) Sample 12

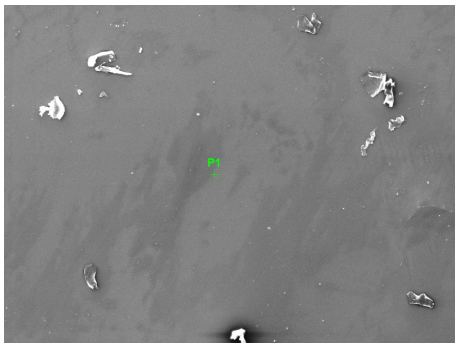

(b) An SEM image of the melt at 500x magnification

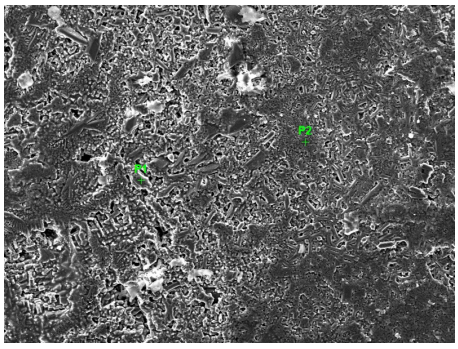

(c) An SEM image of the skin at 500x magnification

Figure 3.18 Sample 12: (a) an image of the sample in the crucible after the exposure, SEM images of (b) the melt region with marked EDX measurement points, and (c) the skin region with marked EDX measurement points

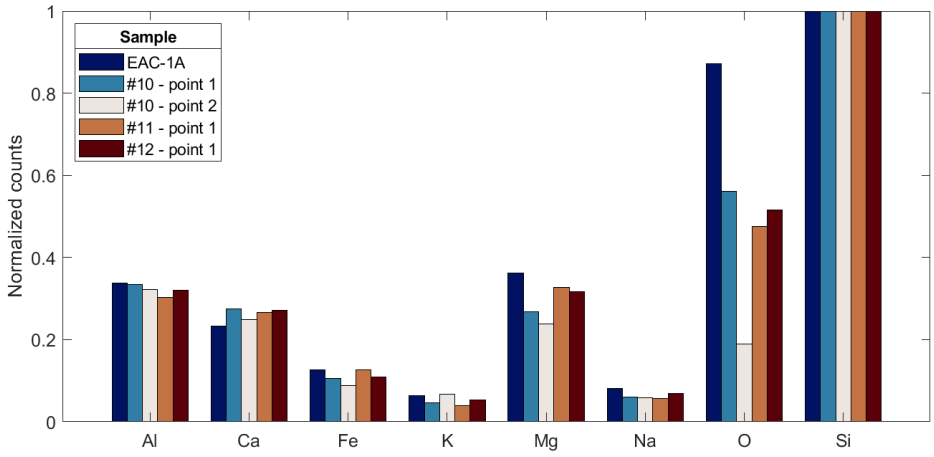

(a) Melt spectrum

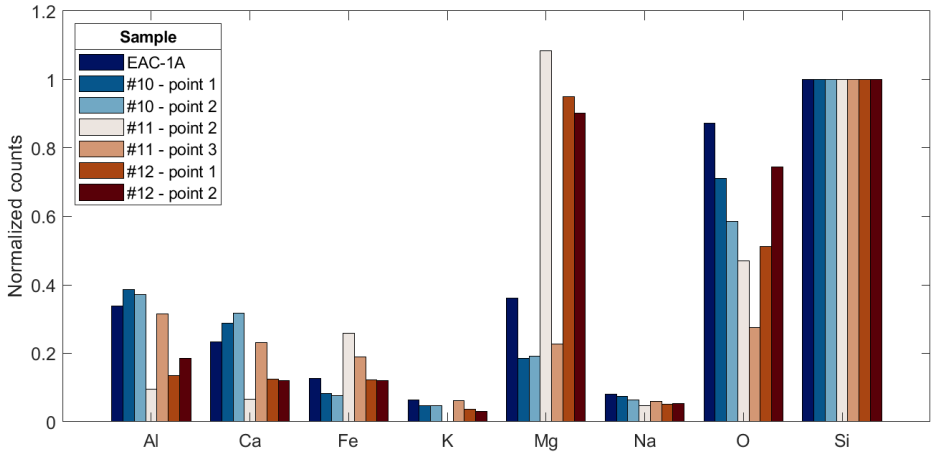

(b) Skin spectrum

Figure 3.19 EDX measurements of melt and skin regions of selected samples with Silicon-normalized counts and the EAC-1A as reference material

Condensate Another two samples of the crucible wall were analyzed, where two distinct regions of condensate material were found after the exposure of sample 12 (Fig. 3.18). The crucible with marked condensate regions and their corresponding spectra are shown in Fig. 3.20. The darker condensate marked with "A" seems to have been deposited first, and the lighter condensate marked with "B" is deposited on top. This is also consistent with the EDX measurements, which show an aluminum peak in the "A" condensate and not in "B". This aluminum is not expected to have come from the sample through vaporization and condensation. It is assumed that this is the crucible material being measured through the thin layer of the darker condensate since the crucible used is made from pure alumina ceramic and therefore contains only aluminum and oxygen.

Apart from aluminum and oxygen, there are two visible peaks of sodium and potassium in both areas, with a higher sodium content in the lighter condensate relative to the potassium peak. These two elements are also expected to vaporize first from the regolith as well as easily condense on relatively cold surfaces on the crucible as modelled in section 4 and literature by Matchett [14], or Cardiff [65]. A significant loss of sodium and potassium oxides from a JSC-1A melt during solar exposures with similar conditions in vacuum has also been measured by Sauerborn [44]. Condensation of Na and K on the crucible surface

indicated dissociation of Na_2O and K_2O which are the first oxides expected to vaporize and dissociate from the melt. The presence of elemental Na and K on the crucible, therefore, shows the occurrence of pyrolysis reactions in the chamber.

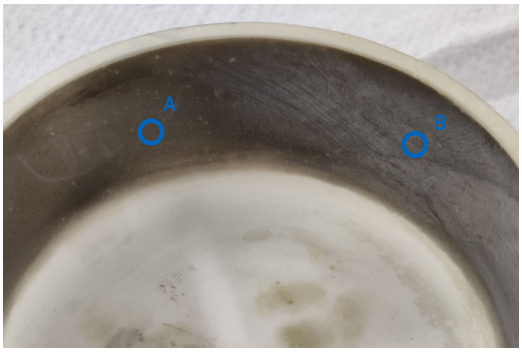

(a) Crucible wall

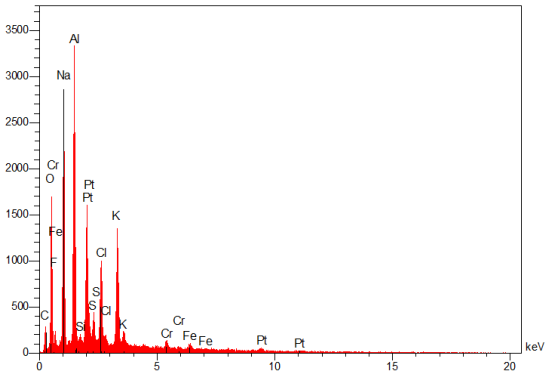

(b) An SEM image of the melt at 500x magnification

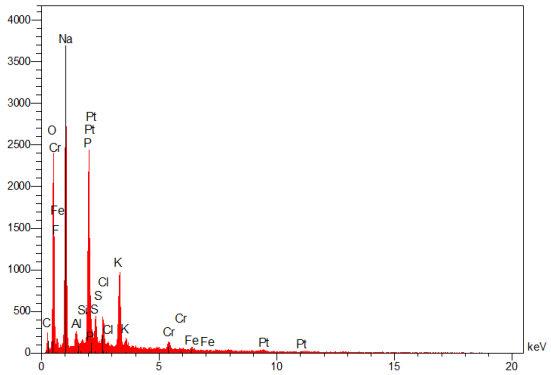

(c) An SEM image of the skin at 500x magnification

Figure 3.20 Crucible condensate EDX analysis: (a) an image of the crucible wall with marked condensates, (b) EDX spectrum of condensate A, and (c) EDX spectrum of condensate B.

3.4 Conclusion of the experimental work

The primary issue of the experimental results is the insufficient baking of bulk regolith in the vacuum chamber and the resulting outgassing of the sample during heating. This results in a significant pressure increase due to outgassing and, in turn, the inability to analyze vaporized material through the pressure increase alone since the actual vaporization product represents an undetermined amount of gaseous material in the chamber. On the other hand, the approximate pressure equilibria could be inferred from the pressure range, surface temperature, and the pumping rate in the case of an open system. Pressure and temperature results confirm the presence of theoretical conditions needed for vapor pyrolysis to occur when comparing these values to the data shown in section 4 as well as in literature by Matchett [14] or Cardiff [65].

EDX analysis of the melt samples has shown a decrease in oxygen content of the sample surface compared to the bulk regolith simulant, consistent with observed decrease in surface oxygen by Cardiff [38]. A conclusion about other elements cannot be confidently drawn at this point. The validity of the comparison between EAC-1A and melt measurements due to non-polished surface measurements makes these results less certain, so they have to be interpreted with caution. However, it can be taken as an initial indication of a pyrolysis process. The confidence in the occurrence of a pyrolysis process is increased by

the condensate on the crucible walls, which clearly shows the expected elements potassium and sodium in the EDX measurement. It can be concluded that solar-vapor pyrolysis was achieved in these experiments, but a specific conclusion about oxygen production cannot be drawn.

4 Thermochemical equilibrium modelling of vapor phase pyrolysis

This chapter presents the modelling of the thermodynamic behavior of four representative regolith compositions to calculate thermodynamic properties, amounts of produced oxygen, and other species during thermal reduction. The calculation of chemical equilibria at selected discrete constant pressure and temperature conditions was performed using the Gibbs Free Energy minimization concept with the FactSage 8.1 software package [66, 67, 68].

The reaction kinetics of the process have not been considered in the presented calculations. They are considerably slow, as discussed by Senior [11] and Shaw [15]. The process with slow kinetics likely would not reach equilibrium in a technically sensible timespan, so the presented thermochemical results should be understood as results of an idealized state where the reaction is allowed time to reach equilibrium. An additional assumption is a homogenous mixture of oxides at macroscopic and microscopic levels. This leads to reactions that would not happen in actual regolith, with particles of a specific mineral composition representing a locally non-homogenous material. An estimation of a realistic oxygen yield will be discussed in section 4.3.6.

The following simplifying assumptions have been made for these calculations:

- The system is assumed to be at chemical equilibrium. All reactions with slow reaction kinetics have been completed.
- Material composition is homogenous and has no local differences. All compounds, atoms, or molecules can interact with each other and achieve the lowest possible energy state.
- The regolith sample does not contain any volatile material which would outgas at modelled temperatures or change the thermal or chemical behavior of the sample.

4.1 Regolith compositions

Thermochemical simulations have been run with three regolith and one regolith simulant composition. These have been chosen in a way to cover the most typical compositions of lunar regolith. The regolith compositions chosen are the Luna sample 24999, the Apollo sample 64501, and the Apollo sample 70051. Samples 24999 and 64501 are, according to Papike [20], "pure" representations of a Maria and a Highland regolith composition, respectively. These have been taken to determine the behavior of representative Maria and Highland soils. These two samples have also been used in the previous thermochemical simulations by Shaw [69] and can be used to compare the two simulations.

The Apollo sample 70051 [70] has been chosen as an additional regolith sample with high titanium content to compare its behavior with the low-titanium Maria sample 24999. It might exhibit different behavior due to the higher fraction of TiO_2 and, therefore, higher Ilmenite content. It is not the highest titanium-content sample but is an overall interesting sample for ISRU investigations as proposed by Hill et al. [70] because it is a mixture of soils across a large area of the Apollo 17 landing site. The last modelled composition is the EAC-1A simulant [24, 25], also used in the experiments in Section 3.

Table 4.1 Regolith and regolith simulant geochemical compositions in wt% used for thermochemical simulations. Oxide fractions are taken from [20] for 24999 and 64501, [70] for 70051, and [25] for EAC-1A

Oxide	24999, Maria	64501, Highlands	70051, High-Ti Maria	EAC-1
SiO_2	44.61	45.42	43.22	44.41
FeO	20.83	4.49	12.70	0.00
MgO	10.97	4.39	10.55	12.09
CaO	10.87	16.77	11.78	10.98
Al_2O_3	10.77	27.85	16.08	12.80
TiO_2	0.99	0.45	5.21	2.44
Cr_2O_3	0.42	0.08	0.00	0.00
MnO	0.28	0.06	0.15	0.20
Na_2O	0.23	0.40	0.25	2.95
K_2O	0.02	0.09	0.07	1.32
Fe_2O_3	0.00	0.00	0.00	12.20
P_2O_5	0.00	0.00	0.00	0.61
Total	99.99	100.00	100.01	100.00

4.2 Modelling method and theory

Computation of thermochemical equilibria in FactSage relies on databases of optimized and verified multi-component systems. All single oxides used in the calculations are contained in these databases, but not all possible multi-component systems have been fully verified through experimental data. [66]

4.2.1 Input, solution, and background data in FactSage

The important $Al_2O_3-CaO-FeO-Fe_2O_3-MgO-SiO_2$ system, which contains most prominent oxides for this study, has been fully verified with experimental data from 25 °C to above liquidus temperatures [67]. This system contains 98.05% of all Maria oxides, 98.98% of Highland oxides, 94.33% of High-Ti Mare oxides, and 92.48% of EAC-1A oxides by weight. The four compositions also include several other oxides, not included in this multi-component system. There are in total 9-10 oxides per regolith composition, so they cannot be described by a single optimized multi-component system. The above mentioned $Al_2O_3-CaO-FeO-Fe_2O_3-MgO-SiO_2$ system contains only six relevant oxides. There are no systems which contain all oxides contained in the modelled regolith compositions. To calculate a system with more reactants, FactSage combines data from several multi-component systems. For example, an additional system $Al_2O_3-CaO-CrO-Cr_2O_3-SiO_2$ can be used for calculation to include Cr oxides.

The EAC-1A is a problematic composition in that regard. Slags containing Fe_2O_3 and Ti simultaneously have not been evaluated in the FactSage underlying data. [66] Therefore, the equilibrium results for EAC-1A have to be interpreted with caution.

Input reactants in FactSage are selected from compound databases and the computation is done using solution databases. Correct compound databases and solutions must be selected based on reactants and expected products. To ensure thermodynamically consistent data, reactant compounds have been selected from the compound database which correspond to the chosen solution database. Choosing the corresponding coupled compound database assures consistency because both compound and solution data were obtained by simultaneous evaluation/optimization. The FToxide database was used in the following calculations for reactant compounds and solutions since it is a specialized database for metal oxides in solid and liquid states. Additionally, the FactPS database was included since it is the largest general database and includes a large amount of gas data that is not given in other databases. [66]

4.2.2 Discretization study of equilibrium grid-points

The results given by FactSage are discrete equilibrium points on a grid of pressures from 10^{-8} mbar to 10^{3} mbar and temperatures from 298 K to 3773 K. Upper and lower pressure bounds have been chosen between Earth's atmospheric pressure of 10^{3} mbar and 10^{-8} mbar which is one order of magnitude less than the proposed pressure of 10^{-7} mbar for lunar operations of a vapor-phase pyrolysis reactor by Cardiff [38]. This covers the most likely areas of interest for investigating pyrolysis behavior in vaporization and sublimation ranges, as well as the lowest initial pressures of 6×10^{-8} mbar reached during experiments in section 3.

Large discretization steps between these grid points can lead to missing spikes in certain values between two points. This is especially important for heat capacity data, which will partially be used in further thermal modelling of the regolith surface in Section 5.2 and exhibits considerable peaks at certain temperatures due to phase change phenomena. Discretization has a lesser impact on enthalpy, gas evolution, and O_2 yield, although it still has to be investigated to verify the computation step size. A small discretization study with a Maria regolith composition (Fig. 4.1) was run to analyze the effects of temperature and pressure step size and make a trade-off between resolution and computation time. The temperature discretization study was run at a pressure of 10^{-5} bar for temperature steps between 10 K and 50 K while the pressure study has been run at a temperature of 1773 K and resolution between 10 and 1 steps per decade. The constant values of 10^{-5} mbar and 1773 K have been chosen to provide a view over the whole range of the vaporization/sublimation process, shown between 1450 K and 1900 K and 10^{-7} mbar and 10^{-3} mbar.

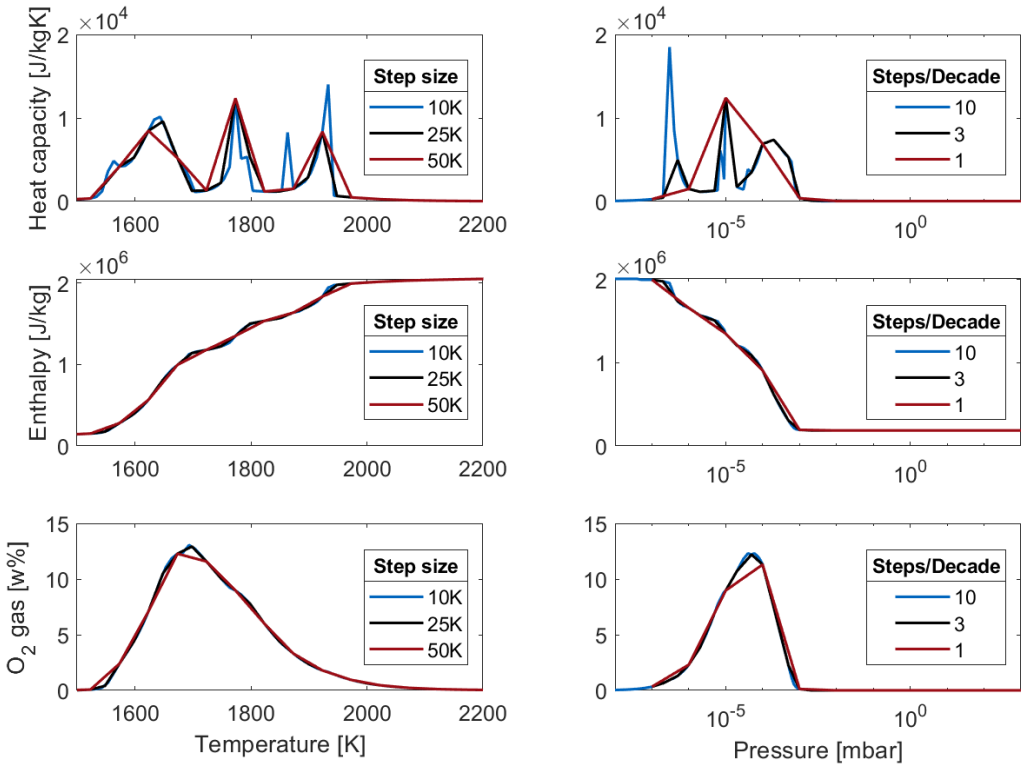

Figure 4.1 Results of the temperature (left) and pressure (right) discretization study in FACTsage with heat capacity (top), enthalpy (middle), and O_2 gas production as the weight fraction of initial regolith mass (bottom). Temperature discretization values are shown for a constant pressure of 10^{-5} mbar and pressure values for a constant temperature of 1773 K

Sharp spikes are visible in the heat capacity figure at 10 K or 10 steps/decade, which start disappearing at lower resolution. Enthalpy and oxygen production values are less impacted by the increase in step size even at a step of 50 K or 1 step/decade, although a noticeable reduction in quality can be seen especially in the O_2 figure at the peak around 1700 K or 10^{-4} mbar. Heat capacity data is shown to be the more impacted by the coarser resolution in comparison to enthalpy and O_2 values. A trade-off was made with discretizations of 20 K for temperature and 3 steps/decade for pressure to keep computation time low while having enough resolution in both temperature and pressure to trace the finer details of the enthalpy and O_2 production during the phase transition. The sharp peaks in heat capacity are not as relevant for this study because only the heat capacity data outside the vaporization/sublimation (1450 K and 1900 K at 10^{-5} mbar) region will be used for thermal modelling in Section 5.2 while the phase transition data will be taken from the more steady enthalpy values.

4.3 Thermochemical modelling results

Thermochemical calculations provide data on numerous solid, liquid, and gas compounds that exist at chosen equilibrium points. This thesis focuses primarily on oxygen production and its connection to a thermal model. Thermodynamic data and produced oxygen gas are the primary datasets that will be evaluated. This section presents the data produced in FactSage computations of the Maria regolith composition. Other three regolith compositions have also been computed. Their main results will be compared to the Maria composition in section 4.3.4. All other figures for the remaining regolith compositions, not shown in this chapter, are shown in the Appendix.

4.3.1 Regolith phases

To discuss regions of interest in the thermochemical data, it is useful to look at the figures of solid, liquid and gas fractions (Fig. 4.2) and compare them to a contour plot of system enthalpy (Fig. 4.3), using values from FactSage solutions. The solid phase exists for the whole pressure range below 1350 K except for pressures bellow 10^{-5} mbar, where vaporization or sublimation start below 1300 K. Above this pressure, a melting phase transition can be observed between 1350 K and 1530 K. The liquid state (Fig. 4.2 (middle)) can then be observed until the large pressure-dependent increase in enthalpy (Fig. 4.3). For example, the enthalpy increase is seen at approximately 1800 K for the pressure of 10^{-3} mbar and at 2100 K at a pressure of 10^{-1} mbar. This increase in enthalpy denotes the vaporization/sublimation of liquid material and corresponding gas phase production, which can be seen in Fig. 4.2 (right). The vaporization/sublimation temperature decreases with the decrease in pressure until the vaporization regime crosses the melting temperature between 1500 K and 1400 K. At that point, the sublimation of solid material directly to gas can be observed due to the lack of a liquid phase between solid and gaseous phase ratios. Vaporization/sublimation is used in the following chapters when referring to vaporization or sublimation and properties or behavior which is seen in both regimes. Above the vaporization/sublimation temperature range, only the gas phase can still be observed in Fig. 4.2 (right). Another increase in enthalpy can be seen between 10^{-8} mbar and 10^{-3} mbar, above 2250 K and 3000 K respectively. This increase is associated with the dissociation of SiO, which is discussed later in Section 4.3.3.

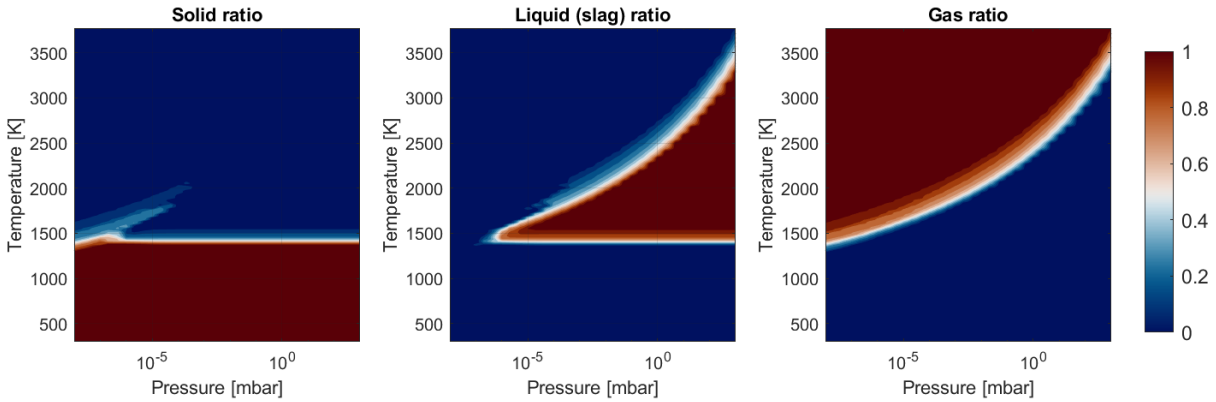

Figure 4.2 Maria regolith: Solid, liquid, and gas phase mass-ratios for pressures 10^{-8} mbar to 10^{3} mbar and temperatures 298 K to 3773 K.

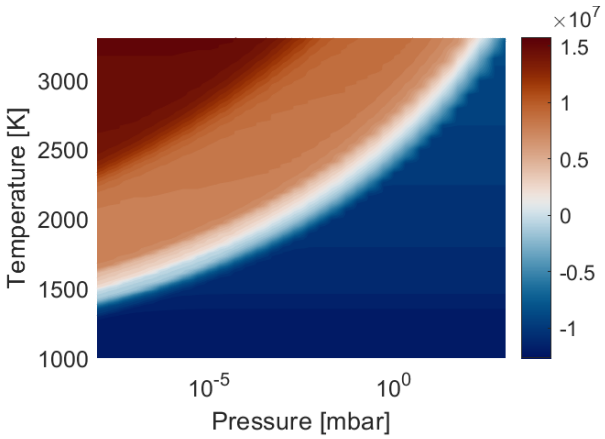

Figure 4.3 Enthalpy for Maria regolith composition 24999 for pressures 10^{-8} mbar to 10^{3} mbar and temperatures 298 K to 3773 K.

4.3.2 Thermodynamic values

FactSage calculations are based on the underlying thermodynamic data, namely enthalpies and heat capacities of reactants. Equilibrium solutions also give their corresponding thermodynamic states with values for enthalpy and heat capacity. These are later used in the thermal model in section 5.2 for the modelling of heating, vaporization/sublimation and the reaction enthalpies. The validity of this data is discussed and compared to values from literature in the following.

Heat capacity Heat capacity of lunar regolith has been measured only limited temperature ranges [28] and has to be extrapolated in the ranges of interest for pyrolysis, that lay above the melting point (>1500 K). Heat capacity of Apollo regolith samples was only measured below 350 K [26]. Models from literature fit these and other datasets of terrestrial material in different ways. A comparison heat capacities form FactSage results and two major heat capacity models from Schreiner et al. [28] and Colozza [48] is shown in Fig. 4.4 to discuss the validity of using FactSage heat capacity data. The model by Schreiner et al. [28] is considered most accurate because it is a fit of Apollo bulk regolith and molten regolith heat capacity measurements [31]. This heat capacity data can only be compared solid and liquid phase regions and not for the temperatures where regolith compounds begin to vaporize or sublimate, as there is no literature model for regolith vapor.

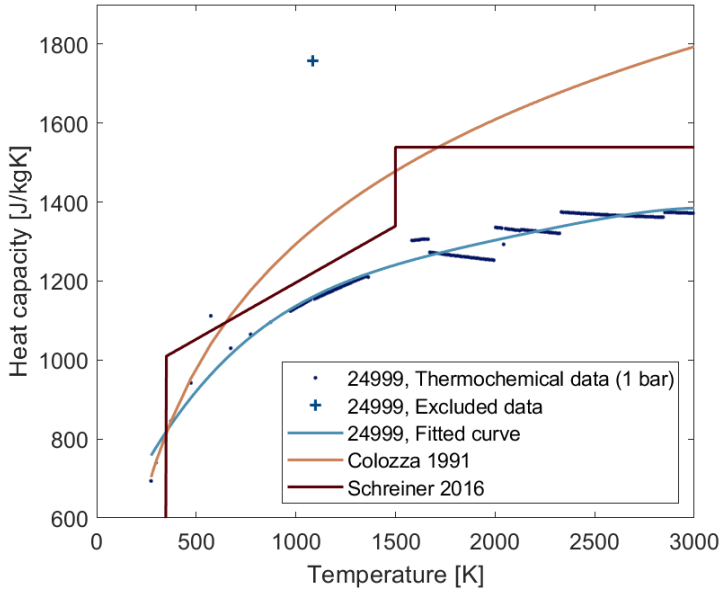

Figure 4.4 Comparison of FactSage heat capacity data for Maria regolith composition 24999 at 1 bar excluding the phase transitions with models from Colozza [48] and Schreiner et al. [28].

Heat capacity of the Maria composition at 1 bar is used in Fig. 4.4 to compare the resulting heat capacities fro mFactSage with models from literature. All phase transitions, melting, vaporization, and sublimation, have been excluded from the data to plot and fit a base heat capacity function. This function does not account for the apparent heat capacity increases during melting or vaporization, so that it can be compared to the literature models, which are based on experimental data, to study their behavior and differences. The fitted data follows a similar upwards polynomial trend as the two models, but the values below both other models for the majority of the temperature range. The Schreiner et al. model, which lays significantly closer to the thermochemical data, is based on more experimental data and is therefore assumed to be a more accurate model than the one from Colozza.

Nonetheless, values from the thermochemical model are still lower than the Schreiner et al. model. These lower values can be attributed to the underlying data stemming from equilibrium calculations, which minimize the Gibbs free energy to the lowest energy state. This is an idealized state which can, in theory, only be reached after a long reaction time and is not entirely representative of an actual heating experiment.

Specific heat capacities of all calculated compositions have also been analyzed, and polynomial functions have been fitted to their data (Fig. 4.5) for further use in the thermal model in Section 5.2. The fitted functions are mathematical approximations of the heat capacity data points, not physics-based models. Comparison plots showing heat capacity data, fitted functions, and literature models for all compositions are shown in the supplementary figure B.2. The fitted function for all compositions follow Eq. 4.1, with C_1 to C_5 being their coefficients and R^2 the error of each fit, listed in Tab. 4.2. EAC-1A has not been fitted due to the complexity of the heat capacity data, which would require a step-wise fit of 2 polynomial functions. The supplementary Fig. B.2d shows its data and an approximate fit.

$$C_{p,base}(T) = C_1 T^4 + C_2 T^3 + C_3 T^2 + C_4 T + C_5 \tag{4.1}$$

All computed heat capacity values are lower than both models described above for the Maria composition. The Highland and high-Titanium Maria compositions always lay above the low-Titanium Maria composition. The Highland composition spans a greater heat capacity range than the Maria compositions. Its heat

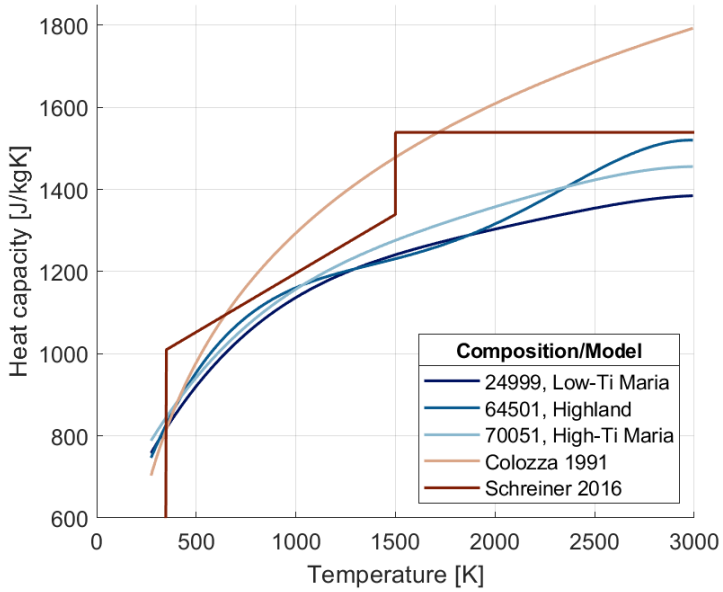

Figure 4.5 Comparison of fitted functions for regolith compositions 24999, 64501, and 70051 at 1 bar with models from Colozza [48] and Schreiner et al. [28]

Table 4.2 Coefficients C and error values R^2 for fitted specific heat capacity functions for regolith compositions 24999, 64501, and 70051 at 1 bar

Composition	C_1	C_2	C_3	C_4	C_5	R^2
24999, low-Ti Maria	-2.69E-11	2.25E-07	-7.33E-04	1.19E+03	4.84E+02	0.96
64501, Highland	-8.14E-11	6.07E-07	-1.59E-03	1.88E+03	3.39E+02	0.97
70051, high-Ti Maria	-2.51E-11	2.04E-07	-6.47E-04	1.09E+00	8.35E+02	0.96

capacity gradient in the molten temperature range is significantly higher. The curve lays below Maria around the melting region at 1500 K, while rising above the Highland curve at temperatures of 2400 K and higher.

Phase transition enthalpies Apparent heat capacity induced by phase transitions or chemical reactions is not visible in the previously shown base heat capacity models. The heat capacities and enthalpies calculated in FactSage include phase transitions and chemical reactions with the latent heat of fusion, latent heat of vaporization/sublimation, and reaction enthalpies. These are also reflected in the heat capacity values, shown in Fig. 4.6. The melting phase can be seen in the figure between 1350 K and 1600 K and the vaporization phase between 2300 K and 2800 K. The melting phase is located in the same temperature range for all pressures above 10^{-5} mbar at which the melting temperature range begins to overlap with the vaporization range, resulting in full or partial sublimation, as also visible in Fig. 4.2.

The melt transition in Fig. 4.6 exhibits an enthalpy increase of 823 kJ kg^{-1} from 1363 K to 1583 K which is representative of the melt transition throughout the melting pressure range. Since the material being melted is a mixture, different compounds melt at different temperatures. This leads to a heat of fusion that is not clearly visible since the enthalpy difference between two points Δh contains both the latent heat of melting L_{pc} and a thermal enthalpy increase, as shown in Eq. 4.2 [71], where T_1 represents the lower temperature bound of the phase change range and T_2 the upper bound. Some components of solid and liquid phases are not undergoing melting in certain sections of the melting range but only get heated. This solid and liquid phase heating can be understood as an additional enthalpy change, which

can be estimated using specific heat capacity values of solid and molten material $C_p(T)$ in Eq. 4.3, where subscript 1 denotes the low temperature phase and 2 the high temperature phase.

$$\Delta h = L_{pc} + \int_{T_1}^{T_2} C_p(T)\, dT \tag{4.2}$$

$$C_p(T) = \frac{C_{p,2}(T_2) - C_{p,1}(T_1)}{T_2 - T_1} T + C_{p,1}(T - 1) \tag{4.3}$$

This enthalpy change of heating is estimated with 276 kJ kg^{-1} and results in latent heat of melting of 546 kJ kg^{-1} for melting transitions from 1×10^{-4} mbar to 1×10^{3} mbar. This corresponds well with values summarized by Schreiner et al. [28] which lie between 400 kJ kg^{-1} and 600 kJ kg^{-1}. Schreiner et al. also gives their own calculated values between 450 kJ kg^{-1} and 480 kJ kg^{-1} which are considerably lower than the FactSage data, but both are still in the previously given range of 400 kJ kg^{-1} to 600 kJ kg^{-1} given by Schreiner et al.

The vaporization range, shown above 2300 K in Fig. 4.6, cannot clearly be divided into separate values for heated liquid or gas, the latent heat of vaporization, and the enthalpy of reaction. All of these are included in the total vaporization range enthalpy difference of 16 400 kJ kg^{-1} at 1 mbar. The total enthalpy change for heated liquid can be estimated with 690 kJ kg^{-1} by extrapolation of liquid phase enthalpy. The combined latent heat of vaporization and enthalpy of reaction in the vaporization region, therefore, result in 15 710 kJ kg^{-1} at 1 mbar. All phase transition data including latent heat is included in the supplementary table B.1. Latent heat of vaporization listed in the table represents vaporization and sublimation in a single value for each pressure in the mixed vaporization/sublimation and in the full sublimation regime. Pressure dependence and applicability of this thermodynamic data for thermal modelling will be discussed in section 5.2.

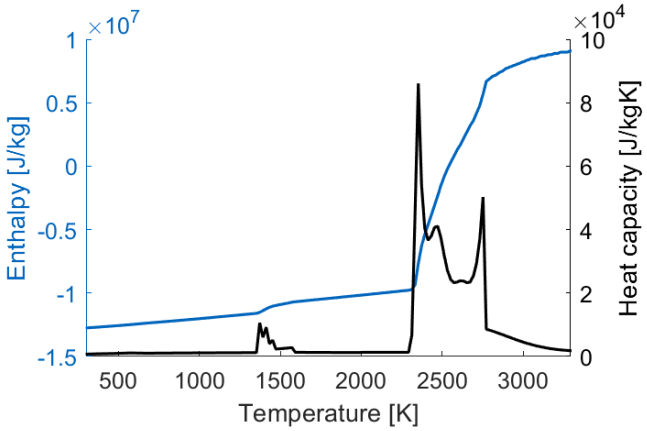

Figure 4.6 Comparison of computed enthalpy and apparent heat capacity during phase transitions of the Maria composition at 1 mbar

4.3.3 Oxygen production

Oxygen gas is produced from lunar regolith during simultaneous vaporization/sublimation and dissociation in a specific temperature range for each pressure. Temperatures in this range will have to be chosen to optimize oxygen production. At first, it has to be defined what parameters define optimal oxygen production.

The first parameter, which was already discussed in several studies, is oxygen yield as defined in Eq. 2.3. It is important to define the yield for O_2 production instead of a combined O_2 and O production since atomic oxygen can aggressively react with reactor hardware and other suboxide species (discussed in section 2.3.3). O_2 yield is shown in 4.7a. Higher yields are shown in darker red at the lower end of the pressure range around 1500 K at approximately 13.5%. The highest values for each discrete pressure are called peak yields in the following sections. Peak yield drops off towards the higher pressures where the peak yield only reaches up to 10%. This reduction in peak yield is likely linked to a wider vaporization temperature range at higher pressures, a wider range of relatively high O_2 yield (9% - 10%), but a lower peak O_2 yield value.

Atomic oxygen (O) yield, shown in Fig 4.7b, increases from nearly 0% at the temperatures where O_2 yield peaks to values above 40%. At full vaporization and dissociation of oxides, all of the oxygen present in the initial regolith is expected to be in an atomic state. The transition from 0% to 25% O yield roughly follows the vapor phase transition. There is a second transition visible from approximately 25% to 40%. This can be attributed to the dissociation of gaseous SiO, which is the last suboxide to dissociate to Si and O. This can be seen in Fig. 4.8, which shows the composition of the gas phase for different temperatures at 10^{-5} mbar. Above approximately 2700 K a decrease in the weight of SiO and an increase in Si and O can be seen.

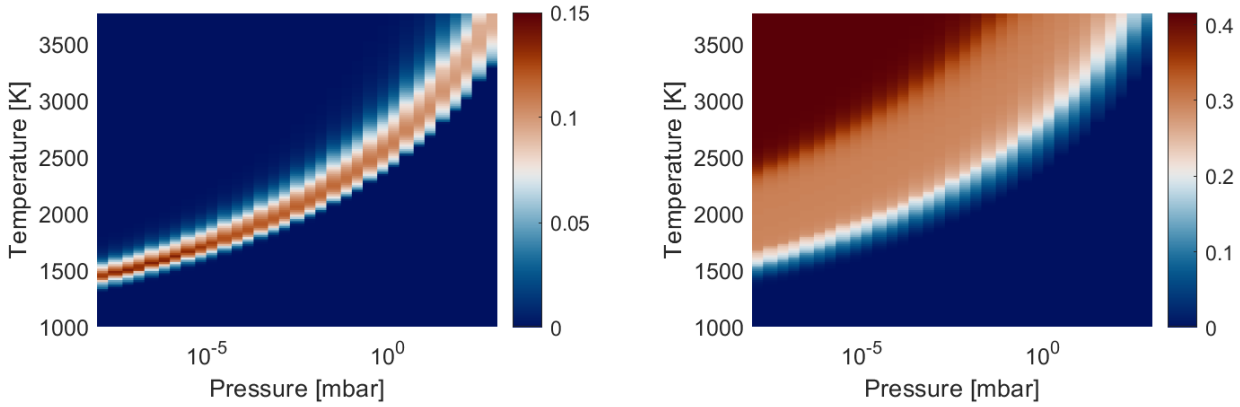

(a) O_2 yield **(b)** O yield

Figure 4.7 O_2 and O yield for the Maria composition for pressures 10^{-8} mbar to 10^{3} mbar and temperatures 1000 K to 3773 K

Data shown in Fig. 4.8 is also useful for investigating the origin of the molecular and atomic oxygen, which can give insight into what oxides and minerals are being reduced at which temperatures. Fig. 4.8a shows gas evolution as a mass fraction of initial bulk regolith, and Fig. 4.8b shows the gas evolution as a mass fraction of produced gas. Some minor gas species have been left out of the figure for clarity since they do not contribute significantly to the gas quantity. The most notable not-included species are Mn and initial oxides, which vaporize/sublimate but do not entirely dissociate immediately with vaporization/sublimation (TiO_2 and CrO_2). These figures show the gas species at 10^{-5} mbar. Similar gas evolution can be observed at other pressures with a shifted temperature range, where the shift follows the vapor phase transition as shown in Fig. 4.3 or Fig. 4.2. Fig. 4.8c and Fig. 4.8d show the gas evolution at 1 mbar which looks qualitatively similar to the evolution at 10^{-5} mbar, only shifted approximately 800 K higher.

Oxides are shown to dissociate in the following order: Na_2O, K_2O, FeO, SiO_2, MgO, CaO, CrO_2, TiO_2, Al_2O_3. Na_2O and K_2O evaporate at significantly lower temperature of 1300 K and 1500 K in the low pressure case (Fig. 4.8b). Evaporation of sodium and potassium happens at higher temperatures and is therefore not visible that well in Fig. 4.8d since their fraction of gas is comparatively low at that point.

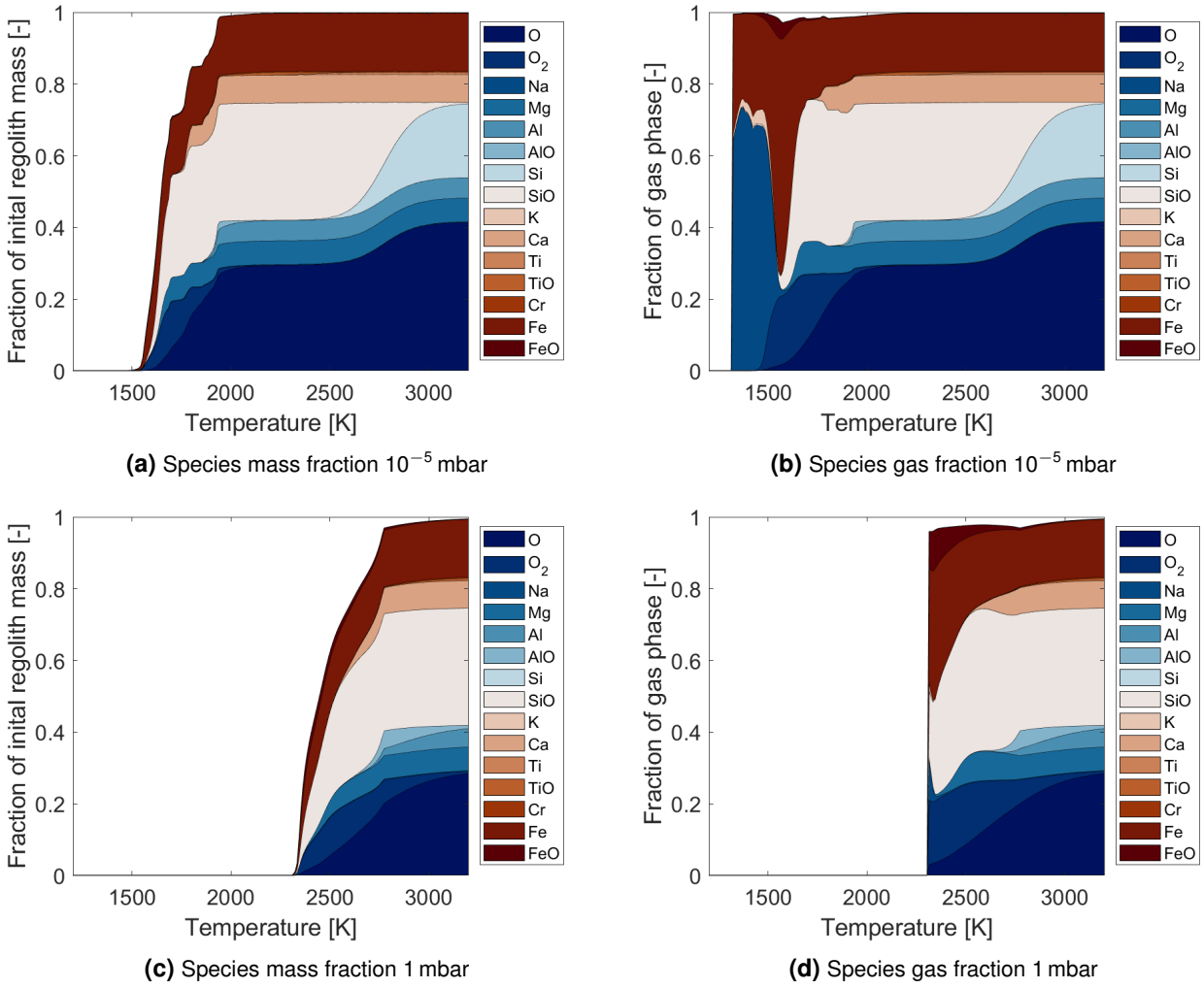

(a) Species mass fraction 10^{-5} mbar

(b) Species gas fraction 10^{-5} mbar

(c) Species mass fraction 1 mbar

(d) Species gas fraction 1 mbar

Figure 4.8 Maria regolith: gaseous species mass as fraction of initial regolith mass at 10^{-5} mbar (a), at 1 mbar (c), gaseous species mass as fraction of gas mass at 10^{-5} mbar (b), and 1 mbar (d)

Dissociation in suboxides before a full dissociation can be seen with SiO_2, TiO_2, Cr_2O_3 which dissociate into SiO, TiO and CrO_2, before dissociating fully.

The most important region for oxygen production is the temperature range where the most O_2 is present in the gas phase. This range can be seen between 1450 K and 1900 K at 10^{-5} mbar in Fig. 4.8a and between 2300 K and 2770 K at 1 mbar in Fig. 4.8c. The oxides which contribute to the production of O_2 the most in this temperature range are shown to be FeO, SiO_2 and MgO, seen through the production of gaseous Fe, SiO, and Mg. Above this range, more refractory oxides (CaO, CrO_2, TiO_2, and Al_2O_3) as well as existing gaseous O_2 dissociate primarily to atomic oxygen, showing that high temperatures above the previously mentioned temperature ranges should be avoided for O_2 production.

Peak O_2 yield might not be the ideal metric for choosing reactor conditions due to the existence of O and other species in the gaseous phase at higher temperatures. Therefore, it is useful to look at the O_2 mass fraction of total gas m_{O_2}/m_{gas} (Fig. 4.9a). A high mass fraction of O_2 would likely simplify the extraction of O_2 from the reactor chamber due to the lower fraction of residual material that has to be condensed or filtered from the vapor. Another metric is the m_{O_2}/m_O mass ratio (Fig. 4.9b), which can be used to optimize temperatures based on the amount of molecular oxygen while keeping the amount of atomic oxygen in the reactor low. In both figures, the white dashed line represents the temperature of maximal

O_2 yield. Both figures show a peak at temperatures lower than the peak O_2 yield. A better comparison is shown in Fig. 4.10, where temperatures for peak O_2 yield, mass fraction of gas and the O_2/O mass ratio at different pressures are shown together. Peak O_2 yield and the O_2/O mass ratio are sensible upper and lower bounds of the temperature range to be considered when optimizing reactor conditions. The mass fraction of gas lays between the two bounds, closer to the peak O_2 yield line below 10^{-1} mbar and closer to the lower bound, O_2/O mass ratio line, above this pressure. No optimal line can be determined at this point because the trade-offs between these metrics must be done during a design of a pyrolysis reactor. Nevertheless, the process temperature optimization should strive for temperatures closer to the peak O_2 yield line to achieve efficient O_2 extraction from bulk regolith.

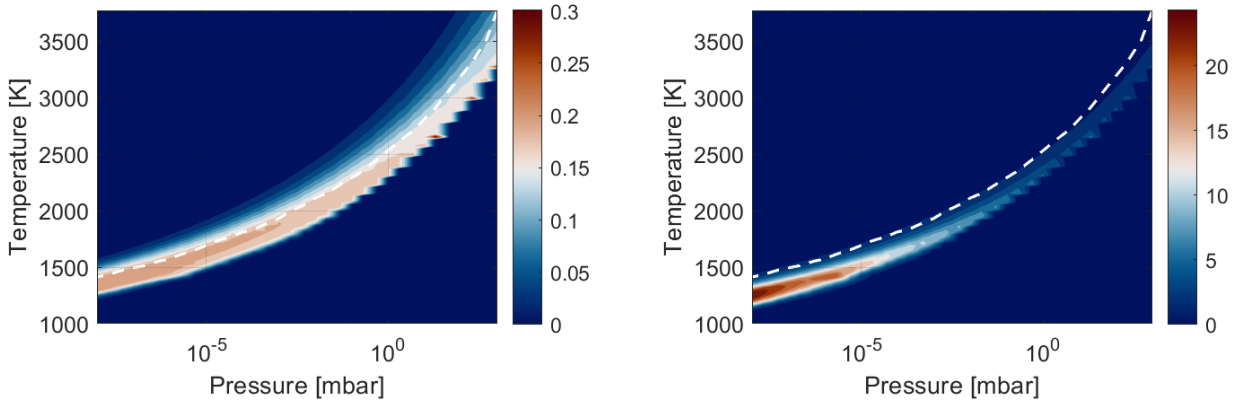

(a) O_2 mass fraction of gas

(b) Mass ratio O_2/O

Figure 4.9 O_2 mass fraction of gas and mass ratio O_2/O for the Maria composition for pressures 10^{-8} mbar to 10^{3} mbar and temperatures 1000 K to 3773 K, white dashed line represents the temperature of peak O_2 yield at given pressure.

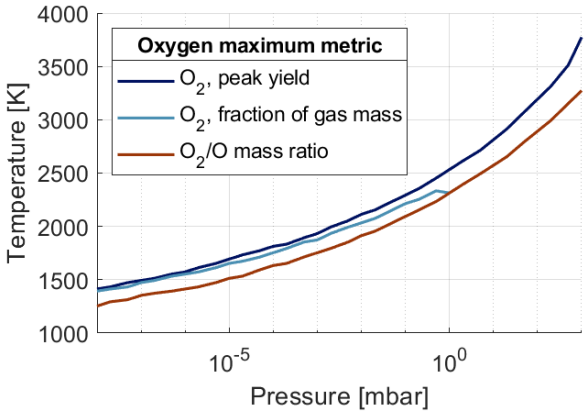

Figure 4.10 Comparison of oxygen production metrics: temperature of peak O_2 yield, peak O_2 mass fraction of total gas, and the peak mass ratio O_2/O

4.3.4 Comparison of regolith compositions

In the previous sections, thermochemical data has only been analyzed using the Maria regolith composition previously introduced in section 4.1. The following section gives insight into the differences between analyzed compositions. The oxygen production metrics, peak O_2 yield, and temperature range of the

peak yield for each pressure, as chosen previously for the low-Ti Maria composition, are shown here also for Highland, high-Ti Maria, and EAC-1A compositions.

The temperatures which produce peak O_2 yield values are compared in Fig. 4.11, shown in solid lines. Their behavior is very similar, with only the highland composition deviating slightly at high pressures above 10 mbar. These temperatures can be fitted well with third-order polynomial functions of form Eq. 4.4 with coefficients shown in Tab. 4.3. This is done to show, that all these values approximately follow a third-order polynomial, which can be used for further calculations. This function is purely a mathematical fit and not physics-derived. The valid range for these functions is 10^{-8} mbar to 10^{1} mbar, because the peak O_2 yield of some compositions for the pressure between 100 mbar and 1000 mbar lay at the upper-temperature boundary of the simulation at 3772 K, so it cannot be confidently said these values are the true peak O_2 yield. Dashed lines in Fig. 4.11 represent the lowest temperatures where the maximal O yield occurs and are shown primarily for comparison and orientation. They also follow a similar polynomial function, although they are cut off at the upper-temperature boundary above approximately 10^{-4} mbar.

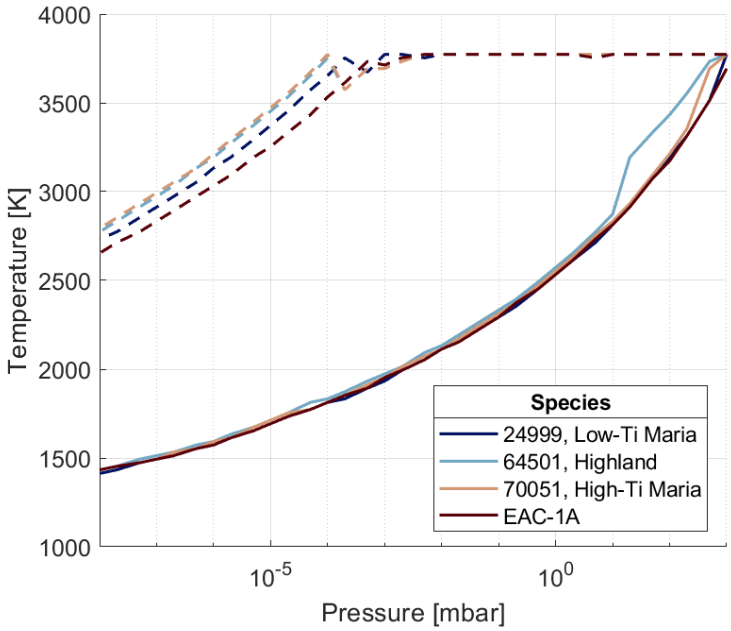

Figure 4.11 Peak O_2 (solid line) and peak O (dashed line) yield temperature as a function of pressure for regolith compositions 24999, 64501, 70051, and simulant EAC-1A.

$$T_{max,O_2} = C_1 log(p)^3 + C_2 log(p)^2 + C_3 log(p) + C_4 \tag{4.4}$$

Table 4.3 Regolith and regolith simulant compositions used for thermochemical simulations

Composition	C_1	C_2	C_3	C_4	R^2
24999, low-Ti Maria	2.006	33.70	282.0	2522	0.9982
64501, Highland	2.213	37.80	309.4	2596	0.9969
70051, high-Ti Maria	1.183	25.03	267.5	2560	0.9998
EAC-1A	1.208	25.00	264.2	2544	0.9997

The second important metric for comparison of regolith compositions for oxygen production suitability is the peak O_2 yield for each of the pressures. Fig. 4.12 shows these peak O_2 yields for each regolith composition. Low-Ti Maria, High-Ti Maria, and EAC-1A all show very similar behavior with a minimum

yield at the highest pressure of 1000 mbar and highest yield between 10^{-6} mbar and 10^{-7} mbar. The difference between these three yield lines is primarily the absolute magnitude, with the High-Ti Maria laying approximately 1.8% lower than the Low-Ti Maria and EAC-1A laying approximately 3% higher than the Low-Ti Maria yields.

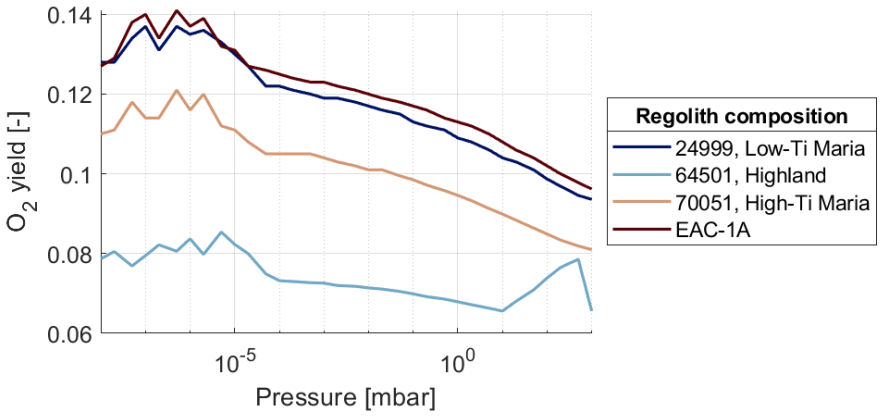

Figure 4.12 Comparison of peak O_2 yield as a function of pressure for regolith compositions 24999, 64501, 70051, and simulant EAC-1A.

The highland composition shows similar behavior to other compositions but lays approximately 0.05 below the Low-Ti Maria. This composition also shows a significant increase in yield above 10 mbar. This higher yield can also be seen in Fig. 4.13b. A shorter second yield peak can be seen after a first increase. For example, a yield of 0.063 is reached initially at around 3400 K at 200 mbar and a second peak can be seen at 3550 K with a yield of 0.077. These secondary peaks contribute to the increase in yield at higher pressures. At 1000 mbar, an expected secondary peak falls out of temperature bounds for these calculations. Therefore, the maximum yield is decreased again compared to the next-highest pressure of 500 mbar. The occurrence of a secondary peak also explains the shift in the peak O_2 yield temperature for highland composition in Fig. 4.11.

Another prominent feature of all yield lines in Fig. 4.12 is the increase in peak O_2 yield from around 10^{-4} mbar nearly to the lower pressure bound of 10^{-8} mbar, where it decreases again. This increase in peak O_2 yield coincides with the sublimation pressure range, which lays below 10^{-5} mbar as also shown in the supplementary figure B.1b.

Other ratios mentioned in section 4.3.3, O_2 mass fraction of gas and the O_2/O mass ratio for all four compositions, are plotted in the supplementary figures in the Appendix (Fig. B.5 and Fig. B.6).

4.3.5 Comparison with regolith dissociation values from literature

The results of thermochemical modelling are mostly consistent with previously done studies with small differences in the oxygen yield values. Comparison of the dissociation behavior and oxygen yields from this model and literature are discussed in the following.

Dissociation behavior Gas species evolution at different temperatures can be compared to a previously developed model by Shaw et al. [15] to sow agreement between the two models. Fig. 4.14 shows the produced gas species as a fraction of total gas at 10^{-15} bar using 100 K temperature steps, and the corresponding data from Shaw et al. [15] for the same conditions. Both datasets were calculated

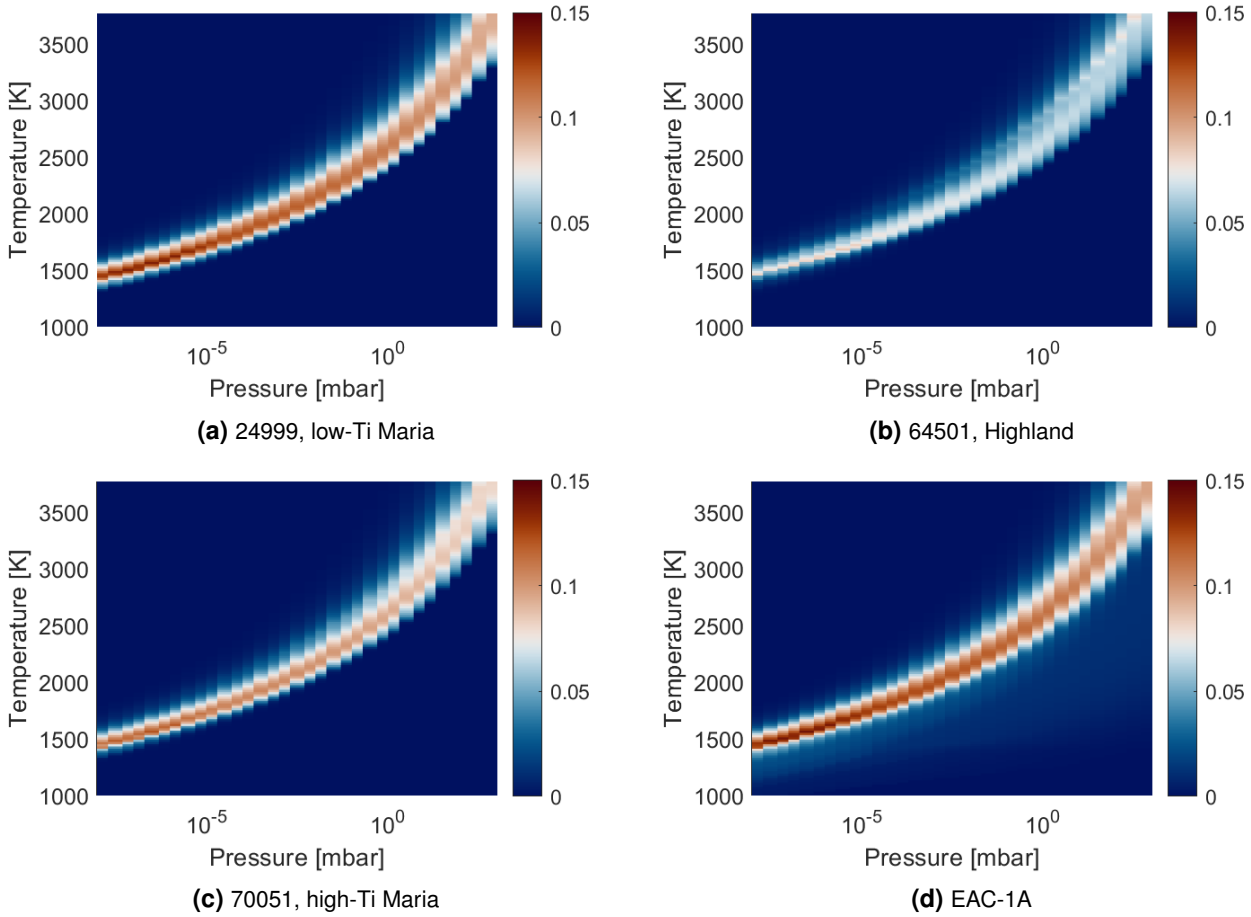

(a) 24999, low-Ti Maria

(b) 64501, Highland

(c) 70051, high-Ti Maria

(d) EAC-1A

Figure 4.13 O_2 yield of regolith compositions 2499, 64501, 70051, and simulant EAC-1A for different pressures and temperatures

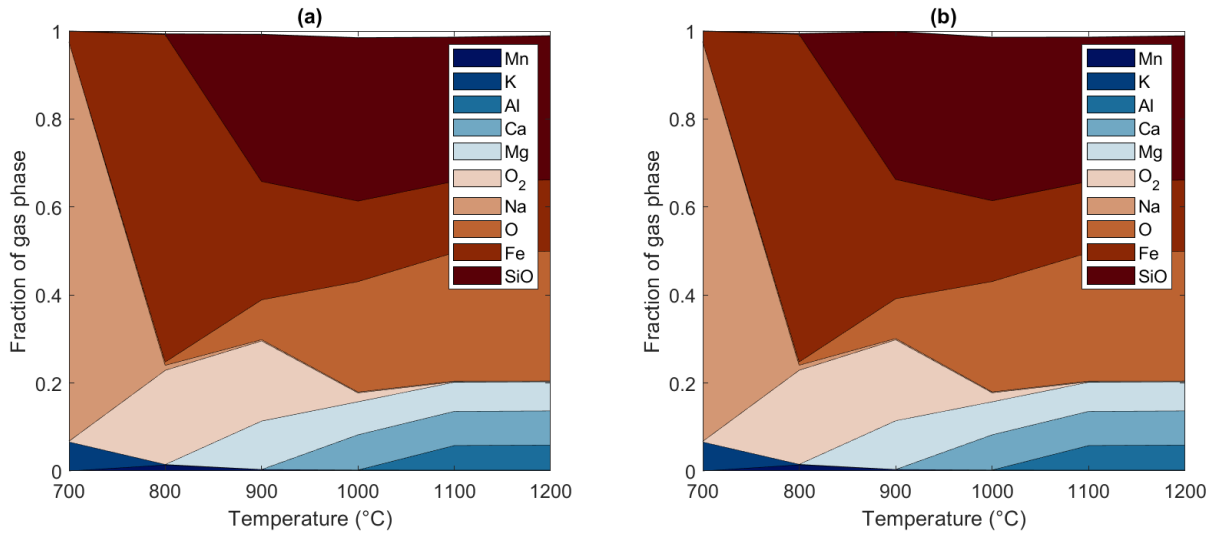

Figure 4.14 Gaseous species as fraction of total gas mass at 10^{-15} bar (10^{-12} mbar) as produced by (a) the calculations in this thesis and (b) the model by Shaw [69]

using FactSage software with Shaw using the additional databank FSstel for improved results in metallic compounds. Gas evolution is shown to be qualitatively consistent between the plots in Fig. 4.14.

The dissociation behavior can also be compared with the calculations done by Matchett [14], shown in Fig. 2.3. The order of dissociation of the species is very similar, with one slight difference. MgO is shown to dissociate before SiO_2, although the dissociation ranges are heavily overlapping in both studies. Therefore, it can be assumed that MgO and SiO_2 dissociate at approximately similar temperatures.

Oxygen yields This thesis focuses on oxygen production, so metal species and their characteristic temperatures are not studied in detail. For the purposes of oxygen production, it is important to determine the dissociation of which oxides contribute the most to O_2 production. These oxides are FeO, SiO_2 and MgO, which is consistent with the stated low-temperature pyrolysis behavior in Senior and Matchett [11, 14]. The high-temperature pyrolysis range during dissociation of Al, Ti, and Ca oxides primarily shows production of atomic oxygen as shown in Fig. 4.8a above. This contradicts the O_2 yields (0.25 to 0.35) for this high-temperature pyrolysis range calculated by Senior [11] since the calculations in this work show primarily O production during dissociation of these more refractory oxides. Maximum O_2 yields given for the low-temperature pyrolysis are given as 0.16 and 0.20 for highland and mare soils, respectively. Maximum yields calculated in this thesis lay between 0.10 and 0.14 for highland and mare soils, respectively, which is more than a 30% lower yield compared to the values stated by Matchett.

Steurer and Nerad [37] state that the oxygen yield of FeO is zero. This contradicts the results shown in Fig. 4.14 and 4.8 which show generation of Fe and O_2 at the same temperatures and can be interpreted as dissociation of FeO. This is also confirmed by Senior [11] and [14], noting that the vapor pressure of Fe is significantly higher than that of FeO, resulting in oxygen production due to the dissociation of FeO.

4.3.6 Estimation of realistic yield values

Equilibrium calculations are inherently an ideal solution for generation of oxygen and other products from pyrolysis. Kinetics of these reactions are expected to be slower than the economical timespans of the regolith heating process, so the reaction would likely not reach equilibrium in an actual pyrolysis reactor [11, 69]. Additionally, striving for equilibrium would not be sensible from the reaction rate point of view since the forward reaction rate slows towards equilibrium defined by the equilibrium constant K in Eq. 2.9. Kinetics of the process have to be studied to determine optimal reaction parameters for yield or production rate. A study of regolith vapor phase pyrolysis kinetics has not yet been conducted, so no qualitative values can be used to estimate real yields based on reaction kinetics.

Senior [11] approximated realistic yields by using experimental data from Yakovlev et al. [72]. By using their maximum O_2 yield of 0.35 and the experimental result of 0.2 from Yakovlev et al., a 60% efficiency was assumed. Another consideration has been made regarding the amount of vaporized/sublimated material, since regolith can vaporize/sublimate fully or only partially based on the temperature regime. Assuming vaporization/sublimation between 25 and 100% and a 60% yield efficiency, a lower bound of 15% and an upper bound of 60% can be assumed. Estimated O_2 yield for all compositions is shown in Tab. 4.4.

Table 4.4 Minimum and maximum peak O_2 yields taken from the equilibrium calculations for pressures between 10^{-8} mbar and 10^{3} mbar and estimated realistic yield calculated using estimates from Senior [11]

Composition	min. peak yield	max. peak yield	est. min. yield	est. max. yield
24999, low-Ti Maria	0.094	0.137	0.014	0.082
64501, Highland	0.066	0.085	0.010	0.051
70051, high-Ti Maria	0.081	0.121	0.012	0.073
EAC-1A	0.096	0.141	0.014	0.085

5 Thermal modeling of solar vapor pyrolysis

This chapter describes the modeling of the thermal reduction of regolith in a vacuum under concentrated solar irradiation using a regolith surface thermal model and evaluating the thermal results using the oxygen yield from the equilibrium modeling (Section 4).

Firstly, the general idea of the model is described, and the main simplifications and assumptions are given. Secondly, the thermal model and its validity are described. Thirdly, a simple combined model is presented, incorporating the equilibrium calculation results to evaluate the thermal model. In the end, a comparison with the experimental results is given and discussed.

5.1 Model setup

The computational model is a combination of a thermal and a thermochemical model. Each of them is described in the following sections in greater detail, and the basic setup connecting these is presented here.

Reactors The process is analyzed in 3 different closed or semi-closed reactor systems representing best, middle, and worst case scenarios for pressure and the resulting oxygen generation, shown in Fig. 5.1. As apparent from literature (Section 2.3) and experimental work conducted for this thesis (Section 3), oxygen generation is heavily dependent on reactor pressure. These reactors attempt to give insight into pressure behavior and oxygen production of a small pyrolysis reactor like the one built in section 3. Primary size and power parameters are based on the experimental setup from this thesis but could be scaled up for larger reactor volumes or higher solar concentrations.

All reactor variants have the same solar irradiance, volume, amount, and type of regolith. The regolith composition modelled is low-Ti Maria 24999 (Section 4.1). The reactors differentiate in the logic of how pressure inside the reactor is calculated. Variant I (I-M) is the ideal reactor case with assumed constant pressure regardless of how much gas is generated from the regolith. This can also be seen as a reactor where the produced gas is constantly removed from the system with the assumption that the material composition inside the reactor does not change.

Variant II is a fully closed system as opposed to Variant I and represents a middle-case scenario. The thermochemical model produces gas, which is a mixture of oxygen, metal, and suboxide species that ideally exist in the vapor phase. This is not a realistic assumption for a real reactor with a non-homogenous temperature throughout the system and potentially large temperature gradients across the sample and reactor surfaces. This would lead to condensation of metallic and suboxide species on colder parts of the sample as well as the reactor surface. This can be seen in literature [14, 15] as well as in experiments in section 3, where a condensate can be seen on the inspected samples and crucible surface. Therefore, reactor variant II assumes a full condensation of all gaseous species except O_2, which remains gaseous and increases reactor pressure.

Variant III simplifies Variant II even further with the assumption that none of the gaseous species condense and all increase the reactor pressure. With all species adding to the reactor pressure, it rises the most out of all variants and is considered the worst-case model of the reactor.

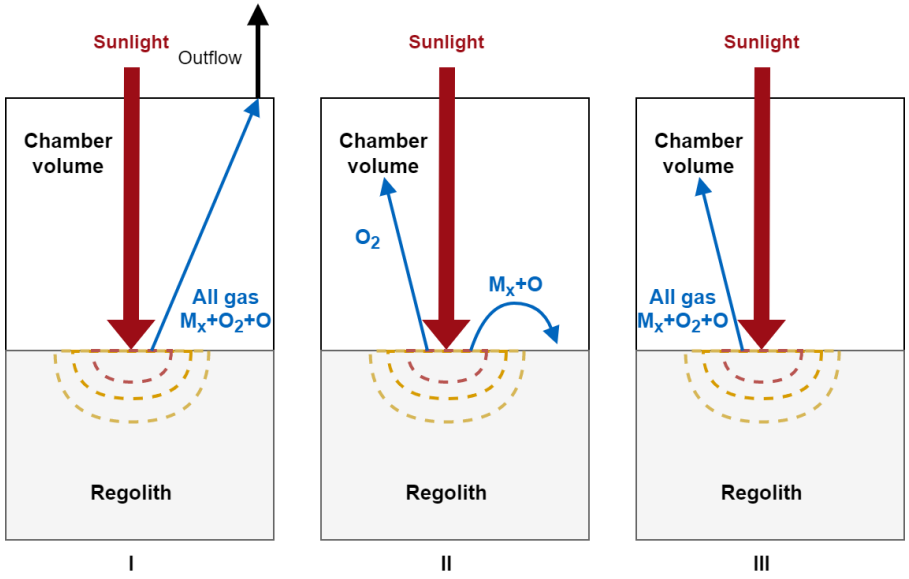

(a) Gradient solution

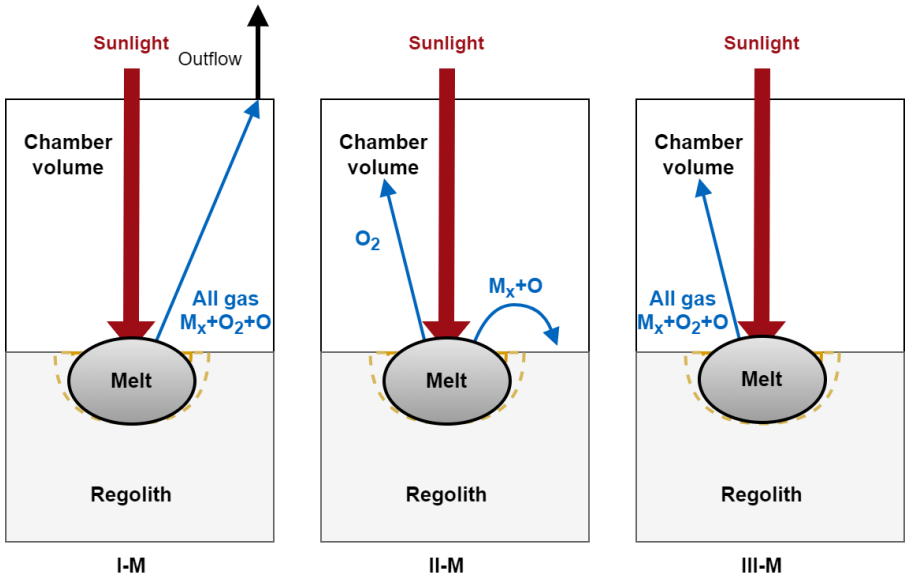

(b) Melt solution

Figure 5.1 Modelled reactor variants: (a) Solution based on the temperature gradient in the regolith surface (I - an ideal case, all gas products are removed continuously; II - middle case, oxygen gas remains in the chamber, other species condense immediately; III - worst case, all gas products remain in the chamber); (b) Solution based on a calculated melt volume (I-M, II-M, and III-M are analogous to the reactor cases from (a) but for the melt-based solution)

The heat transfer in the regolith surface is modeled in a solid state, which is primarily valid for the sublimation regime where evaporation happens directly from solid material without an intermediate liquid phase. A melt consideration (Fig. 5.1b) is introduced to these reactors, with variants I-M, II-M, and III-M, using the results from the solid state heat transfer simulations for pressures above the sublimation range. All material with a temperature above the assumed melting point of 1450 K is analyzed as a single volume with a homogenous temperature.

Modeling assumptions All variants of the reactor are still very simplified models of a real reactor. This simplified modeling approach is required due to several assumptions about thermochemical and mass transport effects in the reactor, keeping computation complexity low. The simplifying assumptions are similar to the ones for the thermochemical equilibrium modeling with a few additions:

- The system is assumed to be at chemical equilibrium. All reactions with slow reaction kinetics have been completed.
- Parts of the system can reach different chemical equilibrium states due to the different temperatures and the overall reactor pressure, which is homogenous throughout the reactor.
- Material composition is homogenous and has no local differences. All compounds, atoms, or molecules can interact with each other and achieve the lowest possible energy state.
- The regolith sample does not contain any volatile material which would outgas at modeled temperatures or change the thermal or chemical behavior of the sample.
- Mass transfer through bulk and melted regolith is neglected. It is assumed that each produced atom or gas molecule adds directly to the reactor pressure or can instantly be removed from the reactor.
- All oxides are soluble in the melt.
- Thermal simulations are done as a solid state model. Geometric, volume, and density changes of the regolith sample during melting are neglected in the thermal surface model, while mass and energy are conserved.
- Re-irradiation of the regolith surface due to reflections from reactor walls is neglected in the thermal model.

5.2 Thermal model of the regolith surface under a concentrated solar beam

This section provides an overview of the thermal model of the regolith surface under concentrated solar radiation constructed in COMSOL Multiphysics [73]. It describes the integration of optical data as a boundary condition, implementation of the thermal properties of regolith, and studies the quality of the numerical model.

5.2.1 Optical parameters

The optical parameters of the concentrated solar beam define the main boundary condition for building a thermal model of a regolith surface being heated by concentrated solar energy. The calculations for the optical losses of the experimental solar vapor pyrolysis reactor and the associated total absorbed energies were discussed in the experimental chapter in section 3.1.4. This section focuses on the distribution of this total flux over the regolith surface.

The considered parameters include the solar spectrum on the Moon and Earth, the system setup, optical elements, and the type of bulk regolith. The most important of these parameters is the energy flux density distribution over the regolith surface, which is produced by the beam of the Fresnel lens. The form of a flux density function roughly follows a gaussian distribution. The form of this gaussian function and the corresponding power are investigated here so they can be implemented in the thermal model. A gaussian function set as a boundary condition in COMSOL Multiphysics is described in Eq. 5.1, with $r = \sqrt{x^2 + y^2}$

being the radius coordinate on the regolith surface plane, σ the standard deviation of the gaussian function, and ϕ_{abs} the absorbed energy flux [71].

$$E_{abs,Gauss}(x, y) = \Phi_{abs} \cdot \frac{1}{2\pi\sigma^2} \cdot e^{-\frac{r^2}{2\sigma^2}} \tag{5.1}$$

The parameter σ was determined using an optical model of the Fresnel lens in a ZEMAX OpticStudio sequential analysis [74]. The lens model is available through the manufacturer Edmund Optics [62]. An initial collimated solar beam was defined as the input into the lens using the ASTM G173 AM1.5 spectrum previously discussed in section 3.1.4. A detector surface was placed at the focal distance given by the manufacturer and the arriving flux density distribution was measured. An overview of this simple setup is shown in Fig. 5.2. The RMS radius value of the beam at the detector can be measured in OpticStudie, which is taken as the σ value for the Gaussian function. The RMS spot radius at the focal point is 3.45 mm.

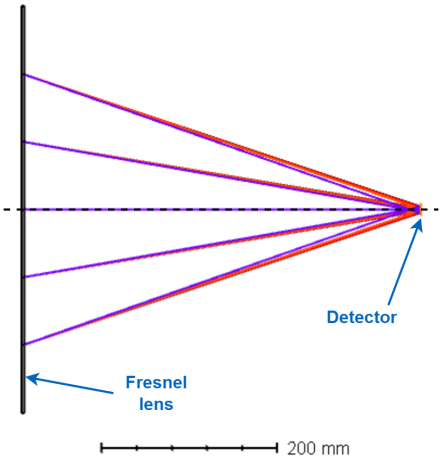

(a) Layout of the optics model

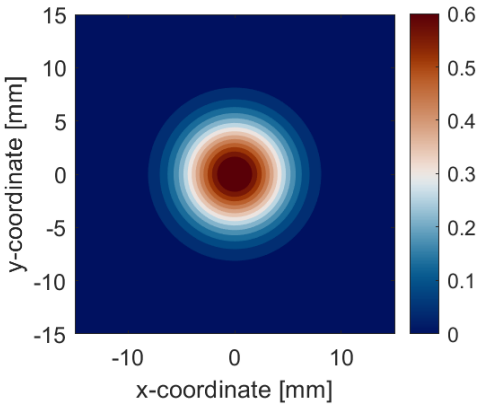

(b) Gaussian beam flux distribution at Φ_{abs} = 50 W [W mm^{-2}]

Figure 5.2 Optical model for determination of the gaussian function. (a) The layout of the optical model in Zemax Opticstudio. (b) Resulting gaussian distribution on the regolith surface at 50 W.

The change in flux distribution was studied to determine the uncertainty induced by lens positioning. This is done by shifting the detector along the optical axis (closer or farther from the lens) to see its effect on the flux distribution and the RMS value and estimate focusing errors during the experiments in section 3. The RMS value as a function of detector distance from the lens is shown in Fig. 5.3. A nominal RMS value of the spot at the nominal focal distance of 452.2 mm is 3.45 mm. An estimated uncertainty for the distance between the lens and the surface of $\pm$3 mm is assumed for the experiments in section 3, resulting in lens-surface distance bounds of 449.2 mm to 455.2 mm. The change in spot radius and spot area can be read from Fig. 5.3. For both directions of uncertainty, the radius and area increase with increased distance from the focal length. The resulting uncertainty for RMS spot radius is +3.7% at 449.2 mm and +5.5% at 455.2 mm. The uncertainty values for the change of spot area are 7.5% and 11.3%, respectively. These values define the rough uncertainty but a more comprehensive uncertainty study would have to be performed to study the influence of this values on regolith heating an oxygen production.

5.2.2 Setup and geometry of the surface thermal model

The Gaussian beam is applied as a boundary condition to a quasi-semi-infinite regolith material with a boundary on the regolith surface and a distant depth boundary which makes the domain quasi-infinite in depth for exposure times up to 3600 s considered in this study. The geometry of this regolith material is

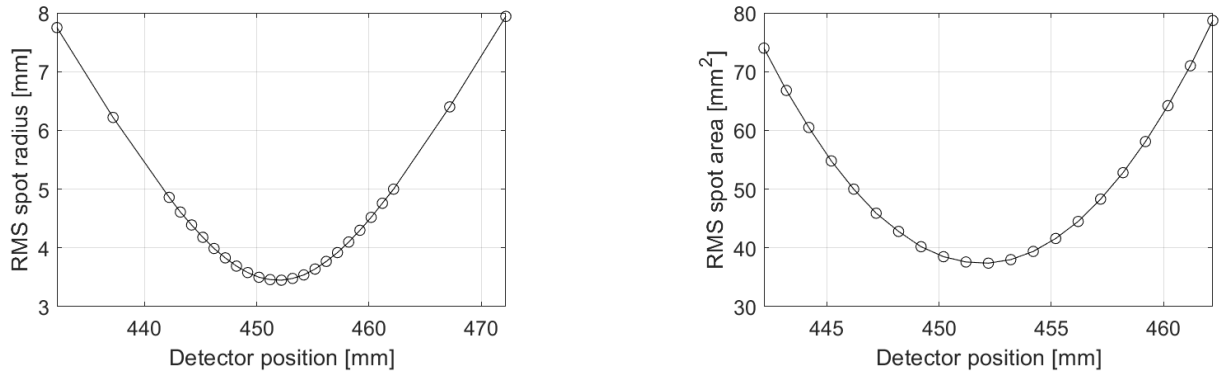

(a) Radius **(b)** Area

Figure 5.3 RMS values of solar spot radius and area as a function of lens-detector distance in the optical model in Zemax OpticStudio.

modeled in COMSOL as a rotation-symmetric 2D model. Fig. 5.4 shows a cross-section of the rotation geometry and the rotation axis at r = 0. The geometry is subdivided into three regions for the mesh definition: an inner square domain directly under the solar beam and an outer domain consisting of the remaining two rectangular regions. The inner domain will allow for a finer definition of the mesh in the region of high-temperature gradients directly under the solar beam interface. The outer domain serves as an approximation of the self-embedded concept for thermal insulation in concentrated solar regolith batch processes, where unreacted bulk regolith is used as the insulation between the melt and the crucible [11].

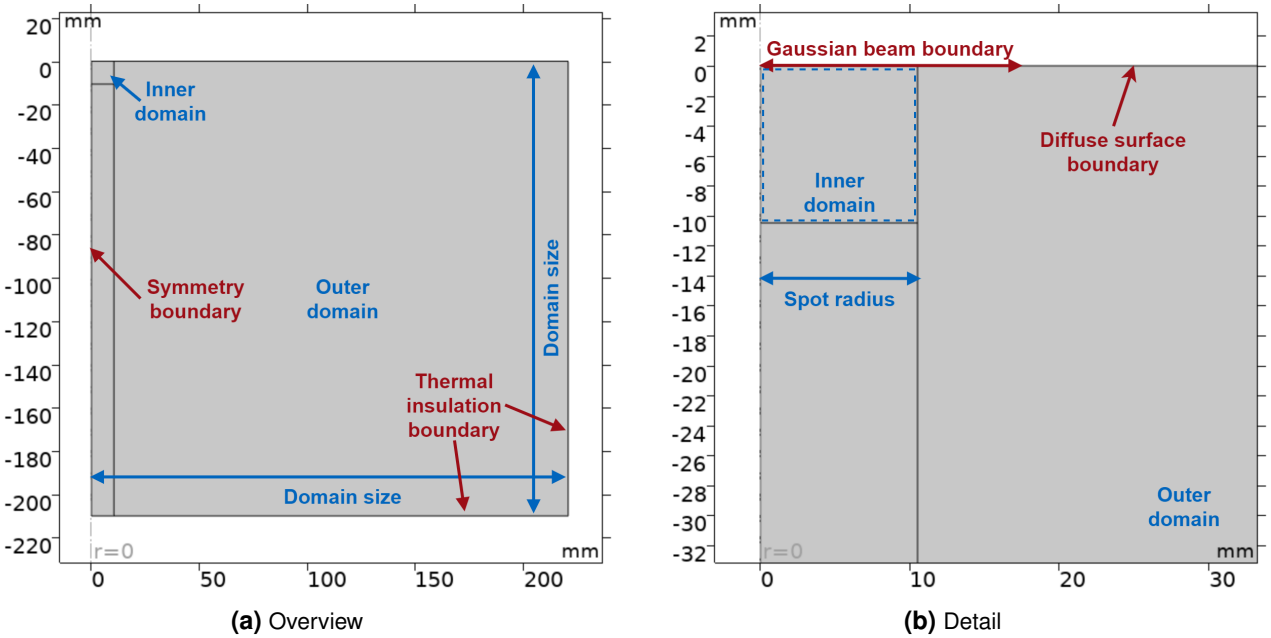

(a) Overview **(b)** Detail

Figure 5.4 Rotation-symmetric geometry of the thermal model with marked mesh factors and boundary conditions in COMSOL Multiphysics

Boundary conditions The thermal model of the regolith surface has four boundary conditions marked in Fig. 5.4. A thermal insulation boundary ($\dot{q} = 0$) is defined on the bottom and side edges of the geometry. A symmetry boundary is set at the inner edge ($r = 0$) of the geometry. The whole upper edge, representing the regolith surface, is a diffuse surface boundary with a radiative flux proportional to T^4 as given by the

Stefan-Boltzmann law [75] in Eq. 5.2, with Φ being the radiative flux, ϵ being the emissivity of the surface, σ the Stefan-Boltzmann constant, A the surface area, T the temperature of the surface and T_{ref} a reference temperature of 298 K. The emissivity ϵ has to be defined as a constant, which is presented in the following section, discussing regolith properties.

$$\Phi = \epsilon\sigma A(T^4 - T_{ref}^4) \tag{5.2}$$

The last boundary condition is the deposited Gaussian beam boundary as defined in section 5.2.1 with the Eq. 5.1, which represents the solar flux absorbed in the surface. The absorption properties are considered separately as described in section 3.1.4 and section 2.4.2.

5.2.3 Implemented regolith material properties

The thermal and physical properties of regolith and simulants used in the model are primarily based on the review of thermophysical property models by Schreiner et al. [28]. The exceptions are emissivity and heat capacity. The latter was taken from the thermochemical calculations described and compared with existing models and measured values in section 4.3.2.

Density Regolith density is the most straightforward property implemented in this model. A constant value of 1500 $\mathrm{kg\,m^{-3}}$ is assumed, which corresponds with the average density of the top 15 cm of lunar soil [17, 28]. This is representative of bulk regolith density but not of molten regolith, which has a higher density of 2500 $\mathrm{kg\,m^{-3}}$ to 2900 $\mathrm{kg\,m^{-3}}$ [28]. The thermal model of the regolith surface is defined with constant volume without a moving melt boundary or a specific gas volume above the regolith surface. All phases exist in the same volume as the initial unreacted bulk regolith. Due to the constant volume of the model, a constant density must be assumed to fulfill the thermal model's mass conservation condition.

Thermal conductivity The model for thermal conductivity k is taken from Schreiner et al. [28], which was fitted over empirical solid and molten data above 1500 K. It is assumed, that thermal conductivity does not change with pressure, as described in section 2.1.2. This is completely valid for pressures below 10^{-1} mbar. Above this pressure the same model is also used for simplicity. The model is shown in Fig. 5.5 using the equation Eq. 5.3. The equation uses a temperature T' in kelvin, normalized by a mean of 691.7 and a standard deviation of 564.3. The validity is reasonable in solid and molten phases but decreases during the vaporization and sublimation regimes. Complete vaporization will not be reached in the thermal model, so this model is still a good approximation of thermal conductivity.

$$k = \frac{0.01257(T') + 0.0172}{(T')^2 - 2.874(T') + 2.085} \tag{5.3}$$

Emissivity Thermal gradients in the regolith surface are significantly dependent on the radiative properties of the regolith surface through radiation to the environment. This is especially the case at high temperatures on the order of 1500 K to 2500 Kachieved during solar heating due to the radiative flux being proportional to T^4. The most important part of the surface for emissivity determination is the molten regolith due to the highest temperatures. The surrounding regolith, which has a temperature close to ambient, is assumed to have little influence on thermal behavior.

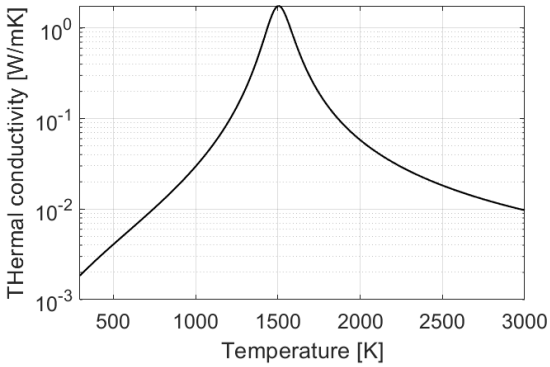

Figure 5.5 Thermal conductivity model by Schreiner et al [28]

Literature provides emissivity values only for low-temperature solid regolith, which are not applicable for molten regolith at high temperatures. Emissivity has therefore been taken from a measurement of terrestrial basalt lava from Ball and Pinkerton [60], which gives emissivities in the range of 0.973 to 0.984. A middle value of 0.98 has been taken for the thermal model, which also coincides with the emissivity settings of the IR camera used in the experiment in section 3.

5.2.4 Heat capacity model

An important factor for thermal modeling of pyrolysis is to account for the energy being used for thermal reduction of oxides while modeling the heating of regolith, melting, vaporization, and sublimation. Data from the thermochemical model (section 4.3) already provides the needed enthalpies for modeling. Fig. 4.6 shows the enthalpy and heat capacity data resulting from thermochemical modeling. This data includes all enthalpies and apparent heat capacities for phase changes and reaction enthalpies. Ideally, this data would be used directly in the thermal model of the regolith surface. Since the thermal model is a numerical, finite-element-model, it does not work well with sharp peaks visible in the heat capacity line in the previous chapter in Fig. 4.6 and in Fig. 5.6a, where heat capacities for different pressures are shown. This is especially problematic at low pressures, where C_p peaks become more prominent. These peaks introduce intense non-linear behavior to the material properties that has a detrimental effect on computational load, the solver, and the quality of the result. Another approach is implemented to solve this problem.

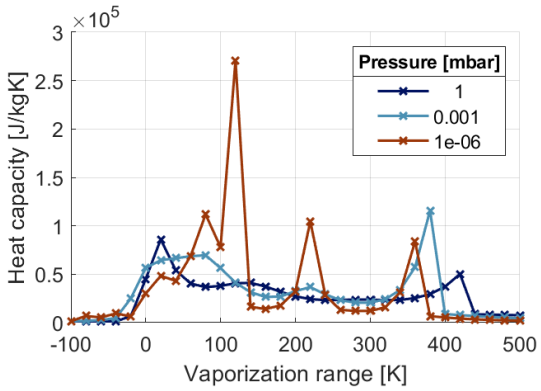

(a) Heat capacity C_p

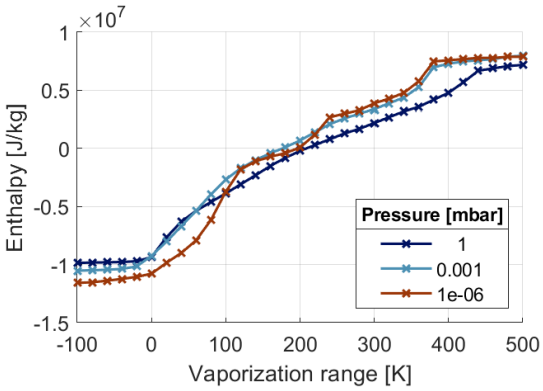

(b) Enthalpy h

Figure 5.6 Heat capacities and enthalpies from the thermochemical calculation for different pressures plotted over the phase transition range

The apparent heat capacity and enthalpy values from the thermochemical model are divided into a base C_p model, describing regolith heating without phase transitions and reactions, and simplified phase change/reaction enthalpies. Fig. 4.4 and Fig. 4.5 provide a base heat capacity as a function of temperature throughout the simulated temperature range from 298 K to 3773 K. These functions model only the heating of the material. The latent heat of the phase changes and reaction enthalpy can be calculated as described in section 4.3.2 by subtracting the heating enthalpy from the total enthalpy change. Adjusted values are used for the thermal surface model because of the use of fitted heat capacity base functions (Eq. 4.1). These slightly underestimate the heating capacity in the phase transitions, especially in the vaporization regime. Therefore, the latent heat of melting L_m and vaporization/sublimation L_v are slightly higher for thermal modeling. Values for true latent heat values are shown in the supplementary table B.1 and the adjusted values for use in COMSOL are shown in Tab. 5.1.

Table 5.1 Phase transition data input for the COMSOL Multiphysics simulation of the regolith surface for the Maria composition for each pressure decade: solidus temperature $T_{solidus}$, melting temperature range ΔT_m, latent heat of melting L_m, bubble temperature T_{bubble}, vaporization/sublimation temperature range ΔT_v, and latent heat of vaporization/sublimation L_v

p [mbar]	$T_{solidus}$ [K]	ΔT_m [K]	L_m [J kg^{-1}]	T_{bubble} [K]	ΔT_v [K]	L_v [J kg^{-1}]
1.00E+03	1363	220	5.51E+05	3283	490	1.34E+07
1.00E+02	1363	220	5.51E+05	2893	470	1.44E+07
1.00E+01	1363	220	5.51E+05	2583	450	1.48E+07
1.00E+00	1363	220	5.51E+05	2333	430	1.51E+07
1.00E-01	1363	220	5.51E+05	2123	420	1.56E+07
1.00E-02	1363	220	5.51E+05	1953	400	1.56E+07
1.00E-03	1363	220	5.51E+05	1803	390	1.63E+07
1.00E-04	1363	220	5.51E+05	1673	380	1.63E+07
1.00E-05	1363	190	4.76E+05	1553	380	1.70E+07
1.00E-06	1363	90	2.25E+05	1453	370	1.72E+07
1.00E-07	1363	-	-	1363	360	1.73E+07
1.00E-08	1303	-	-	1303	330	1.62E+07

The values given for the latent heat of vaporization in these tables already include the enthalpies of the pyrolysis reactions. This accounts for all enthalpy changes between two thermodynamic equilibrium points at the beginning and the end of a vapor phase transition, which lasts for 330 K to 490 K (Fig. 5.6b), which includes latent heat, heating of the components not undergoing a phase change, and the reaction enthalpy as explained in section 4.3.2.

Latent heats of melting and vaporization/sublimation are included in the thermal model using the phase change module, which uses the apparent heat capacity method to increase the heat capacity during a phase change between phases θ_1 and θ_2, shown in Fig. 5.7 [71]. This method is simpler for the COMSOL solver than implementing the FactSage data directly when solving the heat transfer differential equation Eq. 5.4 with density ρ, spatial coordinate u, heat conductivity k, and heat flux Q.

$$\rho C_p \frac{dT}{dt} + \rho C_p u \cdot \nabla T - \nabla \cdot k \nabla T = Q \tag{5.4}$$

The apparent heat capacity method is based on the basic relation between heat capacity C_p and enthalpy H, which defines heat capacity as a change of enthalpy over a temperature range [71].

$$C_p = \frac{dH}{dT} \tag{5.5}$$

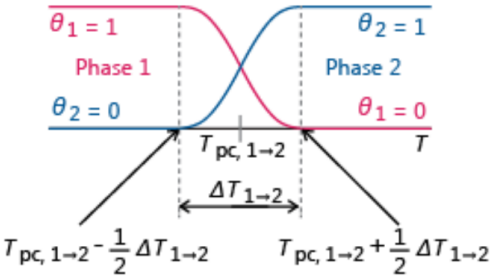

Figure 5.7 Phase indicators θ_1, θ_2, and phase change temperatures during a phase transition interval in the COMSOL Phase change material module [71]

Expanding this heat capacity for two phases with phase indicators θ_1 and θ_2, heat capacities $C_{p,1}$ and $C_{p,2}$, and a latent heat distribution C_L. This latent heat distribution is approximated as the enthalpy difference between the beginning and end of the phase change range $L = H_2 - H_1$ and a temperature derivative of the mass fraction α_m [71].

$$C_p = \frac{1}{\rho}(\theta_1 \rho_1 C_{p,1} + \theta_2 \rho_2 C_{p,2}) + C_L \tag{5.6}$$

$$C_L = L\frac{d\alpha_m}{dT} \tag{5.7}$$

$$\alpha_m = \frac{1}{2}\frac{\theta_2\rho_2 - \theta_1\rho_1}{\theta_1\rho_1 + \theta_2\rho_2} \tag{5.8}$$

Latent heat distribution is defined so that the total latent heat absorbed during a phase change equals the latent heat of a full phase transition.

$$\int_{T_{pc}+\Delta T/2}^{T_{pc}-\Delta T/2} C_L(T)\,dT = \int_{T_{pc}+\Delta T/2}^{T_{pc}-\Delta T/2} \frac{d\alpha_m}{dT}\,dT = L \tag{5.9}$$

Replacing the two heat capacity values with a temperature-dependent heat capacity base function $C_p(T)$ and assuming a constant density valid throughout the temperature range, C_p and α_m can be simplified to Eq. 5.10 and Eq. 5.11. Latent heat $L(p)$ has to be implemented as pressure-dependent due to the different vaporization/sublimation enthalpy changes for different pressures as shown in Fig. 5.6 and Tab. 5.1. They also show a changing vaporization/sublimation temperature range with pressure, considered in the model with ΔT_m and ΔT_v shown in Tab. 5.1.

$$C_p(T,p) = C_p(T) + L(p)\frac{d\alpha_m}{dT} \tag{5.10}$$

$$\alpha_m = \frac{\theta_2 - \theta_1}{2} \tag{5.11}$$

To consider the temperature and pressure dependency of the apparent heat capacity, COMSOL simulations are run as a parametric study with sets of parameters for each pressure decade modeled previously in FactSage. The sets of heat capacity parameter values are listed in Tab. 5.1 and include the solidus and bubble temperatures ($T_{solidus}$, T_{bubble}), phase transition ranges ΔT_m and ΔT_v, and the latent heats L_m and L_v for melting and vaporization/sublimation separately. ΔT_m and ΔT_v are also shown visually in Fig. 5.6b, where the overlap of melting and vaporization transitions can be seen at 10^{-7} mbar to 10^{-5} mbar.

Solidus, liquidus, bubble, and dew temperatures with the phase transition ranges are shown in Fig. 5.8. In the pressure range 10^{-4} mbar to 10^{-7} mbar where melting and vaporization/sublimation overlap the melting transition is cut short and the latent heat is reduced (Tab. 5.1) before the vaporization/sublimation transition begins. Below approximately 10^{-5} mbar, where melting and vaporization partially or fully transitions into sublimation, the designation vaporization/sublimation is used for consistency throughout the pressure range when referring to enthalpies or latent heat.

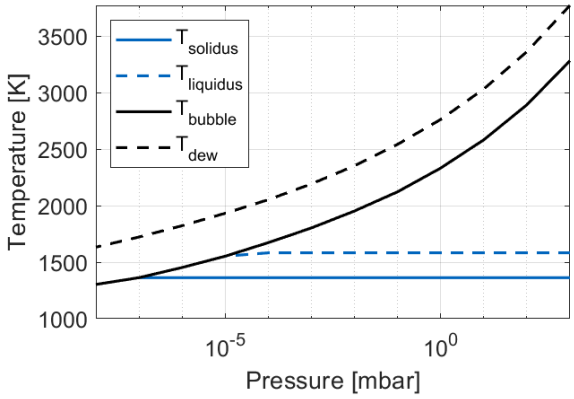

Figure 5.8 Phase transition ranges and characteristic temperatures for melting and vaporization/sublimation phase transitions.

5.2.5 Mesh and solver settings for the surface model

The following section presents studies used for the evaluation of the thermal surface model and the quality of its results. These results can be influenced by the settings of the model and the solver.

Domain and mesh study The mesh is subdivided into two main sections, as shown in Fig. 5.4. The inner domain, directly under the irradiated surface, is subject to high temperature gradients and therefore has to be discretized in smaller elements than the rest of the domain. This inner domain is discretized with structured rectangular elements to achieve better quality results. The rest of the domain serves as a quasi-infinite domain, has low temperature-gradients, and can be discretized in a more simple manner. It is divided into unstructured triangular elements growing from the boundary with the inner domain outwards.

Element and domain sizes have been analyzed through a parameter study with four parameters. The study was conducted using a set of base parameters. A single parameter was changed to the desired value for each study run. Parameter sets where solutions have not sufficiently converged or exhibit linear errors during solving are not considered. The results of these studies are compared based on the resulting temperature gradient using a measurement point grid of size 6σ x 6σ and the output values of the thermal surface model, which are isothermal volume bands of 50 K above 1400 K as is discussed in section 5.3. The NRMSE Errors for all four parameters are shown in Fig. 5.9 for the point grid (a) and the isothermal volume bands (b). Reference values for the error were defined as the finest discretization or largest domain for each parameter.

Parameter "Spot radius" r_{spot} defines the width and height of the inner domain in the cross-section. It is defined as a multiplier of the standard deviation σ of the Gaussian function describing the concentrated solar beam interface. A parameter range of 1 - 6 σ has been chosen. The most flux will be absorbed into the surface inside the 3σ width, but a larger domain has to be studied to account for thermal behavior at

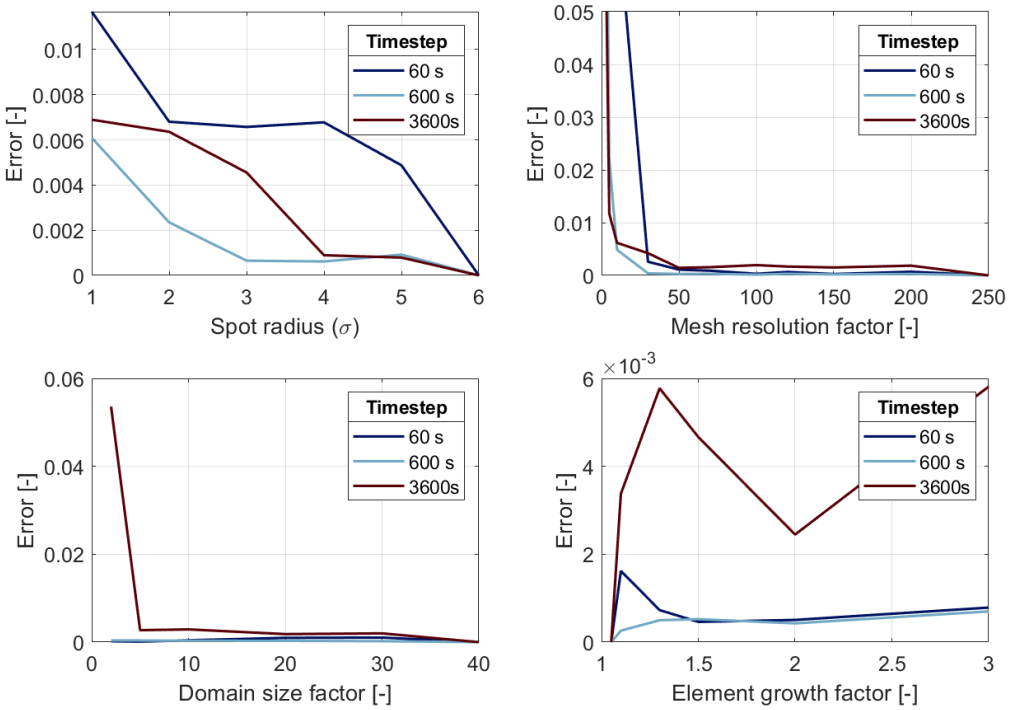

(a) Effect on the temperature

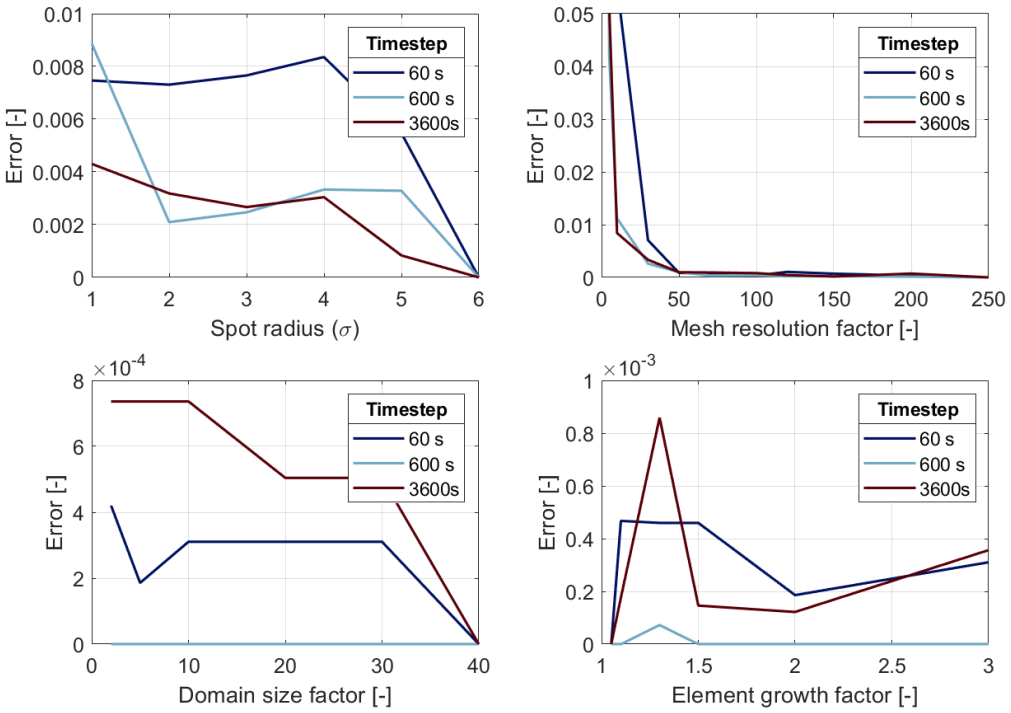

(b) Effect on resulting volume

Figure 5.9 Mesh study of the thermal surface model

later steps when the thermal front has moved beyond the 3σ radius. A radius of 6σ has been chosen as the base value.

Parameter "Mesh resolution factor" f_{mesh} defines the element size in the inner domain where the element size x is defined as $x = r_{spot}/f_{mesh}$. Mesh resolution factors between 1 and 250 have been analyzed, while a base value of 50 was chosen.

Parameter "Domain size factor" f_{domain} defines the marked domain size in Fig. 5.4a with *Domain size* = $r_{spot} \times f_{domain}$. Domain size factors between 2 and 40 have been analyzed, while the base factor was chosen as 20.

Parameter "Element growth factor" $f_{element}$ defines the maximum allowed growth factor of the mesh in the outer domain. Factors between 1.05 and 3 have been analyzed, while a base factor of 1.1 has been chosen.

Fig. 5.9 shows model errors for time steps 60 s, 600 s and 3600 s, although the main focus lies on the 600 s time step, which will be used for model analysis. It is shown that all errors are small (<5%) across the majority of the parameter ranges and below 1% for any chosen value in both analysis metrics. Chosen parameters are 3σ for Spot radius, 70 for the Mesh resolution factor, 20 for the Domain size factor, and 1.5 for the Element growth factor.

5.2.6 Thermal surface modeling results

The result of the thermal model at each parameter and time step is a temperature gradient in the regolith surface, shown in Fig. 5.10 for the timestep of 600 s. This timestep is chosen as a reference time for all further analysis. 600 s is chosen because, at this timestep, the higher temperature regolith reaches an equilibrium in terms of volume and mass, as shown in the supplementary figure C.2, while the low temperature volume increases only slowly. This time is also assumed to be representative of the experiments as it lies between the shortest of around 30 s and the longest solar exposure times of around 3 h.

The presented simulations have been run for absorbed solar fluxes of 24 W to 90 W. The contours at an exposure time of 600 s and two different pressures show, that the regolith at higher pressures of 1 mbar reaches higher temperatures and more volume is heated to these temperatures (Fig. 5.10a, 5.10c, and 5.10e). Regolith at lower pressures of 10^{-8} mbar reaches lower temperatures and less volume is heated to these temperatures (Fig. 5.10b, 5.10d, and 5.10f). This can be attributed to the solar energy flux, which is already used for the vaporization/sublimation of the material at lower temperatures contributing to the latent heat of vaporization/sublimation. This energy is, therefore, not used to heat the solid or liquid regolith to a higher temperature. This effect is significantly more pronounced at higher solar fluxes, where more vaporization/sublimation and dissociation of oxides are expected. The temperature gradient at 24 W is much more similar between the two pressures than at 90 W, where the volume difference is significantly higher.

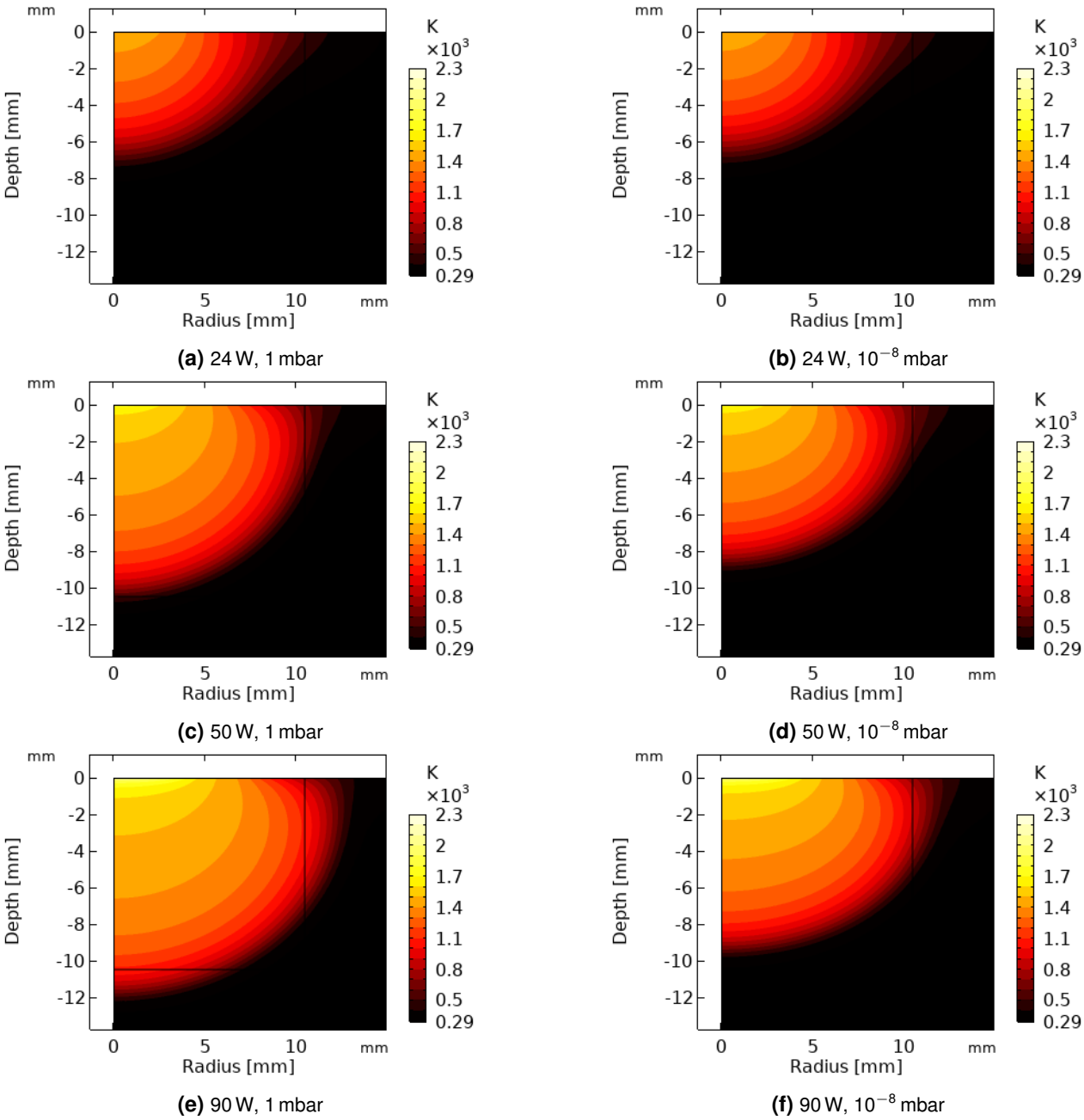

(a) 24 W, 1 mbar

(b) 24 W, 10^{-8} mbar

(c) 50 W, 1 mbar

(d) 50 W, 10^{-8} mbar

(e) 90 W, 1 mbar

(f) 90 W, 10^{-8} mbar

Figure 5.10 Thermal gradient through a vertical cross-section of the regolith surface with applied concentrated solar heating for absorbed solar power of 24 W, 50 W and 90 W at pressures of 10^{-8} mbar and 1 mbar.

5.3 Combined oxygen production model

This analysis aims to connect the temperature state of material to theoretically produced O_2 in the reactor concepts defined in Fig. 5.1. A temperature variable with depth and radius cannot be interpreted by a single equilibrium point from the thermochemical model to produce oxygen yield values (Section 4). The methods for interpreting the temperature gradient produced in the thermal model and calculating produced oxygen mass or pressure are presented in the following.

Temperature gradient solution Oxygen production from the modeled regolith surface is evaluated by evaluating different temperatures along the thermal gradient at constant pressure, based on the assumption that the pressure is constant throughout the reactor and, therefore, also constant throughout the regolith sample.

"Isothermal" volume bands from the temperature gradient are taken for analysis of oxygen production. These bands are defined for each 50 K from 1400 K to 2250 K, shown in Fig. 5.11 from $i = 1$ to $i = n$, with $i = n = 18$ for this model solution.

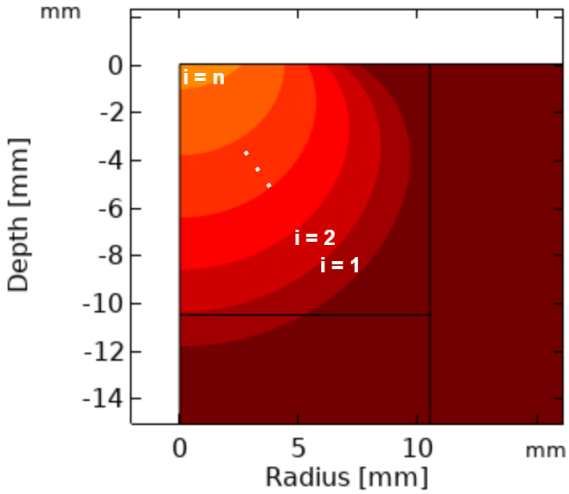

Figure 5.11 Visualization of isothermal volumes from $i = 1$ to n

Eq. 5.12 is used to calculate the total mass of O_2 m_{O_2} as a sum of oxygen masses produced in n isothermal volumes with mass m_i. $\eta_{O_2,i}$ is the O_2 yield of a single isothermal volume between two temperatures T_i and T_{i+1}, where $T_{i+1} = T_i + 50K$. The value of $\eta_{O_2,i}$ is taken from the thermochemical model at the temperature T_i. This is the lower temperature bound of the isothermal band and is, therefore, expected to underestimate oxygen production compared to using the T_{i+1} temperature for each volume.

$$m_{O_2}(p) = \sum_{i=1}^{n} m_i(p)\eta_{O_2,i}(p) \tag{5.12}$$

Similarly, total masses of other species can be calculated by substituting $\eta_{O_2,i}$ with $\eta_{O,i}$ for atomic oxygen or $\eta_{gas,i}$ for total gas.

Melt solution The previous method of calculating total O_2 production from a solar-heated regolith surface is less valid if the material is melted and does not exhibit the temperature gradients in a way shown in Fig. 5.10. To consider a melted material, all material above 1450 K is treated as a homogenous melt with a homogenous temperature T_{melt} in Eq. 5.13. This temperature is calculated as a mass-weighted average of the isothermal bands defined in the previous section.

$$T_{melt} = \frac{\sum_{i=1}^{n} m_i T_i}{\sum_{i=1}^{n} m_i} \tag{5.13}$$

The O_2 production of this melt is evaluated only with the temperature T_{melt} in Eq. 5.14.

$$m_{O_2,melt}(p) = m_{melt}(p)\eta_{O_2,melt}(p) \tag{5.14}$$

5.3.1 Evaluation of oxygen production from the regolith surface

Oxygen production from the regolith surface is evaluated based on three reactors for the thermal gradient and melt solutions, as shown in Fig. 5.1. The underlying values calculated from the temperature state of regolith and equilibrium yields in the previous section are masses of O_2: $m_{O_2}(p)$ and $m_{O_2,melt}(p)$. In reactor version I and I-M, these masses are the direct result, while results for remaining reactor variants have to be calculated through partial pressures. All these considerations are presented in the following.

Reactor variant I and I-M Produced oxygen masses $m_{O_2}(p)$ and $m_{O_2,melt}(p)$ are taken as the direct result for the reactor variant I and I-M (Fig. 5.1), where all produced gaseous material is removed from the chamber. The potential masses of produced molecular oxygen O_2, atomic oxygen O, and total gas after 600 s of solar exposure at 40 W of absorbed power are shown in Fig. 5.12 for different constant pressures. The mass of all products in the gradient solution rises with falling pressure which corresponds with rising yields towards the lower pressures below 10^{-6} mbar, as discussed in section 4.3.3.

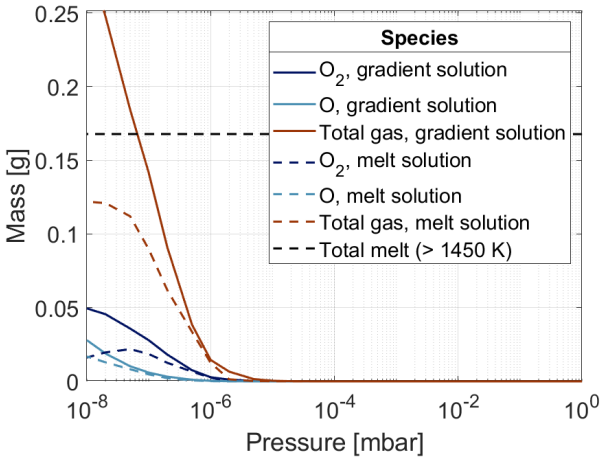

Figure 5.12 Mass of O_2, a combined mass of O_2 and O, and total gas produced from the regolith surface during solar heating at 40 W after 600 s.

The product masses for the melt solution at lower pressures of 10^{-8} mbar to 10^{-7} mbar taper off or even decrease, as shown with O_2. This is likely due to the simplified calculation of the melt volume, which decreases with falling pressures. Less material volume is heated above the assumed melting point at lower pressure since the incoming energy is already partially used for vaporization/sublimation, as discussed in section 5.2.6. This might be the cause of this product decrease in the melt solution. The melt solution is less applicable than the gradient solution at pressures below 10^{-6} mbar since regolith is expected to at least partially sublimate at these pressures as shown in Fig. 4.2.

The assumption of constant pressure means that all gaseous material has to be removed from the chamber immediately as it is produced. This is technically likely not achievable, so this solution presents an ideal case. Significantly higher masses are produced at low pressures below 10^{-6} mbar than above. This would require high mass and volume throughput for the vacuum pumps or other removal solutions of the gaseous material in a high vacuum. This would present a significant engineering problem if such a constant-pressure system shall be designed. Despite the potential engineering challenges, these results are helpful for analysis of pyrolysis behavior in a solar-heated surface and comparing process parameters in section 5.3.2.

Reactor variants II, II-M, III, and III-M: Partial pressure of produced species The second and third set of reactor variants (II, II-M, III, and III-M) are closed systems in terms of mass transfer. It cannot be assumed that all the mass shown previously in Fig. 5.12 in the constant pressure case exists in the gas phase of these reactor variants. Production of oxygen or other gasses from regolith increases the chamber pressure, reducing the gas production from pyrolysis, and some gasses may also oxidize and condense again due to a pressure-induced shift in thermodynamic equilibrium. To estimate this equilibrium pressure of the chamber, theoretical partial pressures are calculated from the theoretically produced gas mass $m_{O_2,melt}(p)$, described in the previous section. Theoretical partial pressures of produced gas species, $p_{O_2}(p)$ in case of O_2, can be approximated by using the ideal gas law and previously calculated produced mass of gas species $m_{O_2}(p)$ or $m_{O_2,melt}(p)$. Eq. 5.15 shows the equation for O_2 partial pressure, although it could be analogously used for other gas species by substituting the mass $m_{O_2}(p)$ or $m_{O_2,melt}(p)$ by a mass of another species. The volume V is arbitrarily set to the chamber volume of $2.3 \times 10^{-3}\,m^3$ from the experimental setup (Section 3) but can be changed easily due to the linear relationships between partial pressure and reactor volume. The temperature T is a mass-weighted average of regolith temperatures, as shown in Eq. 5.13 so that the average energy of all gas in the reactor is conserved. R is the universal gas constant, and M_{O_2} is the molar mass of O_2.

$$p_{O_2}(p) = \frac{m_{O_2}(p)RT}{VM_{O_2}} \tag{5.15}$$

A minor modification is needed to calculate partial pressure of total prodded gas. Its molar mass $M_{gas}(p, T)$ changes throughout the temperature and pressure range of pyrolysis due to the varying composition of the gas. Molar mass is therefore calculated as a mass-weighed average the same way as the T_{melt} in Eq. 5.13, resulting in a $M_{gas}(p)$, which takes into account the gasses produced by the different temperature band along the thermal gradient in the regolith surface.

$$p_{gas}(p) = \frac{m_{gas}(p)RT}{VM_{O_2}(p)} \tag{5.16}$$

A theoretical chamber pressure (Eq. 5.17) is calculated by combining the theoretical partial pressure of a oxygen $p_{t,O_2}(p)$ or total produced gas $p_{gas}(p)$ with an assumed initial chamber pressure p_{ini} of 10^{-8} mbar.

$$p_{t,O_2} = p_{ini} + p_{O_2}(p) \tag{5.17}$$

$p_{t,O_2}(p)$ (and $p_{t,gas}(p)$ analogously) are dependent on the equilibrium computation pressure at which product yield and molar mass are taken from the thermochemical model. This theoretical chamber pressure would exist in the chamber volume under the assumption that all reaction product mass is in the gas phase. This is not a physical solution as it produces pressures above or below the actual chamber pressure for which the gas production yield is calculated in the equilibrium model (Section 4.3). The theoretical pressure is only physically valid when it is equal to the actual pressure in the reactor p_r. This pressure equilibrium point for the reactor can be found at the intersection of curves p_r and p_t. At this intersection point, the pressure for calculating the oxygen or gas yield values is the same as the actual reactor pressure. This is shown in Fig. 5.13, where the real reactor pressure is drawn in black. Theoretical partial pressures computed from thermochemical equilibria are drawn for O_2, a sum of O_2 and O, and total gas.

The left plots in Fig. 5.13 are an overview of the intersection at an absorbed solar flux of 30 W and the right plots are a detailed view of the intersection. 30 W represents an average value of estimated absorbed flux during the solar experiments in section 3. The equilibrium pressures at the line intersections lay between 8.30×10^{-5} mbar and 1×10^{-4} mbar for the gradient solution and 4.96×10^{-5} mbar and 10×10^{-5} mbar for the melt solution with the O_2-based pressure being the lower pressure bound and the total gas-based

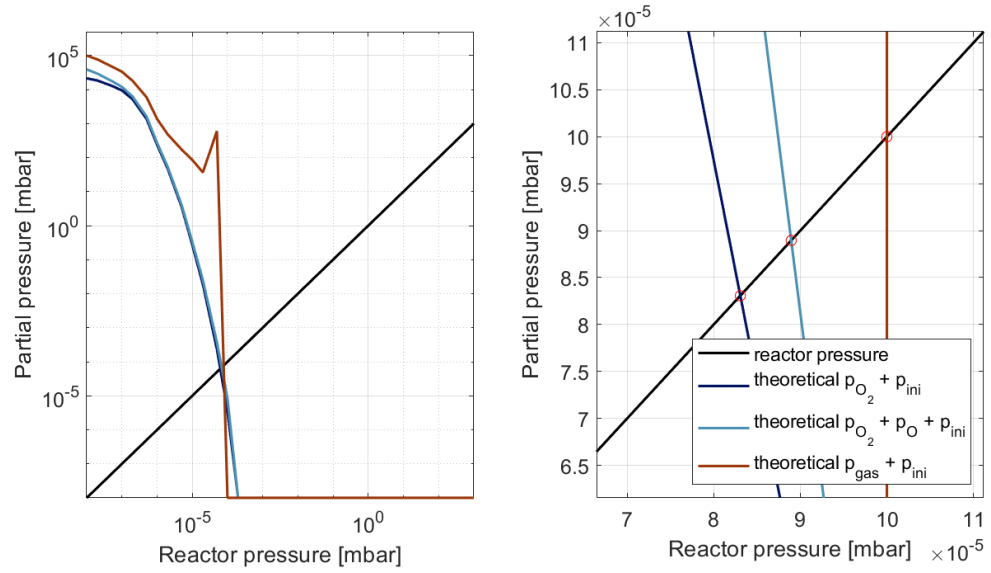

(a) Gradient solution

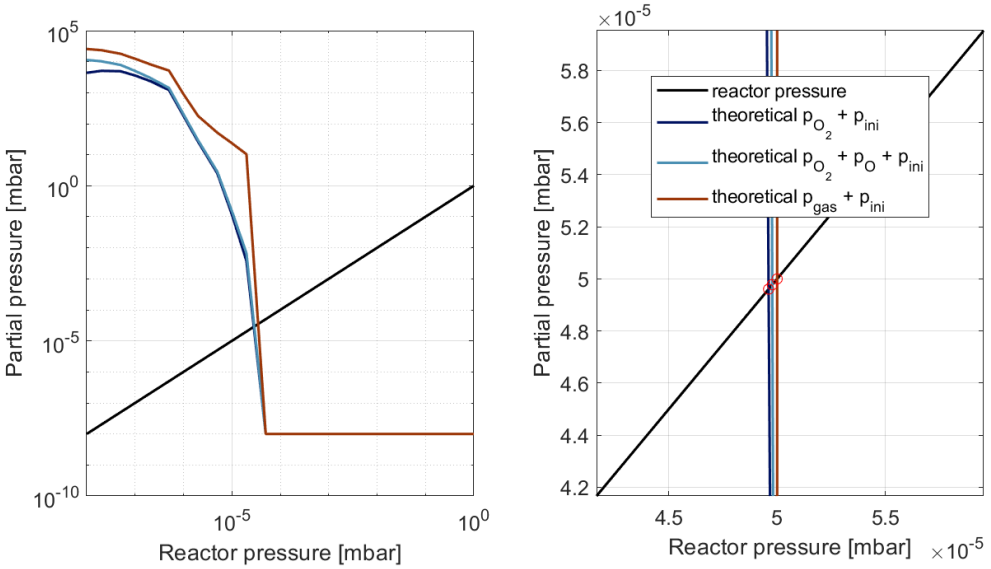

(b) Melt solution

Figure 5.13 Intersection of theoretical reactor pressure and actual reactor pressure for O_2, combined O_2 and O, and total gas at an absorbed power of 30 W. (a) shows the pressures for the gradient solution and (b) the pressures for the melt solution. Initial reactor pressure p_{ini} is chosen at 10^{-8} mbar. The figures on the right are a detailed view of the intersection area with marked intersection points.

pressure the upper bound, as assumed for reactor variants II and III (analogously also for II-M and III-M), respectively (Fig. 5.1). The difference between the pressures for these two reactor variants is less than one-fourth of a pressure decade for the gradient solution and even less for the melt solution, which is not a significant difference when accounting for all the model simplifications. Therefore, reactor variants III and III-M are not considered for further analysis. Only reactor variants II and II-M are considered, which use only the O_2 partial pressures.

These O_2 partial pressure values at pressure equilibrium can be converted back to the mass of O_2 in the chamber using the same ideal gas equations (Eq. 5.15) as were used for the calculation of the theoretical partial pressures before. Mass of O_2 at pressure equilibrium in the closed reactor $m_{O_2,II}$ and $m_{O_2,II-M}$ are

calculated in Eq. 5.18, where $p_{t,O_2}(p_r)$ is the theoretical partial pressure of molecular oxygen at the actual reactor pressure.

$$m_{O_2,II} = \frac{p_{t,O_2}(p_r)\,VM_{O_2}}{RT} \tag{5.18}$$

The calculated O_2 mass is 0.05×10^{-6} g and 0.03×10^{-6} g for gradient and melt solutions at 30 W, respectively. These are technically negligible amounts due to the nature of a small and closed-system reactor. These gas masses can be increased by increasing the volume V of the reactor at the same pressure, although a technically useful amount will likely not be reached with moderate reactor volumes. Higher absorbed solar flux does increase these values, as is shown in the next section. Nevertheless, the usefulness of these closed reactor models is shown to be limited for this analysis. A real reactor would be constantly pumped to extract the reaction products and keep pressure conditions optimal for the pyrolysis reaction as described in section 2.3.

5.3.2 Study of changing absorbed solar flux and oxygen production

The setup of the thermal model in this study is done with parameters from the solar furnace setup, built for experiments in section 3. The parameters of this setup are likely near the lowest boundary, which still allows pyrolysis to occur. Therefore, studying these and higher solar fluxes is valuable, which might improve oxygen production from a solar-heated regolith surface. Produced oxygen mass and reactor pressures at different absorbed solar fluxes modeled in the regolith surface are presented in the following.

Oxygen mass The produced oxygen mass from a solar-heated regolith surface has been evaluated for absorbed solar fluxes of 24 W to 90 W after a time of 600 s. The vapor products are shown for the estimated average absorbed power in the experimental setup of 30 W and the maximum simulated power of 90 W (Fig. 5.14). A three-fold increase in absorbed power increases the maximum produced a mass of O_2 at 10^{-8} mbar by a factor of 17.5. A two-fold increase in power from 30 W to 60 W would already result in a ten-fold increase in oxygen mass. This shows that the experimental setup and this model lie at the lower temperature boundary for pyrolysis and that there is potential for increasing oxygen extraction by increasing the input power.

The rise of maximum produced gaseous molecular oxygen throughout the simulated solar flux range is shown in Fig. 5.15. The maximum masses lie at 10^{-8} mbar for the gradient solutions, as shown in Fig. 5.14. The power-dependent mass in Fig. 5.15 also shows the nearly negligible produced O_2 at the lower solar flux of 24 W to 40 W, estimated for the experimental setup in section 3 and Tab. 3.2. This again shows that higher solar fluxes and higher solar concentrations should be used to increase O_2 production.

Partial pressures A similar trend as for oxygen masses in Fig. 5.15 is also seen with the pressures calculated from reactor variants II and III, showing a considerable increase in partial pressures with increasing absorbed solar flux. Pressures resulting from the melt solution are significantly lower and do not increase with the rising solar flux. This is likely a result of wrong assumptions during the definition of the melt solution, so the melt results have to be interpreted with caution.

Comparison of modeled and experimental pressures in closed reactor models Comparing the resulting pressures in the above figure to the measured pressures during the experimental solar exposures shows that this pressure calculation is likely not accurate. The solar exposures 1 and 2 in Tab. 3.3 in

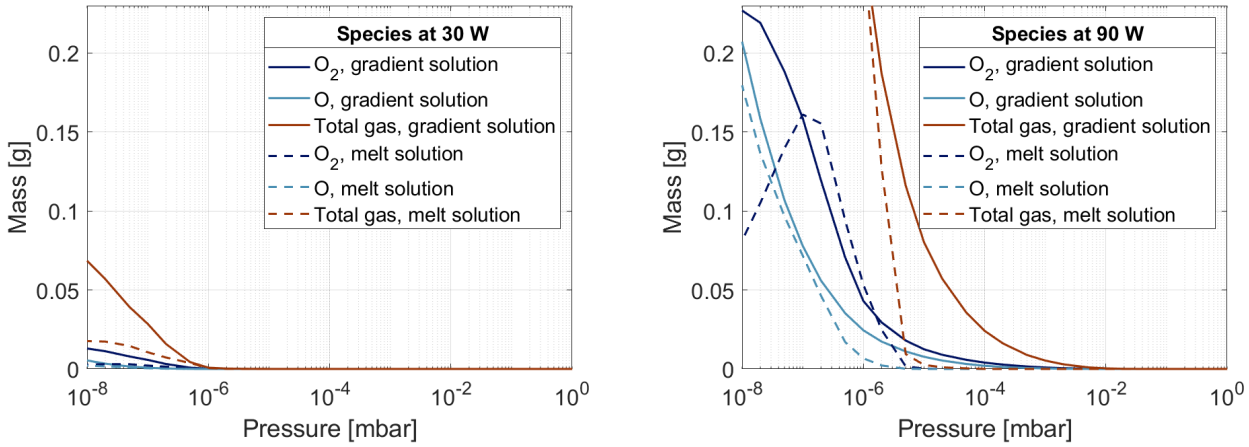

(a) 30 W **(b)** 90 W

Figure 5.14 Mass of O_2, a combined mass of O_2 and O, and total gas produced from the regolith surface during solar heating at 30 W and 90 W after 600 s in an ideally pumped reactor (I and I-M).

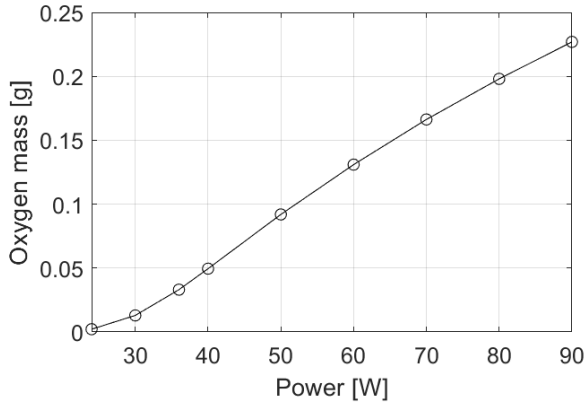

Figure 5.15 Mass of O_2 produced from the regolith surface during solar heating at absorbed solar fluxes of 24 W to 90 W after 600 s of solar exposure.

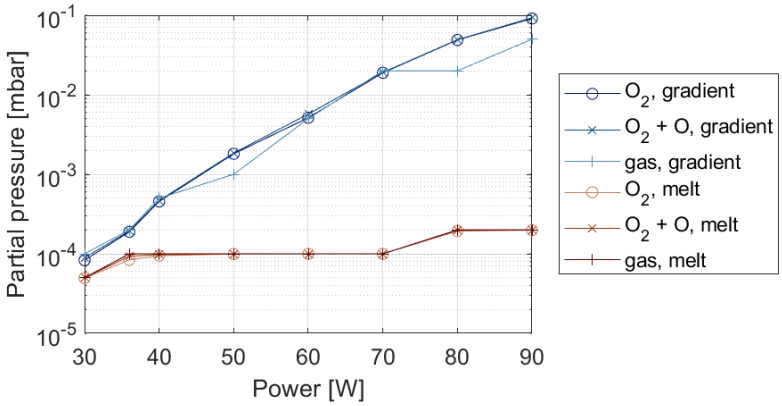

Figure 5.16 Equilibrium pressures for O_2, combined O_2 and O, and total gas at modelled absorbed solar fluxes from 30 W to 90 W.

section 3.3 were performed in a closed chamber without a connected vacuum pump, so these are the best experimental values for comparison with the closed-system reactor models. The pressures achieved during the experiment are on the order of 10^{-1} mbar at an estimated absorbed solar flux of 29 W to 44 W. O_2 and gas pressures produced by the modeled reactors II and III lie approximately two orders of magnitude lower. Melt solutions for the same reactors lie lower for another half of an order of magnitude. This does not correlate with the measured pressures for a closed system. This can likely be attributed to the significant outgassing of volatiles from the regolith sample during the experiment, which is discussed in section 3.3.1. Nevertheless, the results from reactor variants II and III as well as II-M and III-M still need to be interpreted with caution as correctness is not verified.

5.3.3 Oxygen production under terrestrial and lunar solar conditions

All previously discussed combined model results have used the experimental setup's solar flux values. An operational pyrolysis reactor on the lunar surface with similar size of the solar collection area and concentration properties, as those of the experimental setup, would operate on average with 36% more power when a 1000 W m^{-2} is assumed as DNI on Earth and 1363 W m^{-2} on the Moon (Section 2.4). A comparison between estimated absorbed power with terrestrial and lunar solar irradiance is shown in Fig. 5.17. The plotted upper and lower bound (24 W and 36 W) are the average upper and lower absorbed bound discussed in the experiment analysis in section 3.1.4 and listed in 3.2. Values plotted for the lunar surface in Fig. 5.17b are the same lower and upper absorbed bounds but increased by 36%, which result in 32 W and 49 W. Solar flux values were simulated only in 10 W steps above the 40 W values, so 30 W and 50 W are taken as approximate upper and lower bounds. Additionally, an average value between upper and lower bounds is plotted for both lunar and terrestrial cases.

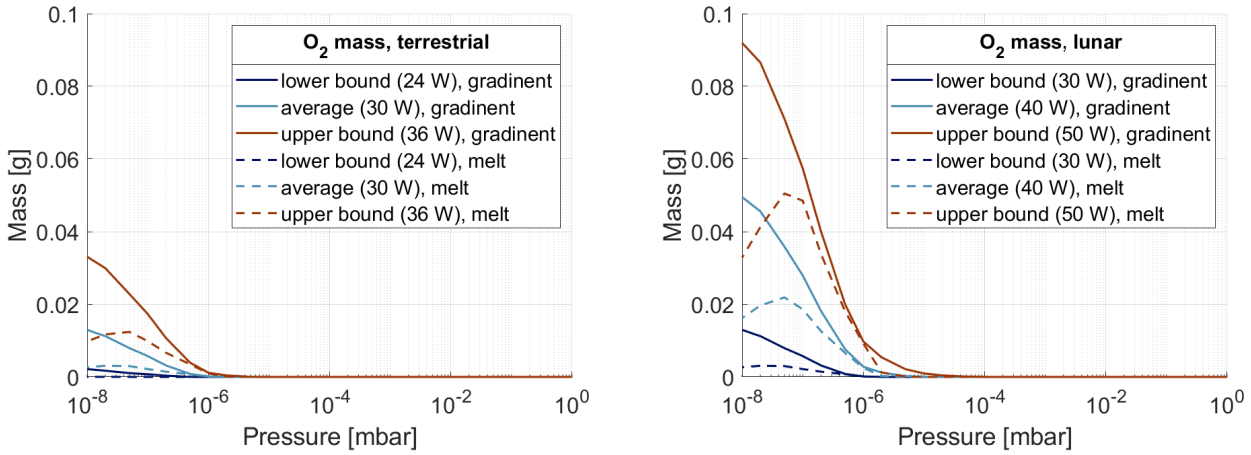

(a) Earth **(b)** Moon

Figure 5.17 Oxygen production in a constant pressure reactor for solar irradiance on the Earth's surface and lunar surface. (a) Earth case: Upper, average, and lower solar flux bounds are taken from the experimental setup; (b) Lunar case: the same upper, average, and lower solar flux bounds are increased by 36% to account for increased solar irradiance on the lunar surface.

Comparing the oxygen production values at the average absorbed-solar flux, a nearly four-fold increase in produced O_2 mass is shown at 10^{-8} mbar with the terrestrial case of 0.013 g and the lunar case of 0.05 g. This is a significant increase in produced O_2 mass for an approximately 36% increase in absorbed power. With increasing the average terrestrial absorbed solar flux, the benefit of a 36% higher irradiance decreases. For example, the upper bound O_2 production increases only 2.5 times during the 36% increase. An increase of power from 60 W to 80 W (approximately 33%) increases the O_2 production even less, only

1.5 times. Thermal simulation has not been run at high enough solar fluxes to evaluate where the increase in produced O_2 would reach an equilibrium or begin to decrease. This diminishing return would have to be studied more closely when designing a pyrolysis reactor to achieve the optimal power to oxygen production ratio.

5.4 Conclusion of the thermal model

This section presented a simple model of a solar-heated regolith surface in a vacuum chamber and tried to evaluate the resulting surface temperatures with yield values from chapter 4 to analyze the potential for oxygen production. The implemented apparent heat capacity and latent heat data from the thermochemical model have produced expected temperature gradients in the regolith. More regolith is heated to higher temperatures at higher pressures and less regolith is heated to lower pressures at lower temperatures due to a part of incoming solar flux being used for the latent heat of vaporization or sublimation.

The thermal model and the derived oxygen production values are more valid for the sublimation regime below 10^{-6} mbar because a solid-state thermal model is used to evaluate temperature in the regolith. The results above 10^{-6} mbar have to be interpreted with caution because the heat transfer and mass transfer phenomena of a melt bubble forming on top of unreacted bulk regolith are not considered in this model.

Out of the six modeled reactor variants defined at the beginning of this chapter in Fig. 5.1, only the open-system reactors I and I-M are used for the analysis. Remaining closed-system reactor and their associated calculation of equilibrium pressures has only limited application and questionable accuracy. More work on refining these pressure calculations would have to be done, for these closed system reactor variants to be useful for analysis of pyrolysis parameters.

The behavior of O_2 production can therefore be compared in the open-system reactor variants at the lowest bound of pressures 10^{-8} mbar to 10^{-6} mbar for different absorbed solar fluxes. The solar fluxes estimated for the experimental setup produce nearly negligible amounts of oxygen, but a small increase in power can produce significantly more. A ten-fold increase in produced O_2 mass is observed when increasing the absorbed flux for 100% from 30 W to 60 W. Similarly, the comparison between oxygen production with a higher solar flux of the lunar surface to the oxygen production on Earth's surface. The higher solar irradiance would result in a four-fold increase of O_2 mass if the absorbed flux of the terrestrial reactor is assumed at 30 W. This significant increase in produced O_2 mass between the terrestrial and lunar case decrease if the base solar flux in the terrestrial case is higher. In general, it can be concluded that a more powerful concentration system than the one built in section 3 would be sensible to improve oxygen generation. Although, solar flux likely should not be increased beyond a particular value because O_2 yields decrease at temperatures beyond the peak O_2 yield, as shown in section 4.3, but an optimal solar flux value has not been defined in this model.

6 Conclusion and outlook

This thesis investigated the process of vapor-phase pyrolysis in a high vacuum regime with concentrated solar power as the heat source. This pressure regime has been identified in literature as attractive due to the potentially lower dissociation temperatures of the regolith. Studies of specific limited pressure ranges have been done, but regolith behavior throughout a wider pressure range has not yet been conducted. This thesis attempts to bridge this knowledge gap through experiments and modeling of regolith pyrolysis.

Pyrolysis experiments have been conducted on a small solar-vacuum furnace using the EAC-1A lunar regolith simulant. Temperatures of 1500 K to 2000 K have been reached during exposures of 30 s to approximately 3 h, while pressures have been measured at 10^{-6} mbar to 10^{-2} mbar in a constantly pumped chamber. Initially planned measurements of gas composition using an RGA were not possible due to large fluctuations in pressure, which reached above the pressure limit of the RGA of 10^{-5} mbar. Melted samples were, therefore, analyzed by EDX for changes in elemental composition. A decrease in oxygen content was measured on the surface of selected melted samples, while a change in other elements could not be clearly seen. Condensation on the crucible was also analyzed and showed significant content of Na and K, which shows the dissociation of at least Na_2O and K_2O. This is additional evidence for partial pyrolysis of the regolith sample. Based on these measurements, it can be concluded that solar-vapor pyrolysis of EAC-1A was demonstrated, fulfilling the first thesis objective.

To better understand the process parameters of vapor pyrolysis, thermochemical equilibrium calculations were performed for low-Ti Mare, high-Ti Mare, Highland regolith, and EAC-1A simulant compositions in a vacuum range of 10^{-8} mbar to 10^{3} mbar. Pyrolysis temperatures of 1400 K to 3700 K have been shown for this pressure range, with pyrolysis temperatures falling with decreasing pressures. Oxygen production was investigated throughout this temperature and pressure range, focusing on molecular oxygen. The temperature range of O_2 production is shown to have an upper limit because molecular oxygen dissociates to atomic oxygen at higher temperatures, which can be detrimental to the process and the reactor hardware. Therefore, process temperatures and pressures must be precisely controlled to optimize oxygen production. Peak yields of 6.6% to 14.1% have been calculated for the different compositions and pressures at thermodynamic equilibrium. These peak yields are pressure-dependent and increase with falling pressure. Realistic yields are expected to be lower than these calculated equilibrium yields and have been estimated at 1% to 8.5% using values from literature. The highest yields are exhibited by the EAC-1A composition, followed by low-Ti Maria, high-Ti Maria, and Highland compositions. This partially fulfills the second thesis objective of determining the ideal reaction temperature and pressure conditions for oxygen production in a small solar-vapor pyrolysis reactor.

A solar-thermal simulation is set up to connect the oxygen yields from the equilibrium calculations to a solar-heated regolith sample and entirely fulfill the second thesis objective. Such samples exhibit high temperature gradients, which cannot be evaluated by a single equilibrium point from the thermochemical calculations. The solar-thermal simulation investigates the thermal behavior of such a surface in a solid-state regime. The thermal gradient is discretized in isothermal bands, which are evaluated for oxygen production using the oxygen yield values from the thermochemical calculations. This simplified model is less valid than initially thought. However, it provides an insight into how the amount of solar flux influences oxygen production and where the lower limits of the process lie, using the assumption of constant reactor pressure, where pyrolysis products are removed from the chamber immediately. This assumption delivers

idealized results since removing high gas mass rates from a high vacuum chamber is technically challenging, especially because high oxygen production is expected below 10^{-6} mbar. The results show that the experimental setup operates at the lower bound of solar concentration, where pyrolysis is still possible. An increase in power would be beneficial, bringing a ten-fold improvement in oxygen generation by only doubling the absorbed solar flux. Although, further increases in the absorbed solar flux would result in increasingly smaller improvements of O_2 generation. This warrants further study to understand ideal solar concentration conditions for oxygen generation.

Further improvements of experimental systems and a better understanding of the pyrolysis process, especially vapor condensation, oxygen processing, and storage, are needed before this process becomes a viable ISRU technology. The following two sections provides a few thoughts on further theoretical and experimental work derived from the lessons learned in this thesis.

6.1 Outlook for the experimental work

The initial plan of using the RGA to measure the gasses produced in the chamber did not work due to high pressures and regolith outgassing. Therefore, a few improvement areas have been identified which must be worked on to improve the pyrolysis behavior and enable the use of the RGA.

Baking Firstly, a better baking solution has to be implemented to release nearly all volatiles in the regolith and reduce its initial outgassing to a minimum. Only then a quantitative analysis of pressure evolution is possible. Additionally, a more powerful heating solution could raise the initial regolith temperature. This would increase the temperatures, which can be reached with only solar heating. It would also allow for better temperature control of the surrounding regolith or the crucible, which could aid in the investigation of condensation behavior.

Setup architecture Secondly, experiments must be run on the setup version 4 described in Fig. 3.5. This would allow for a continuous RGA measurement while constantly pumping the chamber and keeping the chamber at pressures achieved during the exposure of sample 12 of around 10×10^{-4} mbar. A more powerful pump and an improvement of the vacuum conductance of the system through larger piping and closer pump mounting would also be beneficial to lower the pressure peaks during a solar exposure.

Additionally, the optics have to be improved or redesigned for higher solar elevation angles to increase heating efficiency in the summer months and increase the overall power of the furnace. An automatic solar tracking system should also be implemented for the heliostat to keep the hotspot reliably at a single location in the crucible. This was done manually in current experiments, which led to the melt sometimes forming irregular shapes, as shown in Fig. 3.18a.

Condensation Condensation behavior of metal species out of the gas is an essential topic for efficient oxygen production and utilization of metals produced in this process. Controlled condensation of metal and suboxide species in the chamber would enable the analysis of these condensates to understand the pyrolysis process better and improve oxygen production.

Experiments With improved pressure evolution and functioning RGA measurement, several EAC-1A samples, its size fractions, other common simulants (JSC-2A, NU-LHT-2M), and single oxides have to be tested in order to understand the influence of regolith composition on the produced gas.

Material analysis Melt samples must be further analyzed for their elemental composition by EDX measurements of cut and polished samples. This way, consistent, quantitative composition measurements throughout the melt can be made, and conclusions about the composition change relative to depth can be drawn.

6.2 Outlook for the modeling

Modeling based on thermodynamic equilibrium calculations is an ideal approach to modeling pyrolysis behavior. To understand realistic behavior, reaction kinetics have to be studied. While this is an essential topic for future study, adjustments and additions to the existing models can be made.

Equilibrium modelling Equilibrium calculations using lower, average, and upper bounds of single oxide content in the regolith should be performed to understand the influence of a single oxide or mineral on oxygen yield in the context of regolith pyrolysis. The effectiveness of byproduct condensation shall also be studied to determine rates of reoxidation during the cooling of the vapor, its efficiency, and the final O_2 yield after dissociation, condensation, and oxygen capture have been completed.

Thermal modeling Thermal modeling should be improved by considering phase-dependent regolith properties (density, emissivity, and solar absorbance) and a moving mesh boundary to describe the interaction between molten and solid regolith, for example, similar to the melt/regolith boundary modeled by Rumpf et al. [59]. Improved logic shall also be implemented to calculate partial pressures of pyrolysis products so open system (constantly pumped) reactors can be assessed.

A Appendix: Experimental data

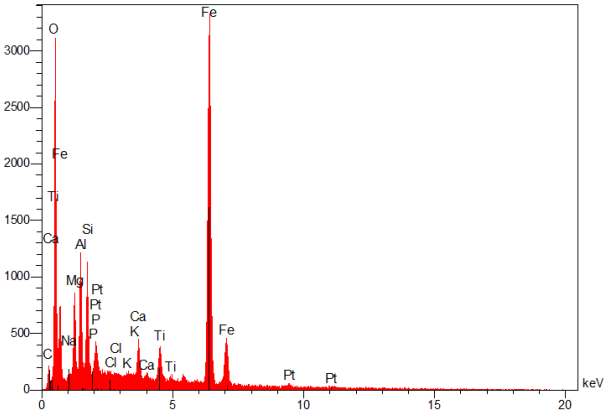

Figure A.1 EDX spectrum of the point 1 on the skin of sample 11

Table A.1 Measurements of ambient solar irradiance E_s, irradiance at the front position after the mirror E_s, back position after the mirror E_2, average irradiance E_2 after the mirror calculated from E_1 and E_2, and the irradiance loss between the environment and the position after the mirror (interpreted as mirror absorbance).

Number	E_s	E_s	E_2	E_2	Irradiance loss
1	960	795	840	817.5	0.1484
2a	900	740	795	767.5	0.1472
2b	930	765	804	784.5	0.1565
3a	965	804	855	829.5	0.1404
3b	940	777	820	798.5	0.1505
4a	954	805	840	822.5	0.1378
4b	958	795	830	812.5	0.1519
5a	995	826	850	838	0.1578
5b	1002	822	862	842	0.1597
6a	920	773	792	782.5	0.1495
6b	925	767	806	786.5	0.1497
7	860	739	767	753	0.1244
8	1008	840	880	860	0.1468
9	1020	840	895	867.5	0.1495
10	1030	840	868	854	0.1709
11	955	787	806	796.5	0.1660

Table A.2 Measurements of the temperature error of the IR camera when shooting through the quartz glass window used in the experimental setup. Measurements have been done on regolith molten by a microwave heating setup in atmosphere. T_1 and T_2 are temperature measurements without a window in front of the camera. T_w is a temperature measurement with the quartz glass window in front of the IR camera performed between T_1 and T_2. T_{ave} is the average of T_1 and T_2. ΔT is the difference between T_{ave} and T_w. Temperature of the target regolith was unstable in measurements 5, 6, and 7, resulting in larger temperature difference.

Number	T_1	T_w	T_2	T_{ave}	ΔT
1	1018.5	1020	1040.3	1029.4	9.4
2	1156.8	1156.3	1174.5	1165.65	9.4
3	1146.3	1125	1132.9	1139.6	14.6
4	1219.5	1222.7	1239.9	1229.7	7.0
5	1373.5	1365	1401.1	1387.3	22.3
6	1437	1429.7	1338.1	1387.55	-42.2
7	1469.2	1410.7	1515.9	1492.55	81.9
8	1449.2	1435.6	1450.1	1449.65	14.1

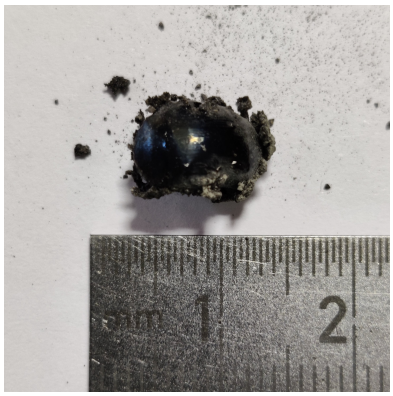

(a) Sample 1

(b) Sample 2

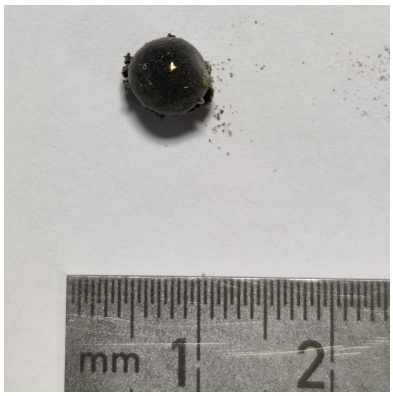

(c) Sample 3, 30s

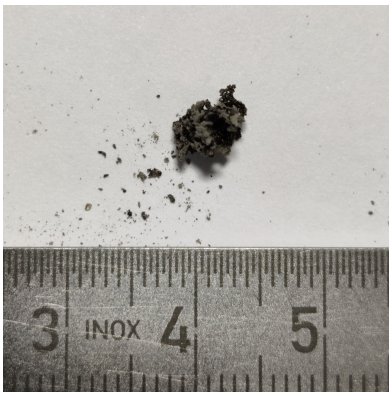

(d) Sample 4, 15s

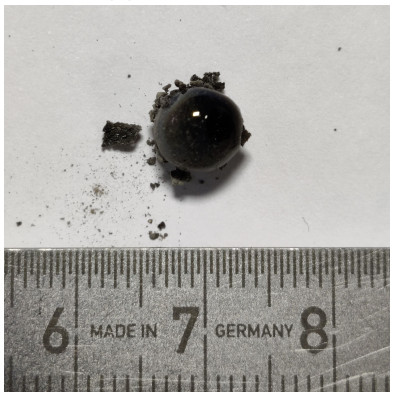

(e) Sample 5

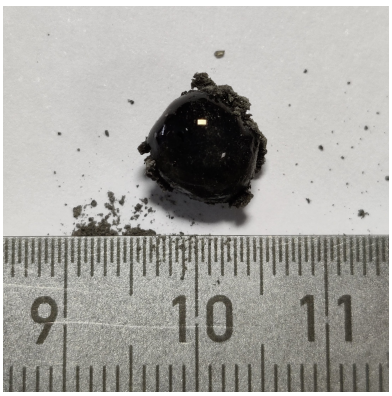

(f) Sample 6

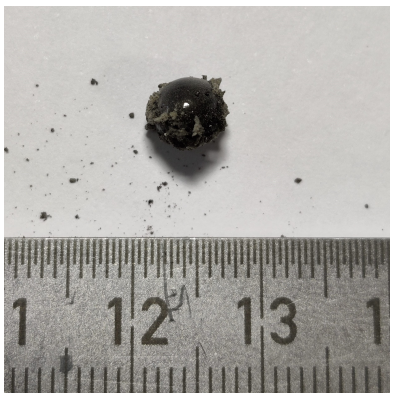

(g) Sample 7

Figure A.2 Additional photos of melted samples 1 to 7

B Appendix: Equilibrium modeling

Table B.1 Phase transition data for the Maria composition for each pressure decade as described in section 4.3.2: solidus temperature $T_{solidus}$, meting temperature range ΔT_m, latent heat of melting L_m, bubble temperature T_{bubble}, vaporization temperature range ΔT_v, and latent heat of vaporization/sublimation L_v.

p [mbar]	$T_{solidus}$ [K]	ΔT_m [K]	L_m [J kg^{-1}]	T_{bubble} [K]	ΔT_v [K]	L_v [J kg^{-1}]
1.00E+03	1363	220	5.47E+05	3283	490	1.19E+07
1.00E+02	1363	220	5.47E+05	2893	470	1.29E+07
1.00E+01	1363	220	5.47E+05	2583	450	1.32E+07
1.00E+00	1363	220	5.47E+05	2333	430	1.34E+07
1.00E-01	1363	220	5.47E+05	2123	420	1.40E+07
1.00E-02	1363	220	5.47E+05	1953	400	1.39E+07
1.00E-03	1363	220	5.47E+05	1803	390	1.46E+07
1.00E-04	1363	220	5.47E+05	1673	380	1.46E+07
1.00E-05	1363	190	4.72E+05	1553	380	1.53E+07
1.00E-06	1363	90	2.24E+05	1453	370	1.55E+07
1.00E-07	-	-	-	1363	360	1.55E+07
1.00E-08	-	-	-	1303	330	1.44E+07

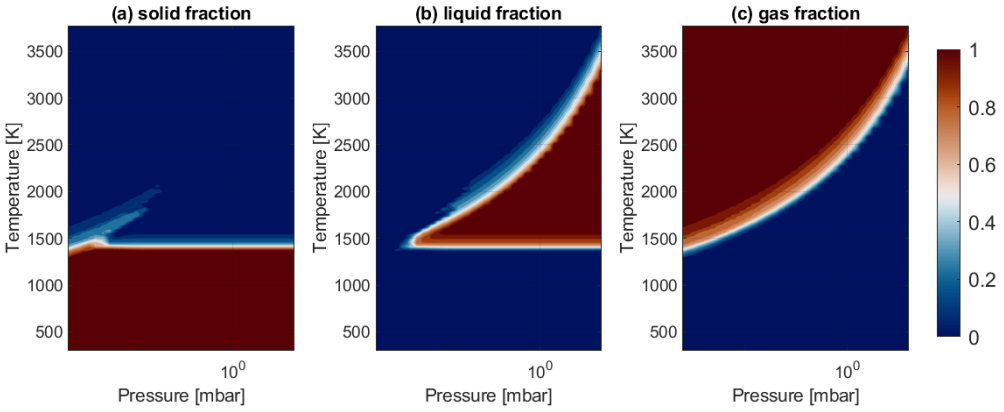

(a) 24999, Low-Titanium Maria

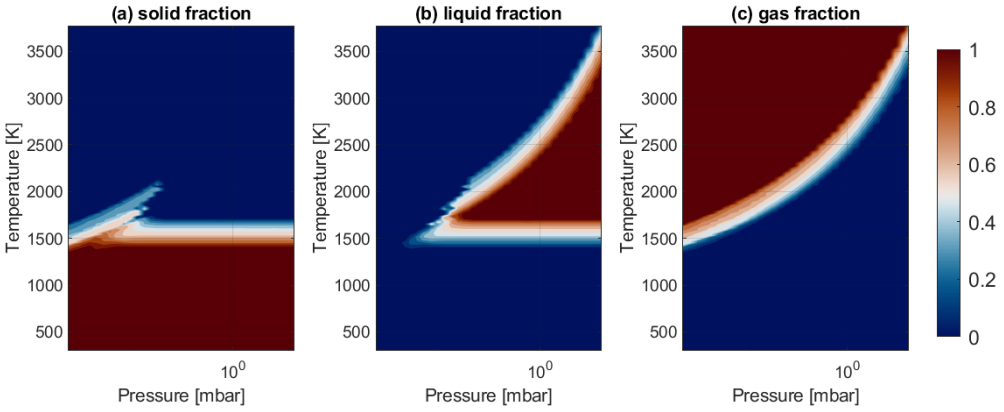

(b) 64501, Highlands

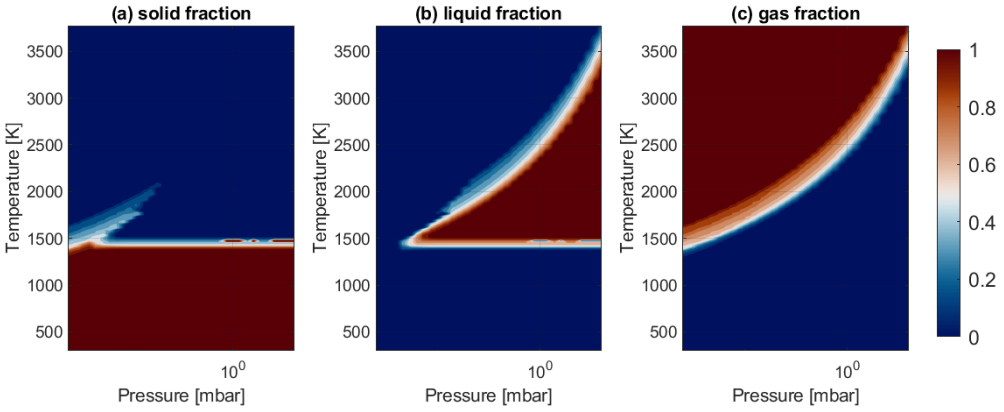

(c) 70051, High-Titanium Maria

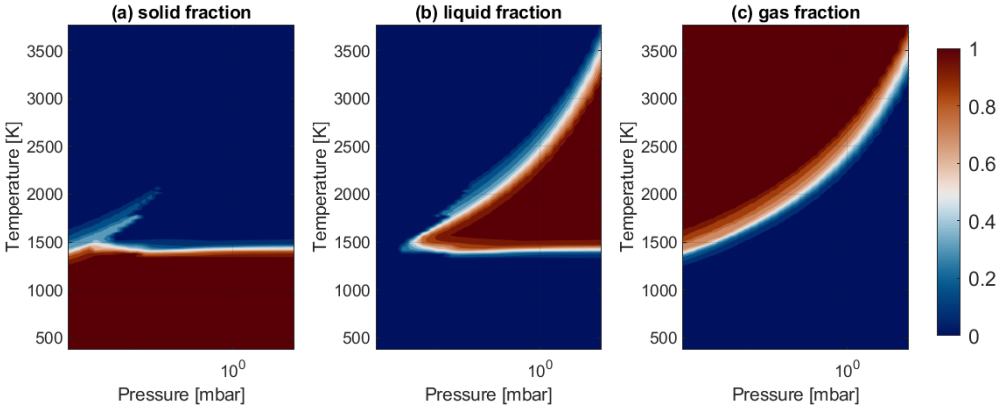

(d) EAC-1A

Figure B.1 Solid, liquid and gas phase mass fractions of 24999, 64501, 70051 and EAC-1A simulant for temperatures of 298 K to 3773 K and pressures of 10^{-8} mbar to 10^{3} mbar.

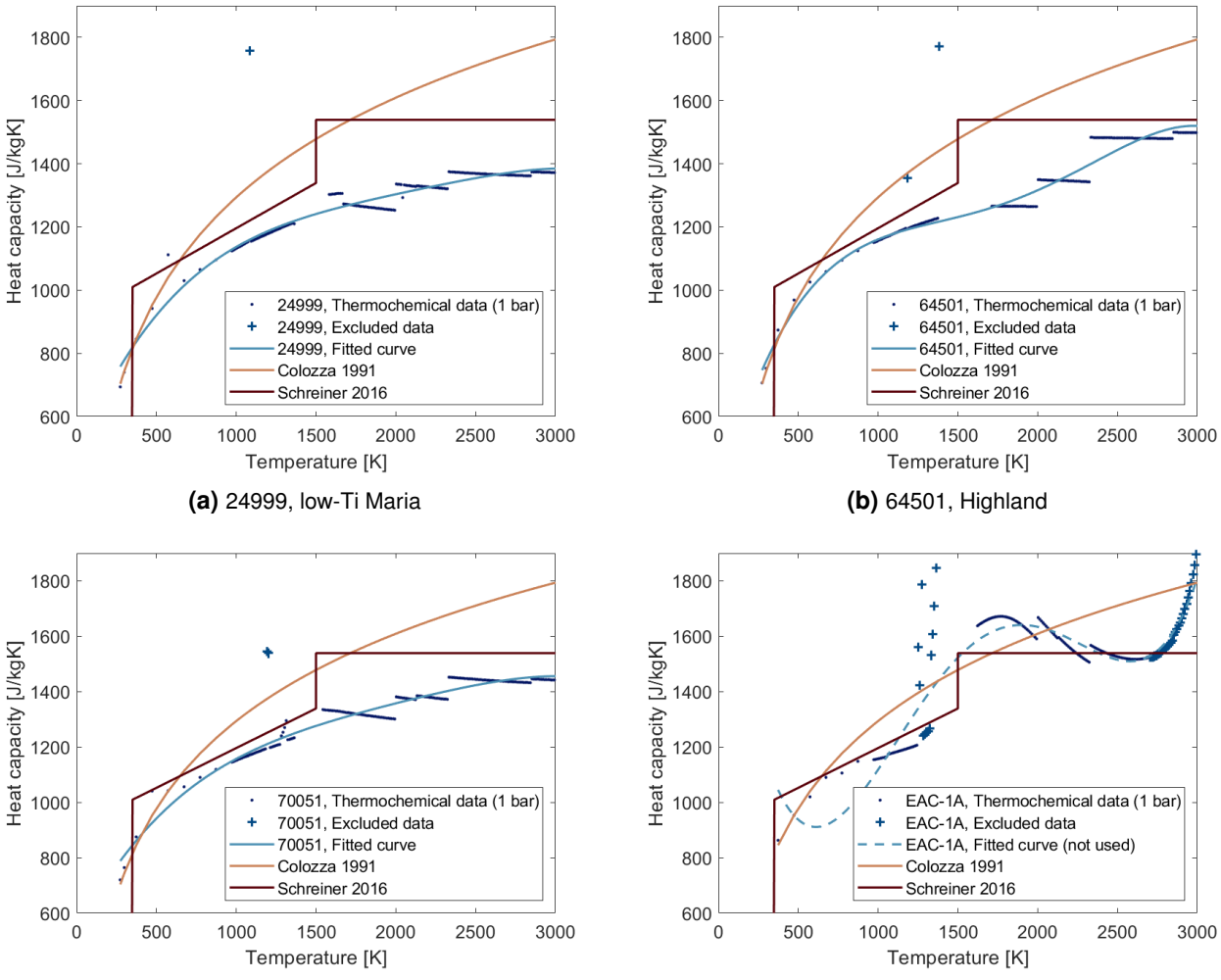

(a) 24999, low-Ti Maria

(b) 64501, Highland

(c) 70051, high-Ti Maria

(d) EAC-1A

Figure B.2 Specific heat capacity data for regolith compositions 24999, 64501, 70051 and EAC-1A simulant from equilibrium modelling in comparison with models from Colozza [48] and Schreiner [28]; Fitted curve for EAC-1A is not used because it does not fit a fourth order polynomial function used for other three compositions Eq. 4.1.

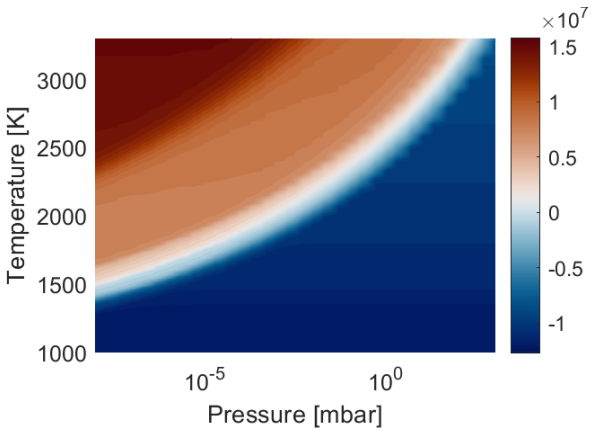

(a) 24999, Low-Titanium Maria

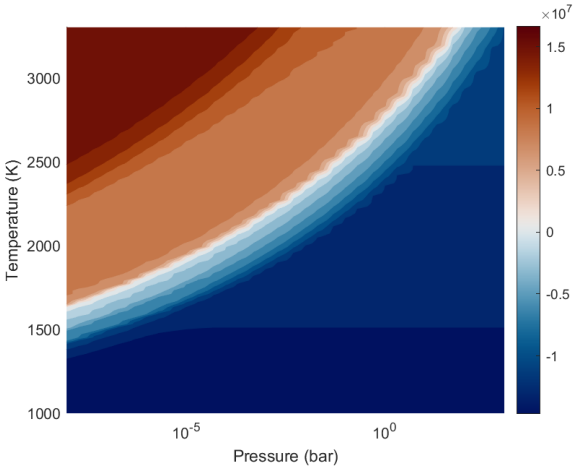

(b) 64501, Highlands

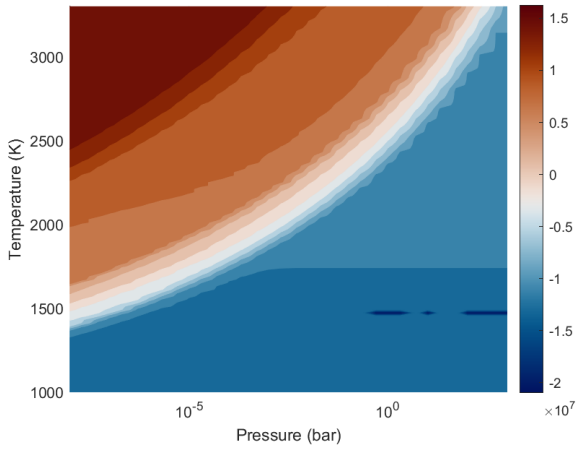

(c) 70051, High-Titanium Maria

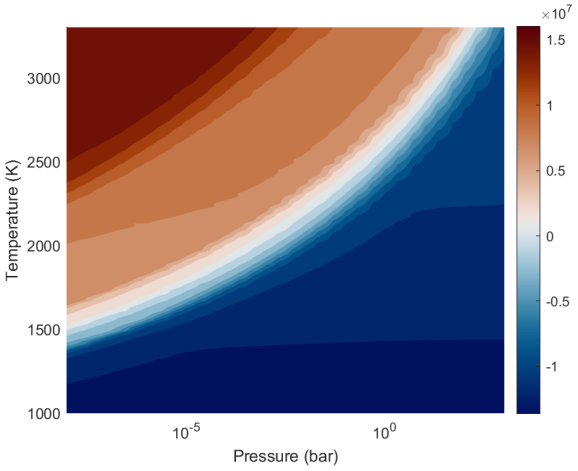

(d) EAC-1A

Figure B.3 Total enthalpies of 24999, 64501, 70051 and EAC-1A simulant for temperatures of 298 K to 3773 K and pressures of 10^{-8} mbar to 10^{3} mbar.

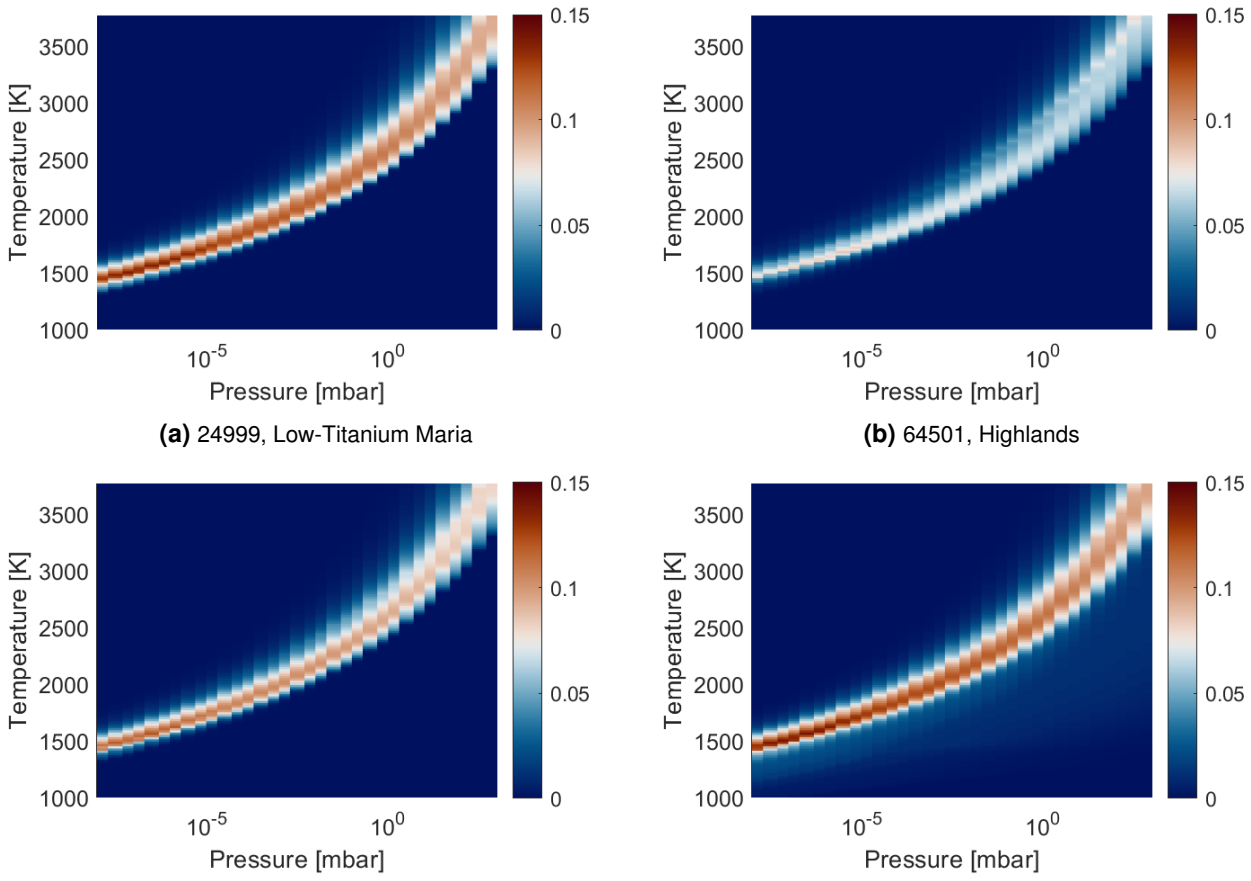

(a) 24999, Low-Titanium Maria

(b) 64501, Highlands

(c) 70051, High-Titanium Maria

(d) EAC-1A

Figure B.4 O_2 yield for regolith compositions 24999, 64501, 70051 and EAC-1A simulant at temperatures of 298 K to 3773 K and pressures of 10^{-8} mbar to 10^{3} mbar.

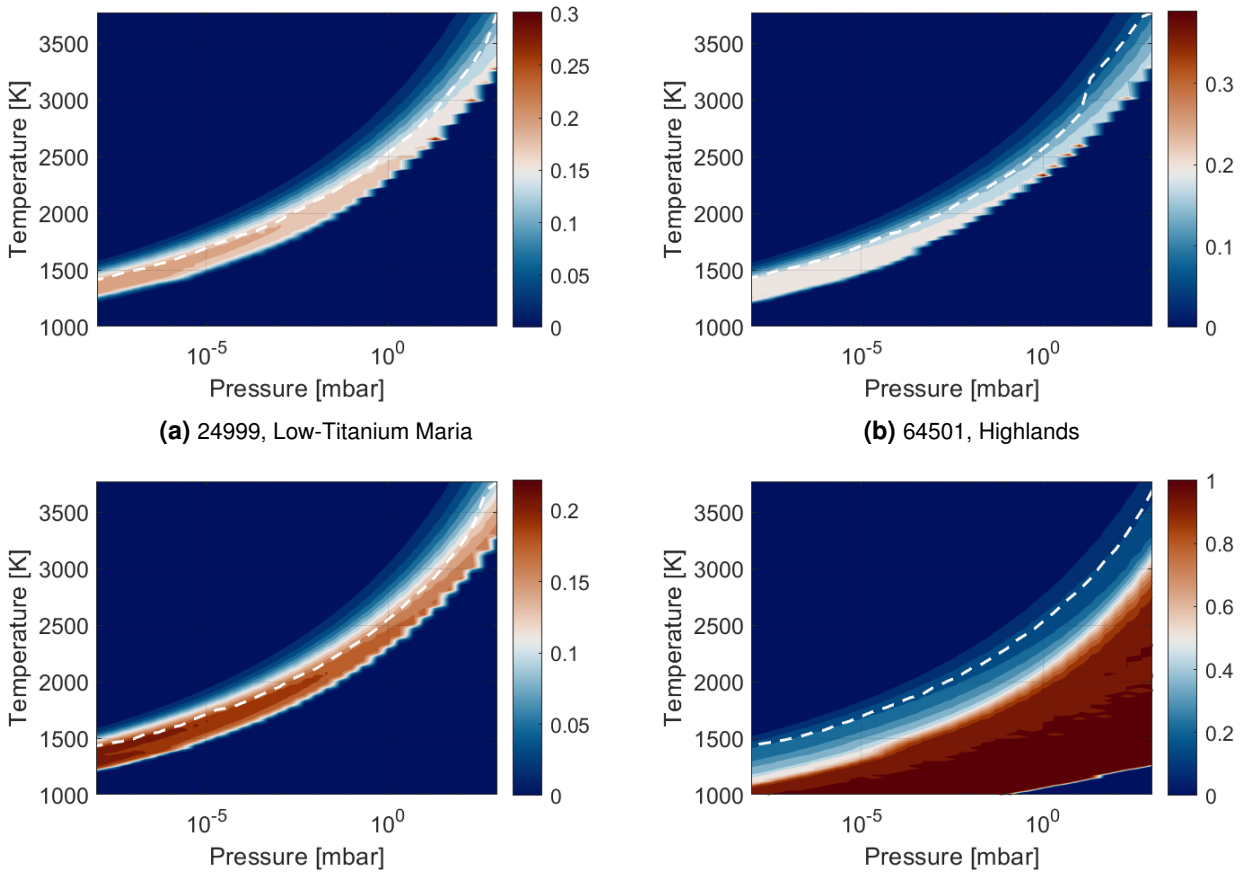

(a) 24999, Low-Titanium Maria

(b) 64501, Highlands

(c) 70051, High-Titanium Maria

(d) EAC-1A

Figure B.5 O_2 mass fraction of gas for regolith compositions 24999, 64501, 70051 and EAC-1A simulant at temperatures of 298 K to 3773 K and pressures of 10^{-8} mbar to 10^{3} mbar. The white dashed line represents the temperature of peak O_2 yield at given pressure.

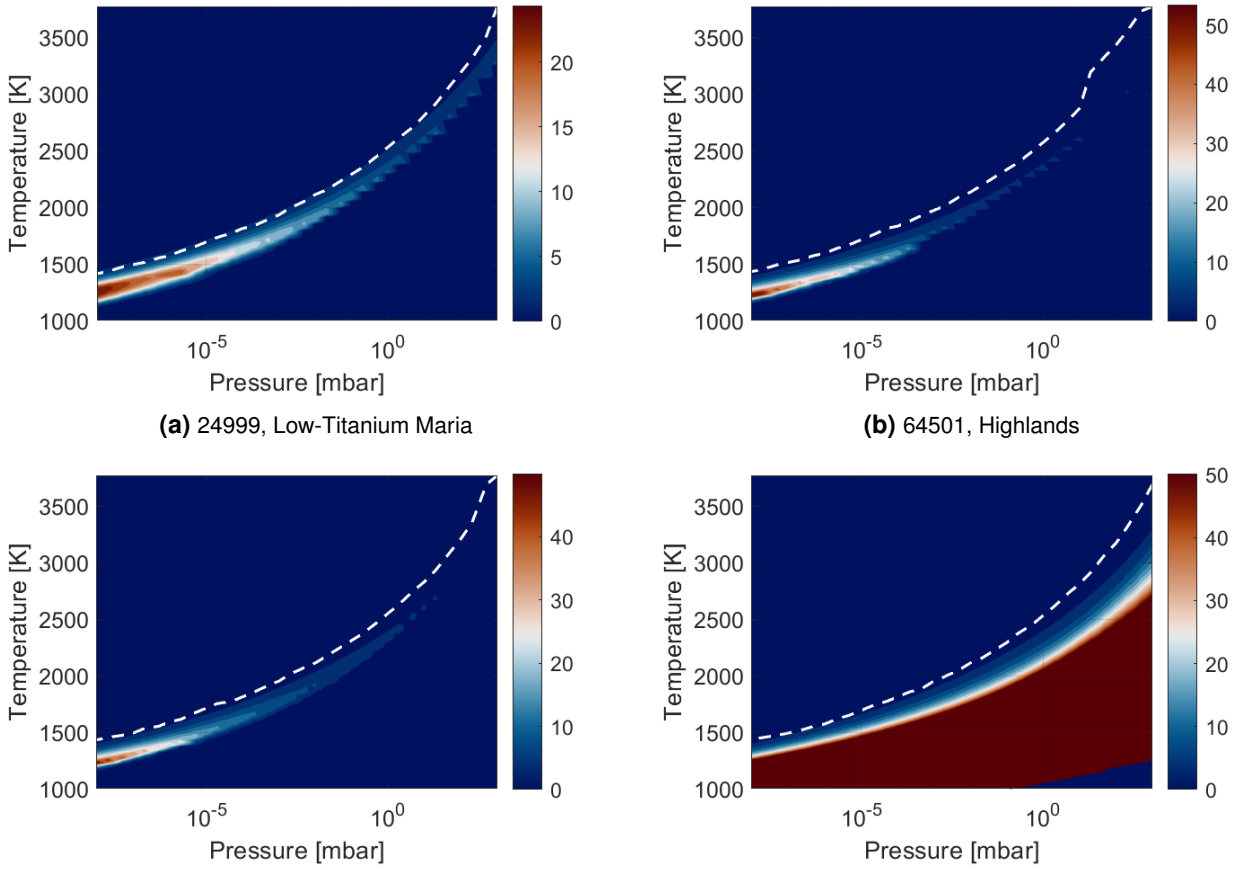

(a) 24999, Low-Titanium Maria

(b) 64501, Highlands

(c) 70051, High-Titanium Maria

(d) EAC-1A

Figure B.6 O_2/O mass ratios for regolith compositions 24999, 64501, 70051 and EAC-1A simulant at temperatures of 298 K to 3773 K and pressures of 10^{-8} mbar to 10^{3} mbar. The white dashed line represents the temperature of peak O_2 yield at given pressure.

C Appendix: Thermal modeling

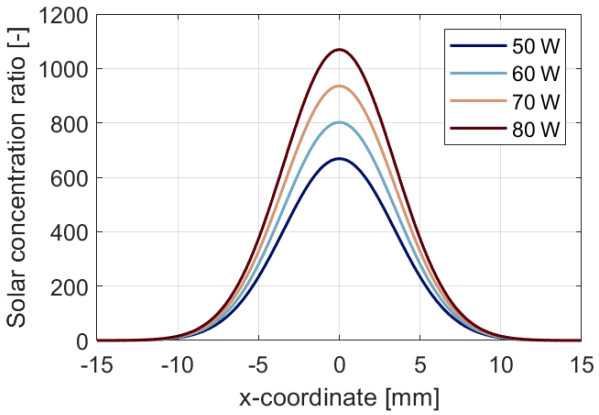

Figure C.1 Solar concentration factor for different incoming solar fluxes Φ_{reg} at the regolith surface using the optical parameters of the experimental setup. The shown curves are representative of the experimental setup where the estimated incoming solar flux at the regolith surface is in the range of 47.7 W to 49.4 W.

Table C.1 Solver settings for the thermal surface model in COMSOL Multiphysics

Parameter	Value
type	transient
time stepping method	BDF
max. BDF order	5
min. BDF order	2
initial time step	0.001s
solver	Direct, PARADISO
solver method	Newton, highly non-linear
max. number of iterations	50

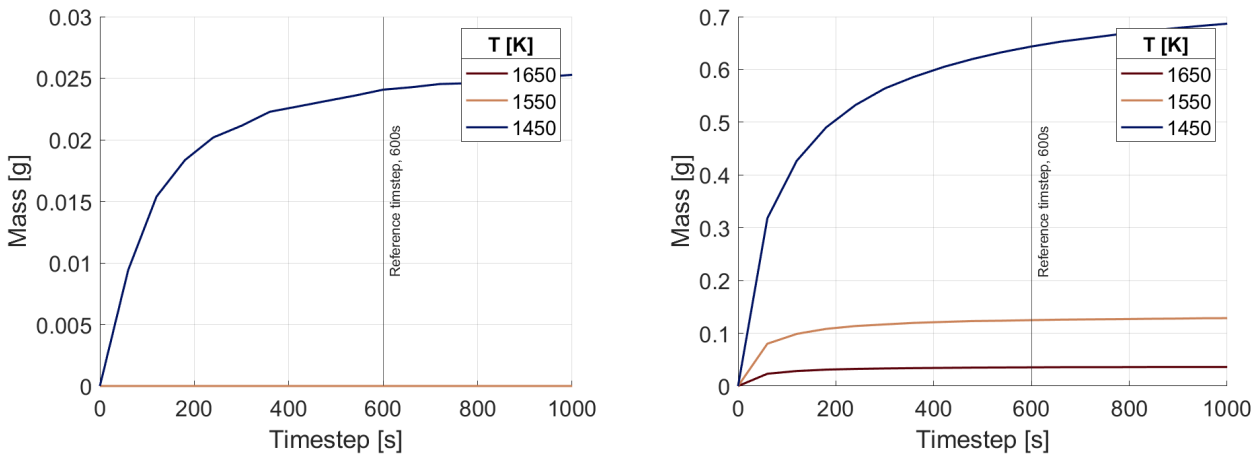

(a) 30 W

(b) 90 W

Figure C.2 Mass of "isothermal" 50 K bands over time in the thermal simulation for absorbed solar fluxes of 30 W and 90 W with marked reference time step of 600 s. The higher temperatures reach a volume/mass equilibrium before the chosen reference timestep of 600 s. Only the lowest isothermal bands below 1450 K are sill increasing in volume/mass.

Bibliography

[1] A. Cassel, "Forward to the moon: Nasa's strategic plan for human exploration." https://www.nasa.gov/sites/default/files/atoms/files/america_to_the_moon_2024_artemis_20190523.pdf. [Acessed on 04/09/2022].

[2] ISECG, "The global exploration roadmap january 2018." www.globalspaceexploration.org, 2018. [Acessed on 10/04/2022].

[3] B. R. Blair, J. Diaz, M. Duke, E. Lamassoure, R. Easter, M. Oderman, and M. Vaucher, "Space resource economic analysis toolkit: The case for commercial lunar ice mining," techreport, Colorado School of Mines, 2002.

[4] H. Jones, "The Recent Large Reduction in Space Launch Cost," in *48th International Conference on Environmental Systems*, 48th International Conference on Environmental Systems, 2018. ICES-2018-81.

[5] B. A. Lomax, "Characterisation and evaluation of lunar regolith simulants for use in in-situ resource utilisation research," Master's thesis, Heriot-Watt University, 2019.

[6] D. Kornuta, A. Abbud-Madrid, J. Atkinson, J. Barr, G. Barnhard, D. Bienhoff, B. Blair, V. Clark, J. Cyrus, B. DeWitt, C. Dreyer, B. Finger, J. Goff, K. Ho, L. Kelsey, J. Keravala, B. Kutter, P. Metzger, L. Montgomery, P. Morrison, C. Neal, E. Otto, G. Roesler, J. Schier, B. Seifert, G. Sowers, P. Spudis, M. Sundahl, K. Zacny, and G. Zhu, "Commercial lunar propellant architecture: A collaborative study of lunar propellant production," *REACH*, vol. 13, p. 100026, 2019.

[7] I. A. Crawford, "Lunar resources: A review," *Progress in Physical Geography: Earth and Environment*, vol. 39, no. 2, pp. 137–167, 2015.

[8] C. A. Jones, J. Klovstad, E. Judd, and D. Komar, "Cost Breakeven Analysis of Cis-lunar ISRU for Propellant," in *AIAA Scitech 2019 Forum*, American Institute of Aeronautics and Astronautics, 2019.

[9] L. Schlüter and A. Cowley, "Review of techniques for in-situ oxygen extraction on the moon," *Planetary and Space Science*, vol. 181, p. 104753, 2 2020.

[10] C. Schwandt, J. A. Hamilton, D. J. Fray, and I. A. Crawford, "Oxygen from lunar regolith," in *Moon: Prospective Energy and Material Resources* (V. Badescu, ed.), vol. 9783642279690, pp. 165–187, Springer-Verlag Berlin Heidelberg, 1 ed., 7 2012.

[11] C. Senior, "Lunar oxygen production by pyrolysis," *AIAA Space Programs and Technologies Conference, 1992*, 1992.

[12] Y. Zhang, G. Brooks, A. Rhamdhani, and C. Guo, "Review on solar thermochemical processing for lunar applications and their heat transfer modeling methods," *Journal of Heat Transfer*, vol. 143, 12 2021.

[13] A. R. Clendenen, "Concentrated solar driven in-situ resource utilization for lunar exploration," Master's thesis, Georgia Institute of Technology, 7 2020.

[14] J. Matchett, "Production of lunar oxygen through vacuum pyrolysis," techreport, The George Washington University, 2006. ADA443950.

[15] M. G. Shaw, G. A. Brooks, M. A. Rhamdhani, A. R. Duffy, and M. I. Pownceby, "Thermodynamic modelling of ultra-high vacuum thermal decomposition for lunar resource processing," *Planetary and Space Science*, vol. 204, p. 105272, 2021.

[16] ESA, "ESA - Spaceship EAC." https://www.esa.int/About_Us/EAC/Spaceship_EAC. [Acessed on 10/04/2022].

[17] G. H. Heiken, D. T. Vaniman, and B. M. French, eds., *Lunar Sourcebook, A User's Guide to the Moon*. Cambridge University Press, 1991.

[18] D. G. Schrunk, B. L. Sharpe, B. L. Cooper, and M. Thangavelu, *The Moon*. Praxis, 2007.

[19] C. R. Neal and L. A. Taylor, "Petrogenesis of mare basalts: A record of lunar volcanism," *Geochimica et Cosmochimica Acta*, vol. 56, no. 6, pp. 2177–2211, 1992.

[20] J. J. Papike, S. B. Simon, and J. C. Laul, "The lunar regolith - Chemistry, mineralogy, and petrology," *Reviews of Geophysics and Space Physics*, vol. 20, pp. 761–826, 1982. ADS Bibcode: 1982RvGSP..20..761P.

[21] J. C. Laul and J. J. Papike, "The lunar regolith: comparative chemistry of the Apollo sites.," in *Lunar and Planetary Science Conference Proceedings*, vol. 2, pp. 1307–1340, 1980. ADS Bibcode: 1980LPSC...11.1307L.

[22] J. C. Laul, J. J. Papike, and S. B. Simon, "The lunar regolith: comparative studies of the Apollo and Luna sites. Chemistry of soils from Apollo 17, Luna 16, 20, and 24.," in *Lunar and Planetary Science Conference Proceedings*, vol. 12, pp. 389–407, 1982. ADS Bibcode: 1982LPSC...12..389L.

[23] L. A. Taylor, C. M. Pieters, and D. Britt, "Evaluations of lunar regolith simulants," *Planetary and Space Science*, vol. 126, pp. 1–7, 7 2016.

[24] V. S. Engelschiøn, S. R. Eriksson, A. Cowley, M. Fateri, A. Meurisse, U. Kueppers, and M. Sperl, "EAC-1A: A novel large-volume lunar regolith simulant," *Scientific Reports*, vol. 10, p. 5473, 12 2020.

[25] M. Alvarez, "Study and characterization of a new lunar regolith simulant: EAC-1A," [internal report], ESA, 2017.

[26] B. S. Hemingway, R. A. Robie, and W. H. Wilson, "Specific heats of lunar soils, basalt, and breccias from the Apollo 14, 15, and 16 landing sites, between 90 and 350 °K," in *Lunar and Planetary Science Conference Proceedings*, vol. 4, p. 2481, 1973. ADS Bibcode: 1973LPSC....4.2481H.

[27] J. F. Stebbins, I. S. E. Carmichael, and L. K. Moret, "Heat capacities and entropies of silicate liquids and glasses," *Contributions to Mineralogy and Petrology*, vol. 86, no. 2, pp. 131–148, 1984-05.

[28] S. S. Schreiner, J. A. Dominguez, L. Sibille, and J. A. Hoffman, "Thermophysical property models for lunar regolith," *Advances in Space Research*, vol. 57, pp. 1209–1222, 3 2016.

[29] K. Watson, *I. The thermal conductivity measurements of selected silicate powders in vacuum from 150 °-350 ° K. II. An interpretation of the Moon's eclipse and lunation cooling as observed through the Earth's atmosphere from 8-14 microns*. PhD thesis, California Institute of Technology, 1964.

[30] S. Parzinger, *Analytische Modellierung der temperatur- und gasdruckabhängigen effektiven Wärmeleitfähigkeitvon Pulvern*. PhD thesis, Technische Universität München, 2014.

[31] P. M. Reiss, *In-Situ Thermal Extraction of Volatiles from Lunar Regolith*. PhD thesis, Technische Universität München, 2018.

[32] P. Reiss, "A combined model of heat and mass transfer for the in situ extraction of volatile water from lunar regolith," *Icarus*, vol. 306, pp. 1–15, 5 2018.

[33] S. Li, P. G. Lucey, R. E. Milliken, P. O. Hayne, E. Fisher, J.-P. Williams, D. M. Hurley, and R. C. Elphic, "Direct evidence of surface exposed water ice in the lunar polar regions," in *Proceedings of the National Academy of Sciences*, vol. 115 (36), pp. 8907–8912, National Academy of Sciences, 2018.

[34] K. Hadler, D. J. P. Martin, J. Carpenter, J. J. Cilliers, A. Morse, S. Starr, J. N. Rasera, K. Seweryn, P. Reiss, and A. Meurisse, "A universal framework for Space Resource Utilisation (SRU)," *Planetary and Space Science*, vol. 182, p. 104811, 2020.

[35] J. Kotze, T. Von Backström, and P. Erens, "Nak as a primary heat transfer fluid in thermal solar power installations," in *Proceeding of SolarPaces 11–14*, 2012. IAC-19-D4.5.15.

[36] H. Benaroya, S. Mottaghi, and Z. Porter, "Magnesium as an ISRU-Derived Resource for Lunar Structures," *Journal of Aerospace Engineering*, vol. 26, no. 1, pp. 152–159, 2013.

[37] W. H. Steurer and B. A. Nerad, "Vapor phase reduction," in *Research on the use of space resources* (W. F. Caroll, ed.), ch. 4, Jet Propulsion Laboratory, NASA, 1983. NASA-CR-173213.

[38] E. H. Cardiff, B. R. Pomeroy, I. S. Banks, and A. Benz, "Vacuum pyrolysis and related isru techniques," *AIP Conference Proceedings*, vol. 880, p. 846, 2 2007.

[39] S. Stern, "The lunar atmosphere: History, status, current problems, and context," *Reviews of Geophysics*, vol. 37, no. 4, pp. 453–491, 1999.

[40] W. J. Kroll, "Vacuum metallurgy—Its characteristics and its scope," *Vacuum*, vol. 2, no. 1, p. 91, 1952.

[41] R. F. Bunshah, "History and current status of vacuum metallurgy," *Journal of Vacuum Science & Technology A*, vol. 12, no. 4, pp. 936–945, 1994.

[42] G. de Maria, G. Balducci, M. Guido, and V. Piacente, "Mass spectrometric investigation of the vaporization process of Apollo 12 lunar samples," in *Lunar and Planetary Science Conference Proceedings*, vol. 2, p. 1367, 1971. ADS Bibcode: 1971LPSC....2.1367D.

[43] G. de Maria and V. Piacente, "Vaporization Study of Selected Lunar Samples," in *Abstracts of the Lunar and Planetary Science Conference*, vol. 4, p. 175, 1973. ADS Bibcode: 1973LPI.....4..175D.

[44] M. Sauerborn, *Pyrolyse von Metalloxiden und Silikaten unter Vakuum mit konzentrierter Solarstrahlung*. PhD thesis, Rheinischen Friedrich-Wilhelms-Universität Bonn, 2005.

[45] J. Matchett, B. Pomeroy, and E. Cardiff, "An oxygen production plant in the lunar environment: A vacuum pyrolysis," in *Space Resources Roundtable VII*, 2005. Abstract.

[46] K. Lamboley, "System architecture for lunar oxygen production from regolith using a model-based system engineering approach," Master's thesis, KTH Royal Institute of Technology, 2021.

[47] F. J. G. Gonzalez, "Analysis of an In-Situ Material Production Concept for Potential Thermal Applications in a Lunar Mission," Master's thesis, Technical University of Munich, 2021.

[48] A. J. Colozza, "Analysis of lunar regolith thermal energy storage," resreport NASA-CR-189073, Sverdrup Technology Inc. for NASA, 1991. NASA-CR-189073.

[49] M. Kaczmarzyk, M. Gawronski, and G. Piatkowski, "Global database of direct solar radiation at the moon´s surface for lunar engineering purposes," *E3S Web Conf.*, vol. 49, p. 00053, 2018.

[50] ASTM, "ASTM e490-00a(2019), standard solar constant and zero air mass solar spectral irradiance tables." `www.astm.org`. [Accessed on 29/05/2022].

[51] ASTM, "ASTM G173-03 reference spectra." `https://www.nrel.gov/grid/solar-resource/spectra-am1.5.html`. [Accessed on 29/05/2022].

[52] D. B. J. Bussey, P. D. Spudis, and M. S. Robinson, "Illumination conditions at the lunar south pole," *Geophysical Research Letters*, vol. 26, pp. 1187–1190, 5 1999.

[53] J. R. Gaier, K. W. Street, and R. J. Gustafson, "Measurement of the Solar Absorptance and Thermal Emittance of Lunar Simulants," in *40th International Conference on Environmental Systems*, 2010. NASA/TM-2010-216788.

[54] Lunar Soil Characterization Consortium, "Bidirectional reflectance spectra for lunar soils." http://www.planetary.brown.edu/relabdocs/LSCCsoil.html. [Acessed on 20/04/2021].

[55] A. Neumann and U. Groer, "Experimenting with concentrated sunlight using the dlr solar furnace," *Solar Energy*, vol. 58, pp. 181–190, 10 1996.

[56] G. Herranz and G. P., "Uses of concentrated solar energy in materials science," *Solar Energy*, 2 2010.

[57] T. Herzig, G. Bihari, and N. Kömle, "PneumoPlanet – Inflatable Moon Habitat (Executive Summary)," resreport, Pneumocell, 2022. [Accessed on 02/09/2022].

[58] P. Reiss, L. Grill, and S. J. Barber, "Thermal extraction of volatiles from the lunar regolith simulant NU-LHT-2M: Preparations for in-situ analyses on the Moon," *Planetary and Space Science*, vol. 175, pp. 41–51, 2019.

[59] M. E. Rumpf, S. A. Fagents, I. A. Crawford, and K. H. Joy, "Numerical modeling of lava-regolith heat transfer on the Moon and implications for the preservation of implanted volatiles," *Journal of Geophysical Research: Planets*, vol. 118, no. 3, pp. 382–397, 2013.

[60] M. Ball and H. Pinkerton, "Factors affecting the accuracy of thermal imaging cameras in volcanology," *Journal of Geophysical Research: Solid Earth*, vol. 111, no. B11, 2006.

[61] Thorlabs, Inc., "A comparisons of thorlabs' thin film aluminum mirror coatings." https://www.thorlabs.com/images/tabimages/Aluminum_Coating_Comparison_Data.xlsx. [Accessed on 03/07/2022].

[62] Edmund Optics Ltd., "18.5" Diameter, 18" Focal Length, Fresnel Lens." https://www.edmundoptics.de/p/185quot-diameter-18quot-focal-length-fresnel-lens/6822/. [Acessed on 04/07/2022].

[63] Kurt J. Lesker Company, "VPZL-600Q." https://www.lesker.com/viewports/viewports-cf-flanged-quartz-fused-silica/part/vpzl-600q. [Acessed on 03/07/2022].

[64] C. Cornwall, A. Horiuchi, and C. Lehman, "NOAA solar position calculator." https://gml.noaa.gov/grad/solcalc/azel.html. [Acessed on 23/03/2022].

[65] E. Cardiff, B. Pomeroy, and J. Matchett, "Production of lunar oxygen by vacuum pyrolysis presentation," in *Space resources roundtable VII: LEAG Conference on Lunar Exploration*, 2005. Presentation.

[66] CRCT, "Factsage database documentation." https://www.crct.polymtl.ca/fact/documentation/. [Acessed on 14/08/2022].

[67] C. W. Bale, E. Bélisle, P. Chartrand, S. A. Decterov, G. Eriksson, K. Hack, I. H. Jung, Y. B. Kang, J. Melançon, A. D. Pelton, C. Robelin, and S. Petersen, "FactSage thermochemical software and databases — recent developments," *Calphad*, vol. 33, no. 2, pp. 295–311, 2009.

[68] C. W. Bale, E. Bélisle, P. Chartrand, S. A. Decterov, G. Eriksson, A. E. Gheribi, K. Hack, I. H. Jung, Y. B. Kang, J. Melançon, A. D. Pelton, S. Petersen, C. Robelin, J. Sangster, P. Spencer, and M.-A. Van Ende, "FactSage thermochemical software and databases, 2010–2016," *Calphad*, vol. 54, pp. 35–53, 2016.

[69] M. Shaw, G. Brooks, M. A. Rhamdhani, A. Duffy, and M. Pownceby, "Applications for Solar Thermal Processing on the Moon and Related Challenges," in *Asia-Pacific Solar Research Conference 2020*, 2020.

[70] E. Hill, M. J. Mellin, B. Deane, Y. Liu, and L. A. Taylor, "Apollo sample 70051 and high- and low-Ti lunar soil simulants MLS-1A and JSC-1A: Implications for future lunar exploration," *Journal of Geophysical Research: Planets*, vol. 112, no. E2, 2007.

[71] COMSOL AB, "Comsol documentation." `https://doc.comsol.com/5.3/docserver/#!/com.comsol.help.comsol/helpdesk/helpdesk.html`. [Acessed on 28/08/2022].

[72] O. I. Yakovlev, V. S. Fainberg, A. I. Shapkin, and G. I. Ramendik, "Melt Evaporation Under Fast Heating Conditions," in *LUNAR AND PLANETARY SCIENCE XVI, PP. 924-925. Abstract.*, pp. 924–925, 1985. ADS Bibcode: 1985LPI....16..924Y.

[73] COMSOL AB, "COMSOL Multiphysics® (Version 5.3)." `www.comsol.com`. [Computer software].

[74] ZEMAX, "ZEMAX OpticStudio® (Version 22.1.2)." `https://www.zemax.com/products/opticstudio`. [Computer software].

[75] H. D. Baehr and K. Stephan, *Wärme- und Stoffübertragung*. Springer, 2010.

[76] F. Crameri, "Scientific colour maps." `https://zenodo.org/record/5501399`, 2018. [Acessed on 03/06/2022].